Spectrum Efficient National Surveillance Radar (SENSR):

OAR Feasibility Study Final Report

Compiled by OAR National Severe Storms Laboratory
24 February 2020

Participants by Organization

J. Boettcher, C. Curtis, I. Ivic, C. Kuster, D. Mirkovic, F. Nai, T. Schuur, D. Schvartzman, S. Torres, D. Wasielewski, B. Wen, M. Weber, N. Yussouf, A. Zahrai

Cooperative Institute for Mesoscale Meteorological Studies, University of Oklahoma and NOAA OAR National Severe Storm Laboratory, Norman, OK

R. Doviak, P. Heinselman, K. Hondl, L. Wicker, D. Zrnic

NOAA OAR National Severe Storms Laboratory, Norman, OK

B. Cheong, C. Fulton, R. Palmer, J. Salazar, H. Sigmarsson, M. Yeary, T. Yu, G. Zhang

Advanced Radar Research Center, University of Oklahoma, Norman, OK

Y. Jung, M. Xue

Center for Analysis and Prediction of Storms, University of Oklahoma, Norman, OK

Xuguang Wang

School of Meteorology, University of Oklahoma, Norman, OK

J. Cho, D. Conway, J. Kurdzo, H. Thomas, E. Clemons

Massachusetts Institute of Technology Lincoln Laboratory, Lexington, MA

Juanzhen Sun, Jeffrey Keeler, Zhuming Ying

National Center for Atmospheric Research, Boulder, CO

T. Wallace

Georgia Tech Research Institute, Atlanta, GA

Abstract

This report summarizes research and development (R&D) activities conducted and coordinated by the National Oceanic and Atmospheric Administration's (NOAA) National Severe Storms Laboratory (NSSL) in support of the Spectrum Pipeline Plan for the Spectrum Efficient National Surveillance Radar (SENSR) Program. The primary focus of NOAA/NSSL's R&D regarded advancing and analyzing Phased Array Radar (PAR) technologies for weather surveillance. This work builds on ongoing PAR R&D conducted by NSSL that is being used to help inform NOAA's National Weather Service's decisions on possible future recapitalization of the current NEXRAD WSR-88D system.

The potential application of new PAR radar technologies to address NOAA's specific mission warranted risk reduction R&D to: assess and validate performance requirements; evaluate whether future PAR technology would be capable of meeting requirements; reduce technical and programmatic risks; and provide a greater degree of confidence that more extensive analysis, development, and demonstrations are appropriate and worthy of greater investment.

Research conducted for the plan focused on: Benefits of Rapid and Adaptive Scanning, Analysis of PAR Data Quality Characteristics, Command and Control Simulator, Network Analysis and Monetized Benefits, Polarimetric Performance and Calibration including Initial Findings using the Advanced Technology Demonstrator (ATD), Cylindrical and All-Digital PAR Architecture Evaluations.

Data assimilation techniques development for the Warn on Forecast System (WoFS) – including determination of optimal observation/assimilation cycle times and refinement of dual-polarization assimilation methods – have progressed significantly, leading towards more realistic assessment of the benefits PAR can bring to this future warning paradigm. Observing System Simulation Experiments (OSSE) indicate that significant potential benefits might result from adaptive radar interrogations of the severe storm environment, for example by enabling observation of clear-air winds in the inflow region of severe storms. Observational studies using NSSL's experimental WSR-88D operating in a rapid-sector scan mode document potential warning improvements for severe storm phenomena through monitoring of polarimetric signatures (e.g. ZDR columns) with fast temporal update. Similarly case studies indicate that flash flood warnings based on radar precipitation observations may be more accurate when the observations are updated at one versus five minute intervals.

PAR data quality characteristics and rapid scanning concepts are analyzed using a high fidelity Signal Processing and Radar Characteristics (SPARC) simulator. SPARC is being used to assess a variety of candidate PAR architectures - for example a rotating planar array, alternative spatial and temporal sampling techniques, and advanced signal processing techniques not readily emulated with NSSL's current PAR testbeds.

Novel econometric studies of the potential operational impacts of enhanced low altitude coverage for tornado and flash flood warnings are presented. These apply geospatial analysis to multi-year, NCEI archives of WSR-88D observations, storm warnings and storm damage reports. The assumptions and methods of analysis indicate that deployment of gap-filling radars, or a more dense overall radar network might improve warning performance, with an associated reduction in casualties.

Research addressing PAR calibration and bias compensation methods was a major component of this effort. These methods are essential for providing dual polarization variable estimates meeting National Weather Service (NWS) requirements. Computational electrodynamic modeling, near- and far-field array probe calibrations and mutual coupling based techniques show considerable promise. A large, dual-polarization phased array radar – the Advanced Technology Demonstrator or ATD – has been deployed at NSSL and initial data analysis provides encouraging evidence that these methods will be effective.

The engineering issues that will drive the choice of array architecture are being addressed using both ATD and smaller PAR prototypes - a cylindrical polarimetric PAR (CPPAR) and an all-digital planar PAR. Experiments using near- and far-field calibration sources and storm target-of-opportunity measurements are exposing the strengths and limitations of these various architectures in realizing NWS observational requirements.

This significant progress towards resolving key questions for meteorological PAR make it appropriate that ongoing OAR PAR research focuses on supporting an NWS acquisition Analysis of Alternatives decision for the WSR-88D replacement network in the coming decade.

Table of Contents

1. Introduction:

In 2016, the Federal Aviation Adminstration (FAA), Department of Commerce (DOC) National Oceanic and Atmospheric Administration (NOAA), Department of Defense (DoD) and Department of Homeland Security (DHS) initiated a feasibility study for a Spectrum Efficient National Surveillance Radar (SENSR). The approach was defined in the The goal was to assess approaches for vacating the 1.3 to 1.35 GHz radio frequency band currently allocated to FAA/DoD/DHS "Long Range Radars (LRR)", so that this band could be auctioned for commercial use. A significant portion of the auction funds would be used to reallocate the LRR surveillance functions to an alternate spectrum band.

A plausible approach for this reallocation would be to consolidate multi-agency national aircraft and weather surveillance functions in the Government controlled 2.7-3.0 GHz "S-band" currently used by NOAA's Weather Surveillance Radar (WSR-88D) and FAA Airport Surveillance Radars (ASR-8, ASR-9 and ASR-11). To evaluate this, and other alternatives, the stakeholder agencies developed requirements for both technical performance and airspace coverage, and evaluated their viability through Government-led technical analysis and requests-for-information (RFI) from the aerospace industry.

NOAA's "High Resolution Weather" requirements for SENSR were based on previously developed National Weather Service (NWS) analysis [NOAA/NWS 2015] and assume as a minimum the capabilities of the legacy operational Weather Service Radar (WSR-88D). Additionally, "objective" requirements were articulated for volumetric scan rates of once per minute - significantly higher than the WSR-88D VCPs – and to significantly enhanced low-altitude coverage throughout the CONUS.

To assess these requirements, NOAA's Office of Oceanic and Atmospheric Research (OAR) conducted and coordinated a two-year research program to quantify NWS mission benefits associated with the SENSR objective requirements, and technical approaches – specifically phased array radar – for achieving these. Although NOAA withdrew from the SENSR program in 2018 - owing to its assessment that the SENSR requirements development process and implementation schedule were inconsistent with NOAA's operational constraints - the OAR research remains highly relevant to NOAA's follow-on research-to-operations strategy for re-capitalizing the national operational weather network [NOAA/NWS/OAR 2020].

This report summarizes the OAR SENSR feasibility study. Research activities encompassed measurements, analysis and modeling using conventional and active-array radar testbeds, data driven simulators, storm observations and high-resolution numerical prediction models. Key components of the effort were:

(i) Assessment of the operational forecasting and warning benefits of rapid-scan, polarimetric phased array radar observations. This assessment exploited storm observations and analysis, numerical weather prediction (NWP) model observing system simulation experiments, and real radar-data assimilation experiments;

(ii) Analysis of operational benefits that might be realized through improved low-altitude weather coverage. This enhanced coverage could result from deployment of "gap-filler" meteorological radars, and/or the availability of high-quality weather observations from future air traffic surveillance radars;

(iii) High fidelity simulation and analysis to assess data quality impacts of candidate phased array radar architectures, and strategies for managing radar scanning timelines to meet SENSR's volume scan update rate goals;

(iv) Assessment of techniques to compensate for inherent polarimetric variable estimate biases introduced by phased array radar electronic beam steering. These include, but are not limited to, "geometric biases" as the array is steered off broadside. Our research considers approaches to calibration, bias-correction and likely residual errors after appropriate compensation techniques are applied;

(v) Analysis of the unique challenges associated with a cylindrical polarimetric phased array radar (CPPAR). While CPPAR eliminates geometric biases of the polarimetric variables, it raises other issues such as possible surface "creeping wave" interference, challenges in achieving sufficiently low antenna sidelobes, and electronic scanning constraints that reduce the flexibility of volume scanning patterns;

(vi) Assessment of engineering issues and the operational benefits of an all-digital active array architecture. This may enable more effective array calibration and compensation techniques, and facilitate efficient scanning through the use of simultaneous receive beams steered at widely separated angles;

The aim of this research is to refine and justify – in terms of National Weather Service mission benefit – the "objective" meteorological radar technical requirements defined in [NOAA/NWS, 2015] and further developed through the SENSR program. If validated, these requirements will be provided to industry as a basis for procurement of one or more prototypes of a next-generation, operational meteorological phased array radar (NexPAR) for follow-on testing and subsequent full-rate production contract.

Sections 2-8 of this report provide research summaries from the contributing principal investigators, ordered as discussed in the previous paragraph. In section 9 we summarize findings and provide recommendations for ongoing research, demonstration and transition to operations.

References:

NOAA/NWS, 2015: Radar Functional Requirements, NOAA/NWS Internal Rep., 58pp. https://www.roc.noaa.gov/WSR88D/PublicDocs/NOAA_Radar_Functional_Requirements_Final_Sept%202015.pdf

NOAA/NWS/OAR: Weather Radar Follow On Plan: Research and Risk Reduction to Inform Acquisition Decisions, 2020, (in review)

2. Warning and Forecast Benefits for Rapid, Flexible Scanning

The figure below depicts a notional NexPAR concept of operations, consistent with the analysis and experiments described in this report. PAR-enabled volume-coverage-patterns (VCPs) providing surface to storm top observations approximately once per minute will significantly improve the efficacy of NWP radar data assimilation and associated warning processes (Section 2.1). Radar-derived, real time observations of "clear air" winds in the near-storm environment will further improve performance (Section 2.2). Adaptive or "targeted" ultra-high update scanning of certain storm volumes, and/or RHI depictions of storm structures may also enhance operational warning performance.

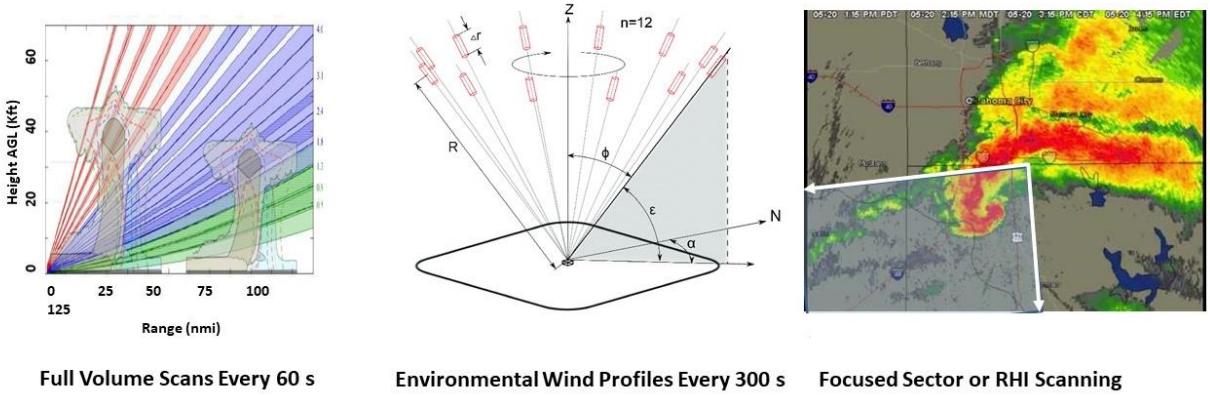

Notional NexPAR scanning concept of operations.

Section 2.1 describes experimental studies of the impact of more rapid volumetric radar observations on NWP data assimilation and "warn on forecast system (WoFS)" performance. This analysis includes unique findings resulting from the direct assimilation of NSSL phased array radar data to show the benefits of fast scans for convective storm forecasting. In section 2.2 we present Observing System Simulation Experiments (OSSE) demonstrating how PAR's capability to provide significantly expanded "clear air" environmental wind observations improves performance when assimilated into NWP-based warning processes. A method for "targeting" radar observations to meteorologically significant storm volumes is presented and experiments assessing associated benefits for storm modeling are described. Rapid-scan polarimetric observations of severe storms obtained with NSSL's experimental WSR-88D (KOUN) are analyzed in section 2.3. These further demonstrate likely NexPAR benefits for severe weather warnings including downbursts and flash-flooding events. Finally, in section 2.4 we describe OSSEs that demonstrate the broader benefits of NexPAR operational concepts for convective weather nowcasts supporting U.S. commercial aviation operations.

2.1 Impact of Assimilating Phased Array Radar Observations on Convective-scale Numerical Weather Prediction Model for Severe Weather Forecasts[1]

The NOAA National Severe Storms Laboratory is developing both PAR technologies with dual-polarization capability as a potential replacement for the aging WSR-88D network, and the Warn-on-Forecast System (WoFS). The goal of WoFS is to provide National Weather Service (NWS) forecasters with storm-scale numerical weather prediction (NWP) model-based probabilistic guidance to aid in extending lead times for severe thunderstorm and associated hazards, with reduced false alarms. Radar data are critical for WoFS data assimilation (DA) and modeling. It is paramount therefore to evaluate the impact of next generation PAR technology on storm-scale modeling with rigorous testing using a variety of severe weather scenarios.

Optimal temporal frequency PAR volume-scan for WoFS

The National Weather Radar Testbed (NWRT) PAR located in Norman, OK collected observations from the 31 May 2013 OK tornadic supercell event. PAR successfully interrogated the El Reno storm from convective initiation through the entire evolution of the tornado with the exception of a 5-minute period from 2216–2221 UTC when the horizontal scanning sector was shifted ~10°. Volumetric data intervals incrementally increased from about 45 s to 69 s before the sector shift owing to additional elevation angles being added to the volume scans. After the sector shift, volume scanning intervals remained nearly constant at about 71 s. These frequent volumetric data provided an opportunity to evaluate the impact of temporal frequency of PAR observations in an experimental version of WoFS at 1-km horizontal grid spacing. The NWRT PAR began scanning this event more than an hour before the first (and strongest) tornado developed near El Reno, OK and scanned most of the tornadic supercell's evolution.

For this study, three sets of experiments were conducted using various cycling and data frequencies to synchronously and asynchronously assimilate these observations to produce analyses and very short-term forecasts of the El Reno supercell. All experiments used the WRF-ARW model and 4DEnSRF DA system (Wang et al. 2013). The first set of experiments are designed to emulate past OSSEs that explored the impact of radar DA cycling intervals on storm-scale analyses and forecasts (e.g., Zhang et al. 2004; Xue et al. 2006). These experiments synchronously assimilate PAR data every 1, 3, 5, and 15 min and are named PAR1Cyc1, PAR3Cyc3, PAR5Cyc5, and PAR15Cyc15, respectively (Fig. 2.1.1). Ensemble forecasts are initialized from each of those experiments every 15-min with WRF history files output every 5 minutes through 0000 UTC the next day. Another synchronous DA experiment is conducted to demonstrate the potential role of adaptive cycling intervals in a future WoFS using PAR observations. During the early stages of storm development, the 1-min DA cycling interval is used to spin up the storm in the model before switching to the 15-min DA cycling interval for the remaining time (i.e., 2200 to 2300 UTC). This experiment is named Cyc1+Cyc15 and is compared to the PAR15Cyc15 experiment, which is the current WoFS DA cycling frequency for real-time demonstration. The final set of experiments compare the impact of asynchronously assimilating 1-min PAR volumetric data using 4DEnSRF with a 5-min cycling interval (PAR1Cyc5) to the previous PAR5Cyc5 experiment. For this asynchronous experiment, the

[1] Principal Investigators: Nusrat Yussouf (OU CIMMS and NSSL), Youngsun Jung and Ming Xue (OU CAPS)

assimilation window is equal to the cycling interval, so all observations between -2.5 min and +2.5 min are assimilated for each DA cycle. Forecasts of low-level reflectivity and mid-level updraft helicity are subjectively evaluated and objectively verified using spatial and object-based techniques.

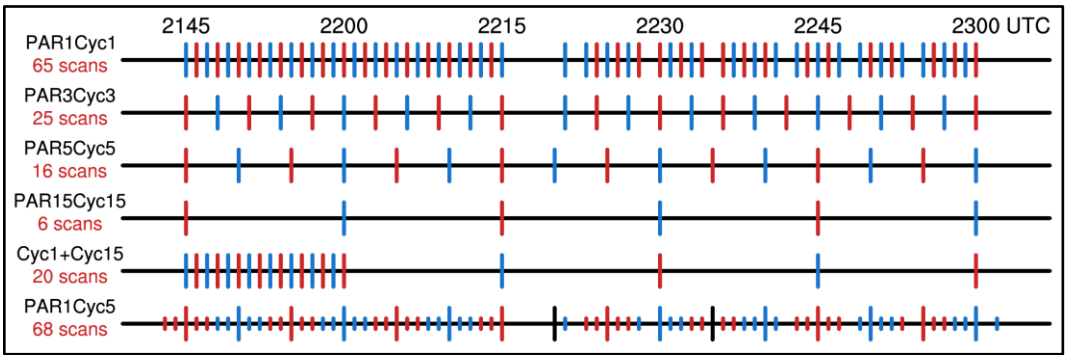

Figure 2.1.1: Schematic of the data assimilation experiments. Red and blue vertical lines indicate the times PAR volumetric data is assimilated. Longer and shorter vertical lines in PAR1Cyc5 represent the centers of the data assimilation windows and PAR volumetric data, respectively.

Synchronous DA cycling interval experiments

Using neighborhood-based verification, PAR1Cyc1 has the largest average Ensemble Forecast Skill Score (eFSS) values for neighborhood widths larger than ~16 km (Fig. 2.1.2a). In fact, PAR1Cyc1's eFSS asymptotes to the largest eFSS value for the largest neighborhood widths as a result of having the smallest frequency bias within the subdomain, likely due to having less spurious convection (Fig. 2.1.2a). Conversely, PAR15Cyc15 has the smallest eFSS values for all neighborhood sizes at least partially owing to having the most spurious convection. For neighborhood widths smaller than 16 km, PAR1Cyc1, PAR3Cyc3, and PAR5Cyc5 have similar eFSS values. Overall, the results from the reflectivity forecasts indicate that more frequent PAR DA can improve forecasts by more quickly developing convection in the correct locations while removing spurious convection.

To provide further insight, a reference forecast skill score, FSS_{ref}, is computed using the observed frequency, f_o, to determine the halfway point between a random forecast and a perfect forecast. The neighborhood widths at which eFSS = FSS_{ref} are determined for forecasts every 5-minutes within the first hour after initialization starting with the 5-min forecast. The best possible neighborhood width at which eFSS = FSS_{ref} is 0 km, which means eFSS $\geq$ FSS_{ref} when the neighborhood size is one gridpoint.

While all of the experiments' forecasts improve with later initialization times, shorter cycling interval experiments generally achieve FSS_{ref} at smaller neighborhood widths than longer cycling interval experiments (Fig. 2.1.2b). In fact, during the first hour after all initializations, PAR1Cyc1's forecasts outperform the other experiments' forecasts for most forecast output times (Fig. 2.1.2b). For forecasts initialized at 2300 UTC, PAR3Cyc3 and PAR5Cyc5 achieve FSS_{ref} at smaller neighborhood widths than PAR1Cyc1 starting around 2345 UTC. However, this result is due to a combination of PAR3Cyc3 and PAR5Cyc5 forecasting more spurious convection, as indicated by the smaller eFSS values at the larger neighborhood widths (Fig.

2.1.2b), and PAR1Cyc1 not forecasting enough new convection to the west of the El Reno storm.

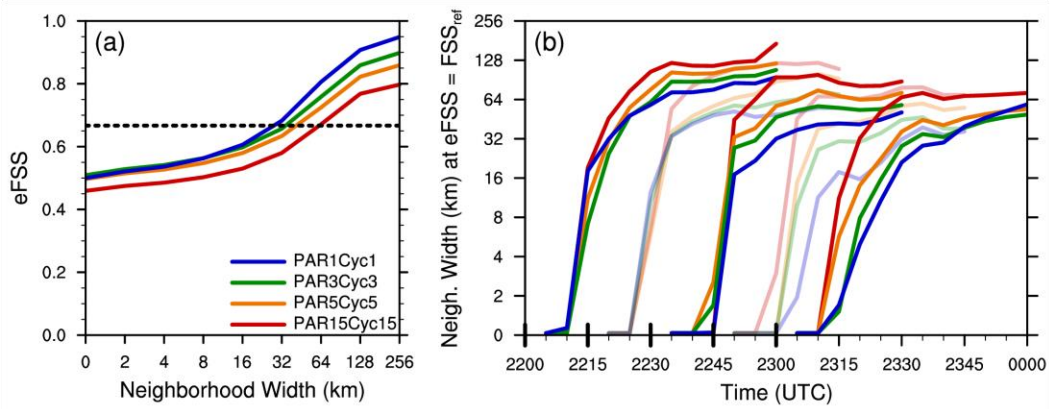

Figure 2.1.2: (a) Average eFSS for each neighborhood width (km) using all five 1-h forecasts of 2-km MSL reflectivity > 35 dBZ, and (b) neighborhood widths (km) where eFSS =FSS_{ref} for each forecast output time. Short black lines on the x-axis in (b) demarcate the forecast initialization times.

All experiments, except for PAR15Cyc15, forecast greater than 50% probabilities of 2–5-km UH > 400 m^2 s^{-2} over the areas of the observed mesocyclones (e.g., azimuthal wind shear > 0.012 s^{-1}) responsible for the El Reno and Oklahoma City tornadoes with only 15-min of DA (Fig. 2.1.3a-d). More specifically, PAR1Cyc1 is the only experiment that has probabilities greater than 95% for a portion of the El Reno storm's observed azimuthal wind shear track (Fig. 2.1.3a). Both the probabilities (Fig. 2.1.3a) and UH magnitudes (Fig. 2.1.3e) reveal that PAR1Cyc1 forecasts less spurious rotation to the north and south of the El Reno storm with PAR15Cyc15 having the most spurious rotation. Except for the spatial differences, all of the experiments forecast similar maximum 2–5-km UH intensities (Fig. 2.1.3e-h).

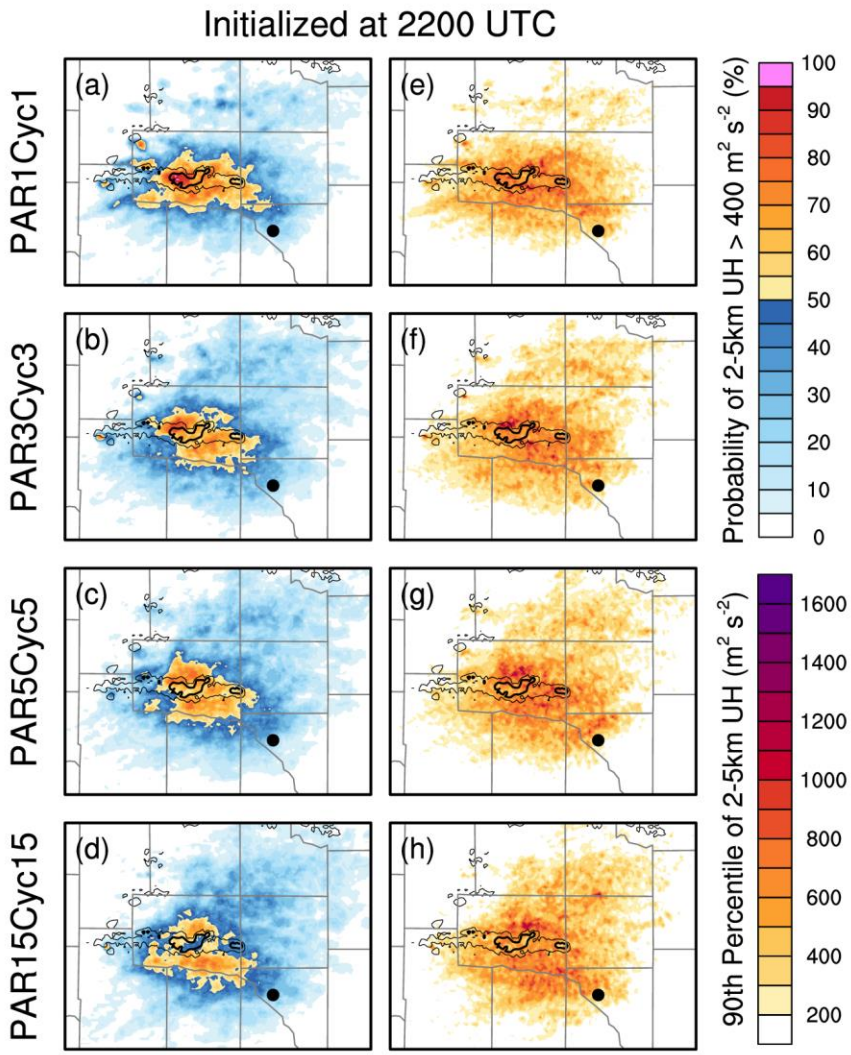

Figure 2.1.3: 0–2-h forecasts initialized at 2200 UTC of (a-d) probabilities of 2–5-km UH greater than 400 m^2 s^{-2} and (e-h) ensemble 90th percentile intensities of 2–5-km UH (m^2 s^{-2}). Black contours are azimuthal-wind shear at 0.006 s^{-1} and 0.012 s^{-1} accumulated from 2200 to 0000 UTC. The black dot is the location of the NWRT PAR.

Example of adaptive cycling intervals

By assimilating PAR volumetric data more frequently for the first 15 min of the DA period, Cyc1+Cyc15 is able to produce better reflectivity forecasts of the El Reno storm than PAR15Cyc15. Subjectively, Cyc1+Cyc15's forecasts have less spurious convection at all forecast time. Also, with less propagation to the southeast, Cyc1+Cyc15's El Reno storm is latitudinally more correct than the storm in PAR15Cyc15's forecasts. Objectively, Cyc1+Cyc15's reflectivity forecasts have substantially higher eFSS values at all scales and achieve FSS_{ref} at substantially smaller scales at most forecast times (Fig. 2.1.4).

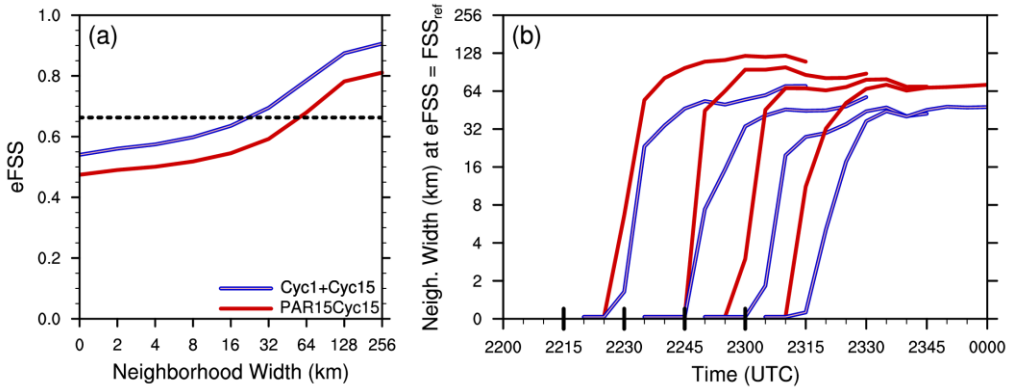

Figure 2.1.4. Same as Figure 2.1.2, but for Cyc1+Cyc15 and PAR15Cyc15.

Probability and intensity forecasts of 2–5-km UH also reveal large differences between the two experiments. Cyc1+Cyc15 has less spurious rotation to the north and south of the azimuthal wind shear track and higher UH probabilities associated with the observed rotation in the northeastern part of the subdomain (Fig. 2.1.5). Also, Cyc1+Cyc15's swaths of UH probabilities and intensities are more precise and closer to the azimuthal wind shear track than PAR15Cyc15's UH swath, which ends up farther to the south. By assimilating more PAR volumes earlier in the DA period, Cyc1+Cyc15 subjectively and objectively outperforms PAR15Cyc15. These results demonstrate the potential benefits of adaptive DA cycling intervals to WoFS using PAR observations.

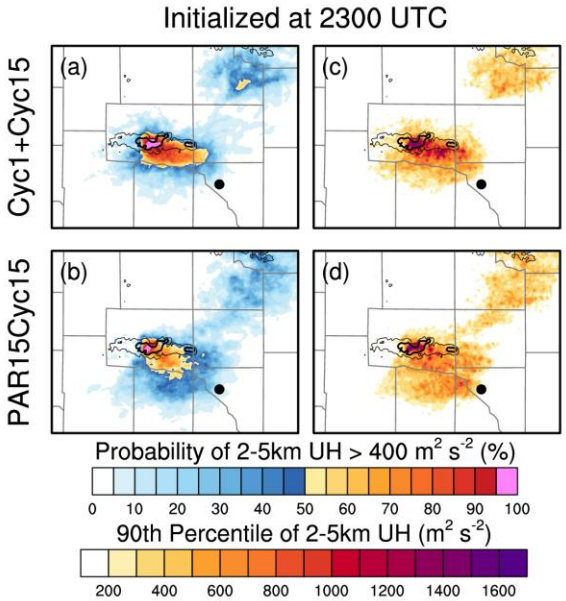

Figure 2.1.5. Same as Fig. 2.1.3, but for Cyc1+Cyc15 and PAR15Cyc15.

Asynchronous DA experiment

Objectively, PAR1Cyc5 has slightly better eFSS values at all scales than PAR5Cyc5. Also, PAR1Cyc5's eFSS values reach FSS_{ref} at smaller scales than PAR5Cyc5 at most forecast times. For 2–5-km UH, PAR1Cyc5 and PAR5Cyc5's forecasts are mostly similar; however, some notable differences do exist. For example, 1-h forecasts launched from 2300 UTC reveal

PAR1Cyc5 results in UH probability and intensity swaths being spatially more centered on the azimuthal wind shear track as indicated by higher probabilities (i.e., > ~80%) covering more of the observed rotation track area. Overall, the differences are minimal between the PAR1Cyc5 and PAR5Cyc5 experiments, but asynchronously assimilating additional PAR volumes using the same DA cycling interval with 4DEnSRF does generally improve forecasts of the El Reno storm and surrounding areas. Asynchronous DA is a potential way to improve analyses and forecasts without having to frequently stop the model to assimilate ~1-min PAR volumetric data.

Summary and Future Work

Results from the synchronous DA experiments showed that more frequently assimilating PAR data can more quickly spin up storms and suppress spurious convection in analyses. Specifically, assimilating PAR volumetric data every 1-min produces better analyses and forecasts of the El Reno storm than assimilating PAR data less frequently at 3-, 5-, and 15-min intervals. Also, the forecast skill changes going from a 1-min to 3-min to 5-min cycling interval were smaller than when going from a 5-min to 15-min cycling interval. The results from these experiments can likely be generalized to conclude that more frequent DA cycling can lead to more accurate analyses and forecasts at longer lead times. As Cyc1+Cyc15 demonstrated, using shorter cycling intervals when convection is developing or quickly evolving before switching to a longer cycling interval to maintain current convection is a way to substantially improve analyses and forecasts at longer lead times. The result from this experiment suggests that adaptive cycling intervals could potentially be beneficial to storm-scale DA systems with non-continuous cycling like the WoFS. Also, adaptive cycling intervals are computationally less expensive (Table 2.1.1) and are a potential solution to any ensemble spread or imbalance issues since frequent DA cycling would be used less often and only in areas where it would have the greatest impact.

Experiment	Data Assimilation	Forecast	Total Core-Hours
PAR1Cyc1	378	2150	2527
PAR3Cyc3	146	1498	1643
PAR5Cyc5	92	1368	1461
PAR15Cyc15	34	1296	1331
Cyc1+Cyc15	116	1541	1657
PAR1Cyc5	281	1944	2226

Table 2.1.1. Total computational costs (core-hours) during the 75-min period of DA cycling for each experiment. For reference, the five forecasts for each experiment consumed an estimated combined total of 7200 core-hours.

The results from this study have a direct implication on the design of the next version of the experimental WoFS. This study demonstrates that an experimental WoFS at 1-km grid spacing with 1-min DA cycling can spin up storms faster in analyses while suppressing spurious convection, lending itself to the use of frequent (~1 min) PAR volumetric data for the next generation of the WoFS. To save computational resources, the WoFS could incorporate an adaptive cycling interval technique to assimilate more frequent PAR observations only when necessary. For example, when maintaining slowly-evolving convection in analyses and forecasts, less frequent PAR observations would be sufficient. However, when accurate analyses are needed in less time, spurious convection exists in the background forecasts, or convection is developing or quickly evolving, the optimal temporal frequency of PAR observations for storm-scale DA would only be limited by computational resources. Therefore, the optimal temporal frequency of PAR volumetric data would be situationally dependent for the WoFS. With the deployment of NSSL's Advanced Technology Demonstrator, the first full-scale, S-band, dual-polarization PAR, future work will continue to explore the benefit of rapid-scan PAR on an experimental WoFS using a variety of severe weather events. Future work will also examine the benefits of adaptive cycling intervals on WoFS depending on storm's maturity. We will also explore the benefits of assimilating "clear air" radial velocity observations from pre-convective and near-storm environments using increased radar dwell times. Assimilating "clear air" radial velocity observations will likely improve WoFS storm motion forecasts and potentially CI forecasts.

WSR-88D vs. NWRT PAR

Experiment design

In the second part of this study, we evaluated the benefit of high temporal resolution PAR data over the WSR-88D data on the prediction of the aforementioned 31 May 2013 central Oklahoma event. This is an extension of Supinie et al. (2017) with more insights on the mechanisms behind the differences between the WSR-88D and PAR experiments. The same experiment domain and configurations in the preceding sub-section are used with 4DEnSRF. The observations assimilated are the Oklahoma Mesonet, the NWRT PAR and the operational WSR-88D (KTLX) (Fig. 2.1.6).

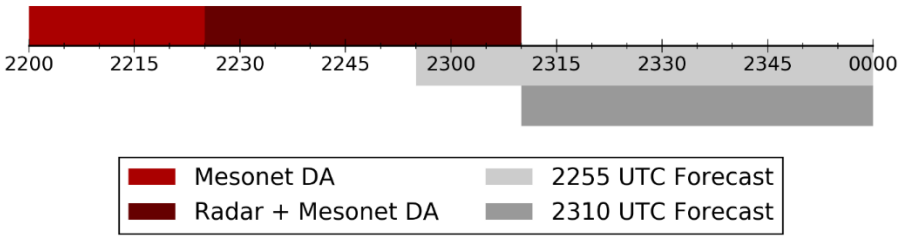

Figure 2.1.6: Schematic and timeline of the experiment. The times shown are in UTC.

Experiment Results

Several ensemble DA and forecast experiments were conducted. One experiment uses only data from KTLX, and another uses only data from the PAR. Both experiments apply relaxation to prior spread (RTPS; Whitaker and Hamill 2012) covariance inflation once at the end of the assimilation window. In the PAR experiment, radar observations are assimilated in order by volume, then by elevation angle. To determine the optimal use of PAR observations in the EnSRF, two additional experiments are conducted changing the order of the radar observations that are assimilated. The first experiment assimilates those PAR observations in reverse order, meaning later volumes and higher elevation angles are assimilated first. The experiment is called "PAR-reversed." In order to determine the effect of the large number of PAR observations on the ensemble spread, another experiment is conducted in which RTPS inflation is applied after assimilating each volume of PAR data. We call this technique "Inter-Volume Covariance Inflation" (IVCI), and thus this experiment is named "PAR+IVCI."

First, we examine root mean square innovations (RMSIs) and the total spreads computed in observation space (Fig. 2.1.7). Statistics are computed for observations at all times considered in the analysis and wherever reflectivity ≥ 15 dBZ in either the ensemble mean or the observations, except where the observations are missing. The forecast RMSI (Fig. 2.1.7a) for each analysis decreases from ~21 dBZ to ~10 dBZ over the course of the DA period. The RMSI in the KTLX experiment is always 2-4 dB less than in the PAR-based experiments. This is partially a result of the zero-reflectivity observations added to the PAR volumes outside the PAR scan area and where KTLX composite reflectivity is > 0. In this case, the PAR, PAR+IVCI, and PAR-reversed analyses are removing hydrometeors from the low levels of the atmosphere, but not the anvil region aloft, where the no zero-reflectivity observations have been added. This results in the remaining hydrometeors falling into the area where the zero-reflectivity observations have been added, which appears in the RMSI statistics. With IVCI, the total spreads of PAR+IVCI for both forecasts and analyses are greatest among experiments (Fig. 2.1.7c, d).

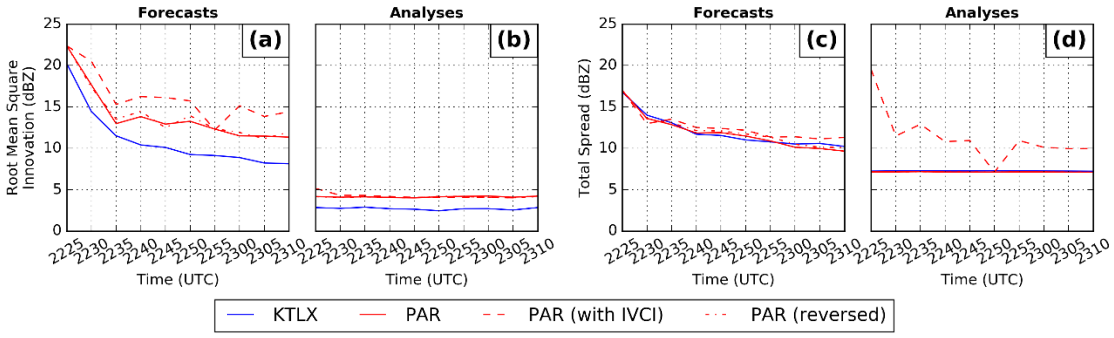

Figure 2.1.7: The forecast and analysis root-mean-square innovation (a) and (b), respectively, and their total spread (c) and (d).

The UH swath from the 2255 UTC initialization shows UH probability coinciding with the MRMS mid-level rotation tracks for the main supercell in all three experiments (Fig. 2.1.8a, c, e). The PAR, PAR+IVCI, and PAR-reversed experiments show a higher UH probability than the KTLX experiment over the early portion of the track of the El Reno supercell. Additionally, the PAR+IVCI experiment has higher probabilities than the other experiments to the south of the observed rotation track. Additionally, the swath in the PAR-reversed experiment has a more easterly orientation, as opposed to the other PAR experiments, which have a more east-southeasterly orientation. The westernmost portion of the MRMS rotation track is associated with a secondary supercell that develops to the west of the El Reno supercell, and none of the 2255 UTC forecasts capture this development. Furthermore, the 2310 UTC initializations are similar, with the PAR and PAR+IVCI experiments having a higher probability of UH from the main supercell than the KTLX experiment. As in the 2255 UTC initializations, the PAR+IVCI experiment has much higher probability to the south of the observed rotation track than the other experiments. Also, the swath in the PAR-reversed experiment has a more easterly orientation than the other PAR-based experiments, same as in the 2255 UTC initializations. However, one difference from the 2255 UTC initializations is the mesocyclone from the secondary supercell that develops west of the El Reno supercell is better captured with higher probabilities in the PAR and PAR+IVCI experiments than in the KTLX experiment. Additionally, the track forecast in the PAR and PAR+IVCI experiments is farther south and faster than the track in the KTLX experiment.

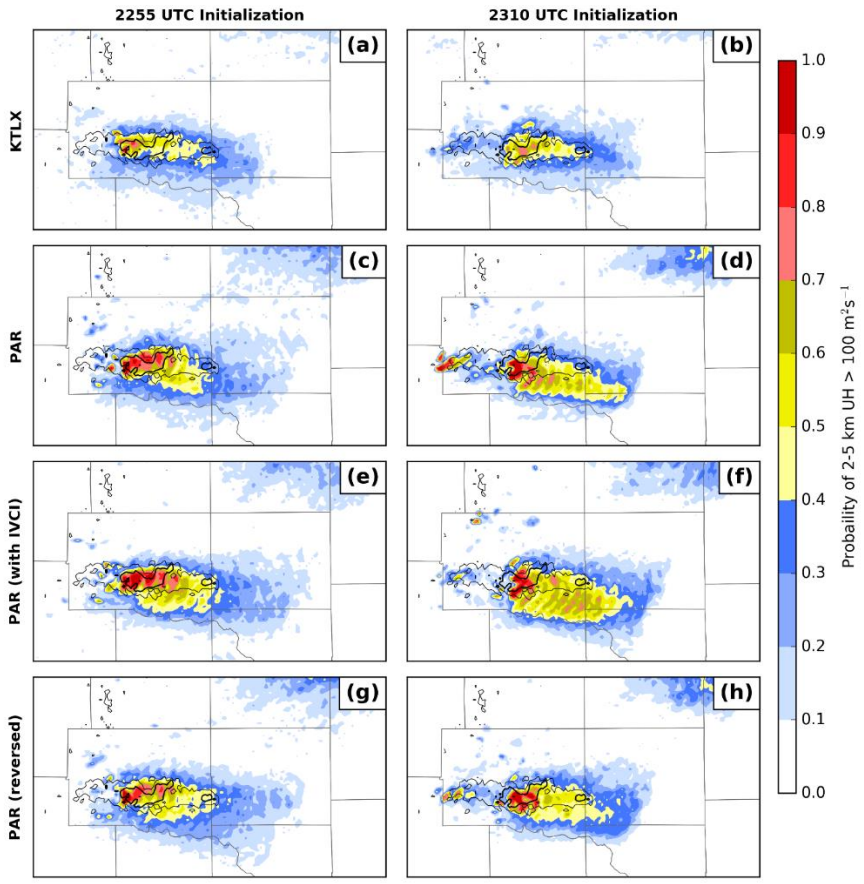

Figure 2.1.8: Probability swaths of 2-5 km updraft helicity > 100 m^2 s^{-2} for forecasts initialized at 2255 UTC (left column) and 2310 UTC (right column) for the KTLX (a,b), PAR (c,d), PAR (with IVCI; e,f), and PAR (reversed; g,h) experiments. Swaths begin at forecast initialization and end at 0000 UTC. The MRMS mid-level azimuthal shear track is contoured in black. The thin and thick lines are the 0.006 and 0.012 s^{-1} contours, respectively.

We look at the contributions to the increments from each PAR volume to determine which volumes affect the model state the most and if all volumes are necessary (Fig.2.1.9). For all three of the PAR experiments, the first three volumes of PAR data that are assimilated are responsible for most of the changes to the model state, though the other two volumes contribute at least a small amount. For the PAR and PAR+IVCI experiments, these are the 2308-2310 UTC volumes, but for the PAR-reversed experiment, this is the 2310-2312 UTC volumes. This behavior is the superposition of two patterns. The first is a temporal localization weight which increases from 0.38 at the first volume to 1 at the third volume and then decreases back to 0.38 at the fifth volume. Thus, the first volume has the same weight in the temporal localization as the fifth volume, even though the first has much more of an impact on the analysis state (compare Fig. 2.1.9 b, g, l to Fig. 2.1.9 f, k, p). The second pattern is a general decrease in the magnitude of covariance in the ensemble state as more observations are assimilated throughout the DA window. This is a natural consequence of ensemble DA, and the additional covariance inflation in the PAR+IVCI experiment is designed to counteract this. However, this does not appear to

have the expected effect, as the 4th and 5th volumes assimilated do not have significantly more effect in the PAR+IVCI experiment vs. the PAR experiment (compare Fig. 2.1.9 e, f to j, k). One potential explanation involves thinking of covariance between two variables as the product of their correlation and spread in both variables. In current ensemble DA, the covariance reduction is typically understood as primarily a reduction in spread in the ensemble state. In fact, the current covariance inflation algorithms inflate the ensemble covariance by increasing the spread in the ensemble state (in the case of RTPS, by multiplying the ensemble perturbations from the mean by some factor greater than 1). However, the filter can change the ensemble correlations, as well as the spread. Therefore, what may be happening in these experiments is that the large number of PAR observations decreases the ensemble correlation, which cannot be rectified by increasing the spread. More details can be found in Supinie et al. (2020).

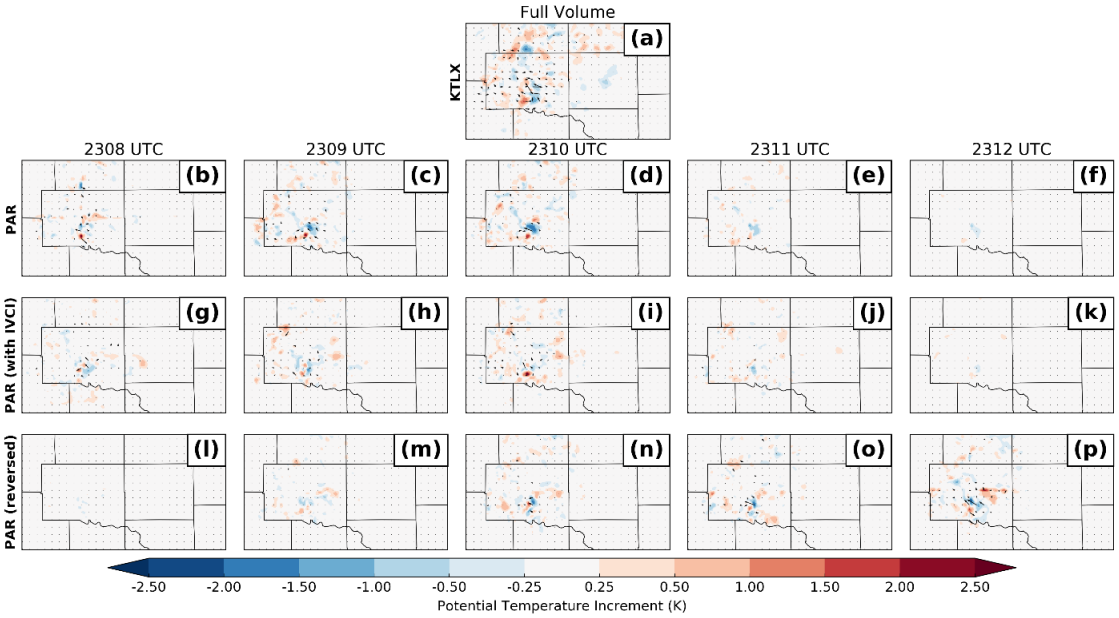

Figure 2.1.9: Ensemble mean increment of 2-5 km mean potential temperature at the 2310 UTC analysis from for the PAR (b-f), PAR+IVCI (g-k), and PAR_reversed (l-p). The full increments from the KTLX experiment are given in (a). Note that none of these include increments from the Oklahoma Mesonet DA.

Summary and Future Work

The study examined the benefit of assimilating PAR observations over the current WSR-88D observations and provides insight into how differences between the two experiments arise in the 4DEnSRF. As in previous studies, the results show more rapid spin-up of convection using 1-min PAR data as compared to ~5-min WSR-88D data. The probability of updraft helicity (UH) is generally greater in experiments that assimilate PAR data than the KTLX experiment, which is primarily driven by a stronger updraft in the PAR-based experiments. This in turn is driven by a combination of the DA directly creating a stronger updraft and the DA also creating a stronger

mid-level temperature perturbation associated with the updraft. This allows the updraft strength to be maintained throughout the forecast.

When the 4DEnSRF is used to assimilate multiple volumes of PAR, it is found that most of the changes to the model state come from the first three volumes of data that are assimilated. Assimilating later volume first (PAR-reversed) improves the UH track forecast, suggesting the benefit of more recent observations. The IVCI method which applies RTPS between volumes of PAR data helps increase the ensemble spread but in also introduces larger bias. This implies that a more advanced inflation method that can maintain the spread while maintaining reliable covariances would be necessary.

Finally, more testing of the impact of PAR data on different storm modes, such as MCSs and single- and multi-cell modes producing tornadoes, hail, damaging wind, and flash flooding is needed for the conclusions to be generalized and to find the optimal configurations for the future Warn-on-Forecast System.

Dual-Polarization Phased Array Radar using Rapid Scan KOUN as Proxy

Experiment design

Polarimetric (dual-pol) observations and rapid-update data assimilation (DA) are both critical components of the Warn-on-Forecast System (WoFS) vision outlined nearly a decade ago to provide forecasts of convective storm hazards before their occurrence. This study investigates the impact that dual-pol observations have on convective scale forecasts and how this impact changes over different DA windows.

The same experiment domain and configurations used above are used with a storm-scale grid initialized at 2100 UTC 31 May (Fig. 2.1.10). A 1-hour spin-up forecast is run from 2100 UTC to 2200 UTC. Data assimilation with the EnSRF begins at 2200 UTC and continues with 5-minute assimilation cycles through 2300 UTC, or approximately 3 minutes before the start of the El Reno tornado. To assess how the assimilation of dual-pol variables may help reduce the number of cycles required to produce a reasonable forecast, three separate ensemble forecasts are launched from two experiments, one assimilating Z and V_r (EXPZ), and one assimilating Z_{DR} in addition to Z and V_r (EXPZZDR).

On that day, the KOUN radar has taken sector scans to provide more rapid updates (~ 2 min) of the radar volume while observing convective storms of interest, including on 31 May 2013 (Kuster et al. 2017; Kuster et al. 2019). The sectors in this case cover approximately 110 degrees and shift from the west-northwest to north over the case period following the movement of the mesocyclone of the El-Reno – Oklahoma City tornadic supercell.

a)

Experiment Name	EXPZ	EXPZZDR
Assimilated Observations	$Z + V_r$	$Z + V_r + Z_{DR}$

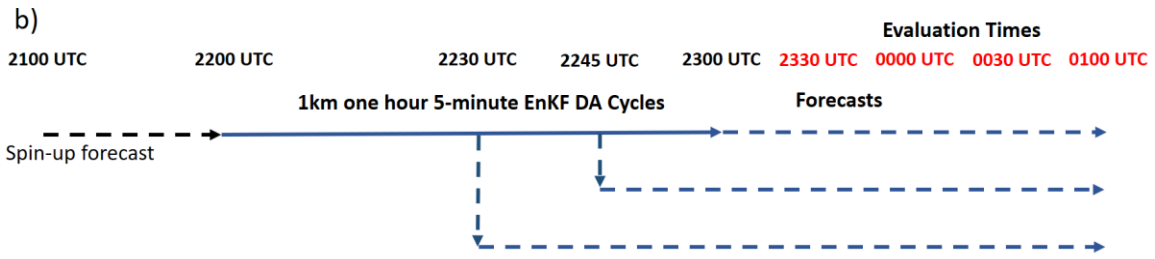

Figure 2.1.10: (a) Combinations of observations assimilated in two experiments and (b) schematic of the experiment and timeline of the experiment.

Experiment Results

The overall forecast storm evolution and progression is assessed by probabilistic forecasts of *Z*. Fig. 2.1.11 contains the neighborhood (5-km) ensemble probability of *Z* greater than 15 dBZ at 0000 UTC and 0100 UTC, with the threshold of 15 dBZ chosen to assess the overall predicted coverage of precipitation. Both forecast experiments initialized at 2230 UTC produce forecasts of the El Reno storm that generally move at a slightly faster speed and are located in the same vicinity of the observed storm as it passes east over Oklahoma City. Additional convection develops to the northwest of the storm but does not replicate the repeated initiation and training of thunderstorms over the Oklahoma City region seen in the observations. The forecasts of the El Reno storm overall are very similar between two experiments. The experiments, however, differ more significantly in the forecast of the northern Stillwater storm. The storm dissipates rapidly by 0000 UTC in EXPZ_2230 (Fig. 2.1.11a), the remaining convection at 0100 UTC is not identifiable as a separate storm from the El Reno supercell. In contrast, the convection is more sustained for a longer period of time in EXPZZDR_2230, with a weak but existent cell at 0100 UTC (Fig. 11d). Similar patterns emerge in the forecasts launched at the later 2245 UTC and 2300 UTC initialization times (Figs. 2.1.11b-c, e-f).

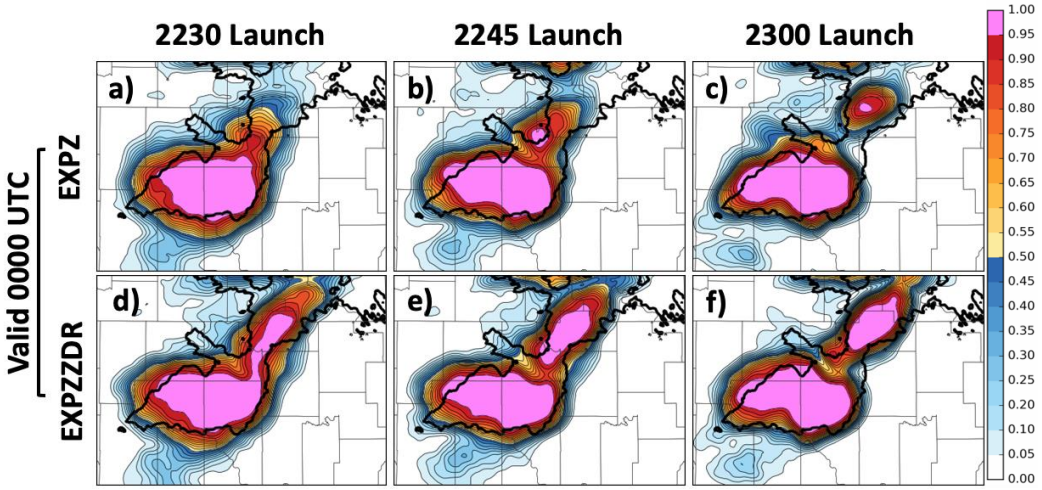

Fig. 2.1.11. Probability of reflectivity (Z) greater than 15 dBZ for EXPZ valid at 0000 UTC 1 June 2013 from the forecasts initialized (launched) at (a) 2230 UTC 31 May 2013, (b) 2245 UTC, and (c) 2300 UTC and for (d)-(f) EXPZZDR.

Swaths of probabilities of hail are considered in Fig. 2.1.12. The probability of hail with a diameter greater than 5 mm at the surface is calculated every 5 minutes over the same 2300 to 0100 UTC window. The hail diameters are found using the Thompson hail method (Thompson et al. 2018), which calculates the largest observable hailstone based on the hail particle size distribution (PSD) at each grid point. The hydrometeor classification algorithm (HCA) of Park et al. 2009 is used with the dual-pol observations to determine where hail may exist, and these regions are overlaid on the probability plots. The EXPZZDR forecast launched at 2230 UTC (Fig. 2.1.12 d) produces greater hail probabilities later into the forecast and further to the east along the observed HCA hail swath compared to EXPZ (Fig. 2.1.12 a). The forecast hail probabilities in EXPZZDR_2245 (Fig. 2.1.12e) have a similar but smaller improvement compared to EXPZ_2245 and the forecast probabilities in the two experiments launched at 2300 UTC are very similar (Figs. 2.1.12c,f). There is a more significant increase in probabilities between the two sets of experiments for the Stillwater storm. There are much larger swaths of higher probabilities of hail compared to the observed HCA swaths for the 2245 UTC (Fig. 2.1.12e) and 2300 UTC (Fig. 2.1.12f) forecasts. The 2300 UTC forecast in particular has a larger area of greater than 90% probability of hail. The Stillwater storm is weaker and smaller compared to the El Reno storm but still produces severe hail, and the EXPZZDR results capture this better.

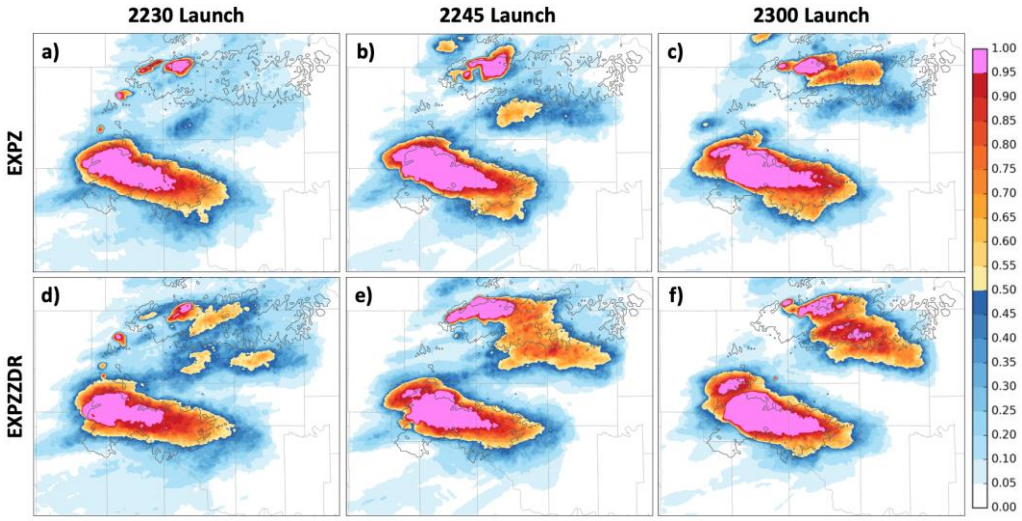

Fig. 2.1.12. Swaths of the probability of forecast surface hail max diameter greater than 5 mm from 2300 UTC 31 May 2013 to 0100 UTC 1 June 2013 for EXPZ forecasts initialized (launched) at (a) 2230 UTC 31 May 2013, (b) 2245 UTC, and (c) 2230 UTC as well as for (d) – (f) EXPZZDR. Areas where radar observations are classified as hail using the Park et al. (2009) hydrometeor classification algorithm (HCA) are outlined in black.

To understand how EXPZZDR maintains the northern, Stillwater storm longer for all forecasts launch times compared to the EXPZ forecasts, where the storm dissipates quickly, we examine the analyzed surface temperature (T) and dewpoint temperature (T_D) at the analysis times used to initiate the forecasts at 2230 UTC and 2300 UTC (Fig. 2.1.13). The surface T at both analysis times is lower in the cold pool of the El Reno and Stillwater storms in EXPZ compared to EXPZZDR. The differences are more significant at 2300 UTC, and the Stillwater storm in EXPZ at this time has the coldest temperatures in the cold pool, overall. The surface T_Ds are also lower in the EXPZ experiments compared to the EXPZZDR experiments at both times and the lowest values of T_D are again seen in the cold pool of the Stillwater storm in EXPZ_2300. While a cold pool is necessary to maintain the structure of a supercell, a cooler and drier cold pool will lead to a decrease in storm intensity as warm, moist air is cut off from and unable to maintain a mature, strong storm updraft. Cooler, drier cold pools are the result of too many small drops that evaporate and cool the air in the storm downdrafts. This implies that the assimilation of Z_{DR} improves the PSDs and microphysical state of the analyzed storms in the EXPZZDR experiments and doesn't lead to as many smaller drops. The EXPZ forecasts initialized from these analyses, particularly the EXPZ_2300 analysis for the Stillwater storm, lead to storms that are seen to dissipate more quickly compared to observations.

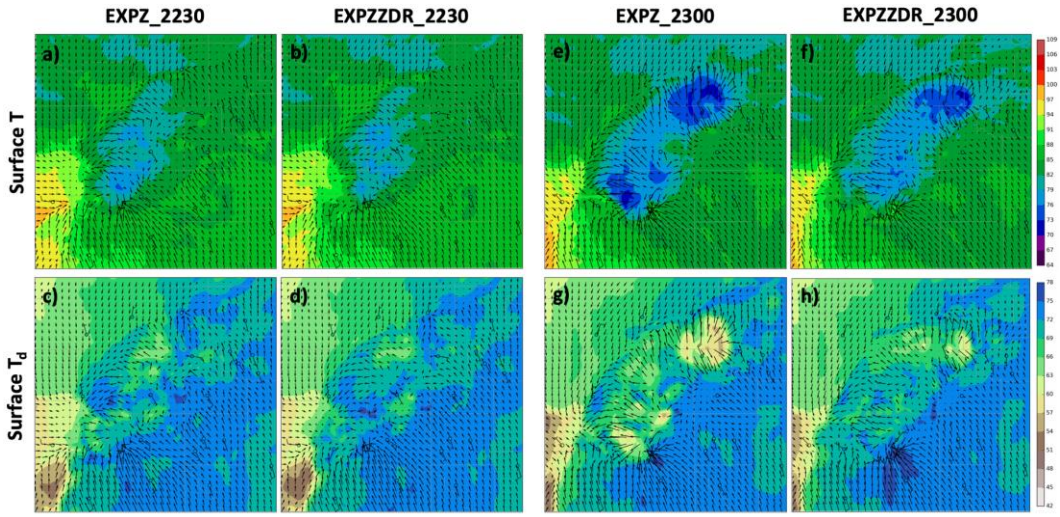

Fig. 2.1.13. Analyzed surface temperature (T, ° C) at 2230 UTC for (a) EXPZ_2230 and (b) EXPZZDR_2230 and (c) – (d) surface dewpoint (T_d, ° C) as well as for (e) – (h) EXPZ_2300 and EXPZZDR_2300. Strengthening analyzed surface winds are indicated by lengthening arrows. Observed surface temperature and wind barbs (m h^{-1}) from the Oklahoma Mesonet are included in the overlaid circles.

Summary and Future Work

In this study, differential reflectivity (Z_{DR}) observations are assimilated using the ensemble Kalman filter (EnKF) for the 31 May 2013 Oklahoma storm event in addition to reflectivity (Z). Attention is paid to two storms in central/northern Oklahoma: the famous El Reno storm and a storm to the north that produced severe wind and hail in the vicinity of Stillwater, OK. Two sets of experiments initialize forecasts after a different number of data assimilation (DA) cycles to assess whether the assimilation of Z_{DR} can lead to improved forecasts over fewer DA cycles. Evaluation of probability matched ensemble mean Z and probabilities of Z greater than 15 dBZ assess the evolution and precipitation coverage of the forecast storms. The El Reno storm in EXPZZDR better follows the evolution and track of the observed storm in the forecast initialized at 2230 UTC. However, the differences in the El Reno storm between EXPZ and EXPZZDR decrease at the later forecast times and show a similar bias in predicting a secondary storm that is too strong. On the other hand, the EXPZZDR forecasts show continued improvement of the Stillwater storm for forecasts launched at later times. Evaluation of probability swaths of derived forecast products for updraft helicity and hail size show similar results. There is a greater improvement in the EXPZZDR tracks for the El Reno storm at the earliest forecast launch time (2230 UTC) while the improvement increases during the later forecast times for the Stillwater storm.

These studies provide insight on what improvements may be achieved by additional dual-pol observations and what are the optimal configurations for dual-pol DA that can maximize the benefit of them for the future rapid-scan polarimetric phased array observations. The assimilation of Z_{DR} during storm initiation indicated an improvement in updraft strength and a future study will look deeper into the correlation between the observations and microphysical and dynamical state variables to better determine how and where these observations have the greatest impact. Also, assimilation of the retrieved updraft from Z_{DR} may facilitate updrafts more quickly during DA by directly inserting the updraft information.

Journal publications:

1. Stratman, D. R., N. Yussouf, Y. Jung, T. A. Supinie, M. Xue, P. S. Skinner, and B. J. Putnam, 2019: Optimal Temporal Frequency of NSSL Phased-Array Radar Observations for an Experimental Warn-on-Forecast System. *Wea. Forecasting*, in press. https://doi.org/10.1175/WAF-D-19-0165.1
2. Supinie, T. A., Y. Jung, N. Yussouf, D. Stratman, B. Putnam, and M. Xue, 2020: Impact of High-Temporal Phased Array Observation on the Prediction of the 31 May 2013 Tornadic and Flash Flood event, *Wea, Forecasting*, To be submitted.
3. Putnam, B., Y. Jung, N. Yussouf, T. Supinie, D. Stratman, M. Xue, C. Kuster, and J. Labriola, 2010: The Impact of Assimilating Z_{DR} Observations on Storm-Scale Ensemble Forecasts of the 31 May 2013 Oklahoma Storm Event, *Wea, Forecasting*, To be submitted.

Conference Presentations:

a. Yussouf, N, Y. Jung, T. Supinie, D. Stratman, and B. Putnam, 2018: Next-generation Rapid-Scan Phased Array Radar Observations on Storm-scale NWP for Hazardous Weather Forecasts, *29th Weather Analysis and Forecasting/25th Numerical Weather Prediction Conference*, Denver, CO, USA, Amer. Meteor. Soc.

b. Stratman, D, N. Yussouf, Y. Jung, T. Supinie, and B. Putnam, 2018:Optimal Temporal Frequency of the Next Generation Phased Array Radar Observations for Storm-Scale Data Assimilation, *29th Conference on SLS*, Stowe, Vermont, , Amer. Meteor. Soc.

c. Putnam, B. J., Y. Jung, N. Yussouf, D. R. Stratman, T. A. Supinie, and M. Xue, 2018: Development of a GSI-based system with polarimetric radar data assimilation capabilities for storm-scale ensemble forecasts, *29th Conference on Severe Local Storms*, Stowe, Stowe, Vermont, Amer. Meteor. Soc.

d. Supinie, Timothy A., Youngun Jung, Nusrat Yussouf, and Ming Xue, 2018: Improvement of NOAA's Warn on Forecast Capabilities through Phased Array Radar Data Assimilation with the 4-Dimensional Ensemble Kalman Filter. Poster presentation at the 29th Conference on Severe Local Storms, Stowe, VT.

e. Yussouf, N, Y. Jung, T. Supinie, D. Stratman, and B. Putnam, 2019: Impact of Phased-Array Radar on Storm-Scale NWP Modeling for Severe Weather Prediction, *Phased Array Radar Symposium, 99th AMS Annual Meeting*, Phoenix, AZ, USA, Amer. Meteor. Soc.

References:

Kuster, C.M., P.L. Heinselman, J.C. Snyder, K.A. Wilson, D.A. Speheger, and J.E. Hocker, 2017: An Evaluation of Radar-Based Tornado Track Estimation Products by Oklahoma Public Safety Officials. Wea. Forecasting, **32**, 1711–1726, https://doi.org/10.1175/WAF-D-17-0031.1

Kuster, C.M., J.C. Snyder, T.J. Schuur, T.T. Lindley, P.L. Heinselman, J.C. Furtado, J.W. Brogden, and R. Toomey, 2019: Rapid-Update Radar Observations of ZDR Column Depth and Its Use in the Warning Decision Process. Wea. Forecasting, **34**, 1173–1188, https://doi.org/10.1175/WAF-D-19-0024.1

Park, H.S., A.V. Ryzhkov, D.S. Zrnić, and K. Kim, 2009: The Hydrometeor Classification Algorithm for the Polarimetric WSR-88D: Description and Application to an MCS. Wea. Forecasting, **24**, 730–748, https://doi.org/10.1175/2008WAF2222205.1

Supinie, T. A., N. Yussouf, Y. Jung, M. Xue, J. Cheng, and S. Wang, 2017: Comparison of the Analyses and Forecasts of a Tornadic Supercell Storm from Assimilating Phased-Array Radar and WSR-88D Observations. *Weather Forecast.*, **32**, 1379–1401, https://doi.org/10.1175/WAF-D-16-0159.1.

Thompson, G., S. Tessendorf, A. Heymsfield, and I. Kyoko, 2018: Improving graupel and hail treatment in the thompson microphysics parameterization. North American Hail Workshop, Boulder, CO, NCAR.

Wang, Y., Y. Jung, T. A. Supinie, and M. Xue, 2013: A hybrid MPI-OpenMP parallel algorithm and performance analysis for an ensemble square root filter designed for multiscale observations. *J. Atmos. Ocean Tech.*, **30**, 1382-1397. doi: 10.1175/JTECH-D-12-00165.1.

Whitaker, J. S., and T. M. Hamill, 2012: Evaluating Methods to Account for System Errors in Ensemble Data Assimilation. *Mon. Weather Rev.*, **140**, 3078–3089, https://doi.org/10.1175/MWR-D-11-00276.1.

Xue, M., M. Tong, and K. K. Droegemeier, 2006: An OSSE framework based on the ensemble square-root Kalman filter for evaluating impact of data from radar networks on thunderstorm analysis and forecast. *J. Atmos. Oceanic Technol.*, **23**, 46–66, doi: 10.1175/JTECH1835.1.

Zhang, F., C. Snyder, and J. Sun, 2004: Impacts of initial estimate and observation availability on convective-scale data assimilation with an ensemble Kalman filter. *Mon. Wea. Rev.*, **132**, 1238–1253, doi: 10.1175/1520-0493(2004)132<1238:IOIEAO>2.0.CO;2.

2.2 Targeted Observation Methods for Phased Array Radar[2]

Ensemble-based targeted observation method implemented to radar radial velocity observations

The potential future installation of a meteorological phased-array radar network will provide capabilities for case-specific adaptive scanning. Knowing the impacts adaptive scanning may have on short-term forecasts will influence scanning strategy decision-making in hopes to produce the most optimal ensemble forecast while also benefiting human severe weather warning decision-making. An ensemble-based targeted observation algorithm is applied to an Observing System Simulation Experiment (OSSE) where the impacts of synthetic idealized supercell radial velocity observations are estimated before the observations are "collected" and assimilated. The forecast metric of interest is the low-level rotation forecast metric (0-1 km updraft helicity), a surrogate for tornado prediction. It is found that the ensemble-based targeted observation approach can reasonably estimate the true error variance reduction when an effective method that treats sampling error is applied, the period of model forecast is associated with less degrees of nonlinearity, and the observation information content relative to the background forecast is larger. In some scenarios, a subset of a full-volume scan assimilation produces better forecasts than all observations within the full-volume. Assimilating the full-volume scan increases the number of potential spurious correlations arising between the forecast metric and radial velocity observation induced state perturbations which may degrade the forecast metric accuracy. Details are provided in Kerr and Wang (2019), a manuscript accepted for publication.

Impact of assimilating clear-air radial velocity observations from phased array radar on the forecasting of supercell thunderstorm

Phased-array radar (PAR) technology offers the flexibility of sampling the storm and clear-air regions with different update times. As such, the radial velocity from clear-air regions, typically with lower signal-to-noise ratio, can be measured more accurately. Zrnic et al. (2019), for example, indicate that an operational meteorological PAR could plausibly detect Bragg-scattered echoes to an altitude of 7 km AGL

In this study, observing system simulation experiments (OSSEs) were conducted to explore the potential value of assimilating the clear-air radial velocity observations to improve numerical prediction of supercell thunderstorms. Synthetic PAR observations of a splitting supercell were assimilated at different stages of the storm using an ensemble Kalman filter. Results show that assimilating environmental clear-air radial velocity can reduce wind errors in the near-storm environment and within the storm region, and improve the supercell forecasts at different stages. This is especially the case for the forecast after 30 min. After assimilating clear-air radial

[2] Principal Investigator: Xuguang Wang (OU SoM)

velocity observations, the probabilities of updraft helicity and precipitation within the corresponding swaths of the truth simulation increase up to 30–40%. Additional diagnostics suggest that more accurate track forecast, stronger vertical motion, and better-maintained supercell structure can be attributed to better analyzed and predicted linear and nonlinear dynamic forces. Consequently, assimilating clear-air radial velocity improves the accuracy and duration of storm structure (rotating updrafts), produces more reasonable updraft size, more accurate storm track, and improves the surface accumulated precipitation forecast. The performance of the forecast with more frequent assimilation (1 versus 5 minutes) of the clear air radial velocity does not show systematic improvement. These results highlight the potential for assimilating the clear-air radial velocity observations to improve the numerical prediction of supercell thunderstorms. A manuscript (Huang, Wang et al., 2019) documenting the study has been submitted and is in review.

Impact of using inhomogeneous errors of radar data on the prediction of a supercell and its initiation

We collaborated with researchers at OU's Advanced Radar Research Center (ARRC) to estimate SNR-dependent inhomogeneous errors in the radial velocity field, and generate simulated radar observation data using these inhomogeneous errors. An OSSE was performed to investigate the impact of inhomogenous V_R errors on supercell forecasting and on the initiation of the supercell.

Future Plans

We plan to conduct ongoing research and development on the benefits of assimilating PAR observations at very high temporal (30-60 sec) and spatial resolution (50-500m) using the dual resolution hybrid ensemble-variational data assimilation system (Wang and Wang 2019). This will support further exploration of the potential impact of PAR on convective scale weather prediction.

References:

Kerr, C. and X. Wang, 2019: Ensemble based targeted observation method applied to radar radial velocity observations on idealized supercell low-level rotation forecasts: a proof of concept. Mon. Wea. Rev., in press.

Huang, Y., X. Wang, C. Kerr, A. Mahre, T. Yu and D. Bodine, 2019: Impact of assimilating clear-air radial velocity observations from phased array radar on the forecasting of supercell thunderstorm: An observing system simulation experiment study. Mon. Wea. Rev., accepted with revision.

Wang, Y., and X. Wang, 2019: Prediction of tornado-like vortex (TLV) embedded in the 8 May 2003 Oklahoma City tornadic supercell initialized from the sub-kilometer analysis produced by

the dual resolution GSI based EnVar data assimilation system. *Mon. Wea. Rev.*, accepted with revision.

Zrnic, D.S., S. Koch, R. Palmer, M. Weber, K. Hondl, G. McFarquhar, and M. Jain, 2019: How an agile-beam polarimetric phased array radar can add to the observing capabilities of the NWS: winds and humidity measurements in optically clear air. AMS 35th Conference on Environmental Information Processing Technologies, Tucson, AZ

Invited Talks that Include SENSR Funded Results:

Keynote talk at the 6th International Symposium on Data Assimilation, Munich, Germany, 2018, "Research and Development of GSI-based EnVar for Convective Scale Radar Data Assimilation: Challenge and Progress"

Texas A&M Department of Atmospheric Sciences invited colloquium, College Station, TX, 2018, "Research and Development of GSI-based Ensemble-Variational (EnVar) Data Assimilation for Convective Scale Severe Weather and Hurricane Prediction"

Conference presentations:

Kerr, C., X. Wang, 2017: Multi-function phased array radar observation targeting of a convective storm. International symposium on earth science challenge, Tokyo, Japan

Kerr, C. and X. Wang, 2018: Impacts of Targeted PAR Radial Velocity Observations on Idealized Supercell Low-Level Rotation Forecasts. 29th Conference on Severe Local Storms. Stowe, VT.

Huang, Y., X. Wang, C. Kerr, A. Mahre, T. Yu, and D. Bodine, 2020: Impact of Assimilating Clear-Air Radial Velocity Observations on the Forecasting of Supercell Thunderstorm: An Observing System Simulation Experiment Study. AMS annual meeting, Boston.

2.3 Rapid-Scan Studies using NSSL's Experimental WSR-88D (KOUN)[3]

In order to assess the potential impact of dual-polarization phased-array radar observations on the warning decision process, SENSR funding was used to collect data with the dual-polarization KOUN WSR-88D radar using rapid-update sector scans. These provided 1-2 minute updates that could be used as a proxy for phased array radar data. These data, along with previously collected KOUN datasets, were then used to investigate meteorological (severe weather warning) and hydrologic (flash flood warning) advantages provided by rapid-update radar data. For the meteorological studies, work focused on first understanding the operational applications of polarimetric variables followed by an assessment of how the collection of *rapid-update* observations might further benefit the warning decision process. A review of these studies, along with a summary of KOUN data collection that was supported by SENSR funding, is provided in the following section.

Meteorological Studies

Rapid-update radar observations of Z_{DR} column depth and its use during the warning decision process

National Weather Service forecasters consider various information sources and scientific conceptual models during the waring decision process (e.g., Andra et al. 2002). The dual-polarization upgrade to the Weather Service Radar 1988-Doppler (WSR-88D) radar network provides additional information about a storm's structure and hydrometeor composition, but these new data are not yet commonly integrated into severe weather warning decisions. The purpose of this study is to examine one potentially important dual-polarization radar signature known as a Z_{DR} column (e.g., Ryzhkov et al. 1994; Snyder et al. 2015). Z_{DR} columns can be a good indicator of updraft location and intensity and therefore potential severe weather (e.g., Kumjian 2013). The ultimate goal is to integrate Z_{DR} columns into existing scientific conceptual models that forecasters use while making warning decisions by comparing Z_{DR} column evolution to commonly used radar signatures, such as -20° C reflectivity cores and mesocyclones, and observed storm reports. Radar update time is also assessed to determine if rapid-update volumetric radar data is valuable for effectively observing and using Z_{DR} columns.

To accomplish these research goals, the Z_{DR} column depth algorithm (Snyder et al. 2015) was run on 13 rapid-update data cases collected using a research WSR-88D located in Norman, OK (KOUN). KOUN collected 90° sector scans with a volumetric update time of 2.1 min or less, and therefore can be used as a proxy for a future dual-polarization phased array radar. The analysis reveals that both Z_{DR} columns and -20° C reflectivity cores are good indicators of storm intensity and local maxima in these signatures occur prior to severe wind and hail reports. Z_{DR} columns may be especially helpful to forecasters because they evolve about 3.5–9.0 min earlier than -20° C reflectivity cores. This extra time could give a forecaster more time to anticipate

[3] Principal Investigators: Terry Schuur, Berry Wen and Charles Kuster (CIMMS)

storm evolution and potential threats and therefore allow for an increase in lead time for severe thunderstorm warnings.

Since Z_{DR} columns could be useful to forecasters issuing severe thunderstorm warnings, it is noteworthy that rapid-update KOUN data (~2-min updates) appear to provide more complete information and longer lead time than KOUN data that was degraded to represent traditional update time of the WSR-88D network (~5-min updates). For all severe hail reports considered (*n* = 21), median lead time (i.e., time between severe weather report and radar signature local maxima) of Z_{DR} column size and median depth was 4.0 and 5.3 min greater for rapid-update data when compared to traditional-update data, respectively (Fig. 2.3.1a). A similar pattern was found for severe wind reports (*n* = 11), where median lead time was 7.5 and 7.0 min greater for rapid-update data when compared to traditional update data (Fig. 2.3.1b). This additional time could allow forecasters to push life-saving information out to the public a few minutes earlier.

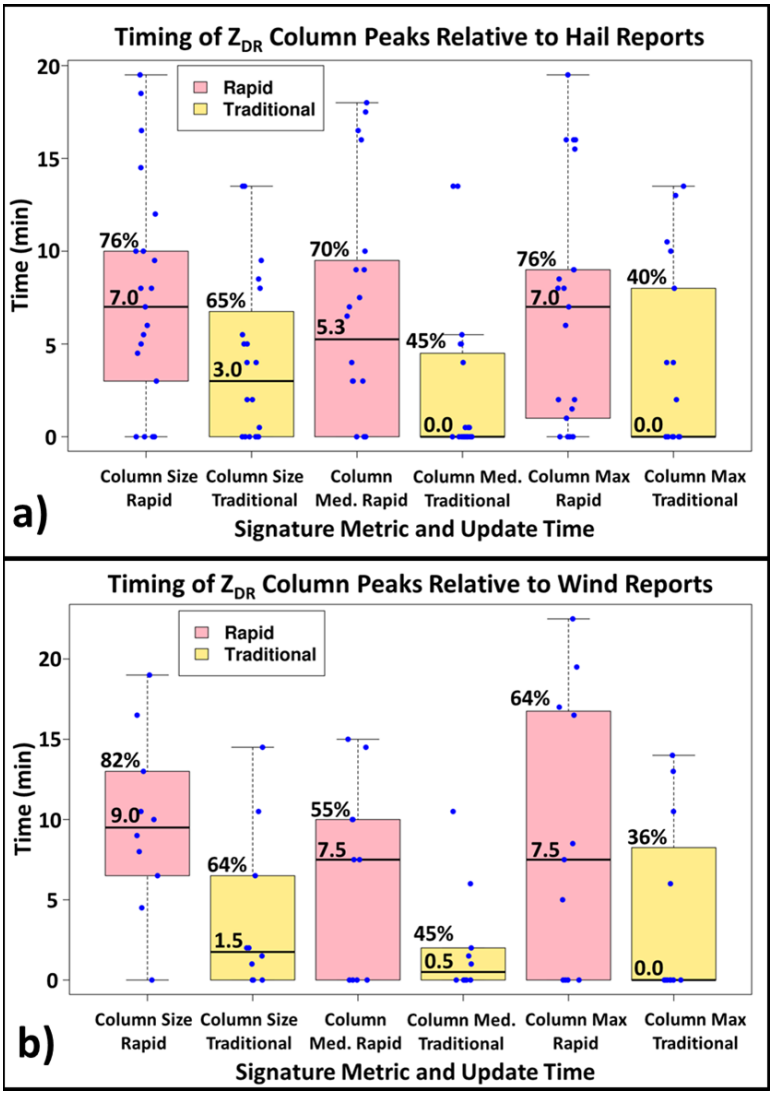

*Figure 2.3.1. Box plots showing amount of time signature local maxima (i.e., peaks) occurred prior to a) severe hail reports and b) severe wind reports for rapid-update (< 2 min updates) KOUN data (pink) and traditional-update (5–6 min updates) KOUN data (yellow). Percent of reports preceded by a signature peak and median lead times are annotated above and within each box respectively. Box edges are the lower (Q1) and upper (Q3) quartiles, the horizontal black line is the median, and the lower and upper whiskers represent Q1-1.5*IQR and Q3+1.5*IQR respectively, where IQR is the interquartile range. Blue dots indicate data used in box plot creation.*

Rapid-update radar data and downburst precursor signatures observed in K_{DP}

Downbursts pose a challenge to forecasters because they develop quickly and can be hard to detect. For this reason, research efforts have sought to identify radar precursor signatures that can alert forecasters to impending downburst development (e.g., Isaminger 1988; Roberts and Wilson 1989). The dual-polarization upgrade of the WSR-88D radar network provides new radar variables and therefore potentially new downburst precursor signatures to forecasters. Therefore, the purpose of this study is to examine one such new signature, known as a K_{DP} core, to determine if it may provide reliable information about impending downburst development and intensity to forecasters. K_{DP} cores may be useful because they can indicate areas of melting graupel and hail in addition to areas with increased raindrop concentration and therefore higher potential for water loading and evaporation if the rain falls through an unsaturated layer below cloud base. Observing processes such as melting, water loading, and evaporation is important because all three can increase the intensity of a downdraft and the subsequent intensity of the downburst it ultimately produces.

Size, magnitude, and vertical gradient of K_{DP} was examined for 11 cases containing 49 different downbursts across primarily the Southeast and central Great Plains. Of these, 3 cases and 15 downbursts had rapid-update KOUN data available. Analysis showed that K_{DP} cores developed and intensified prior to a majority of downbursts in this dataset, but the distributions of K_{DP} core size, magnitude, and vertical gradient were relatively similar between strong and weak downbursts. Therefore, K_{DP} cores may provide a reliable signal to forecasters that a downburst is about to develop, but it may not provide much information about how strong the impending downburst might be.

However, it is possible that rapid-update radar data may be needed to observe the important details of signature evolution needed to anticipate downburst intensity. When looking only at rapid-update (~2-min updates) KOUN data, the distributions of 2 km K_{DP} vertical gradient between strong and weak downbursts are statistically significantly different (Fig.2.3.2a). These differences are much smaller when only looking at traditional-update (~5–6 min updates) WSR-88D data (Fig. 2.1.2b). It is possible that rapid-update radar data are needed to use K_{DP} cores to predict the relative intensity of an impending downburst. Further work is ongoing with additional cases to explore this possibility.

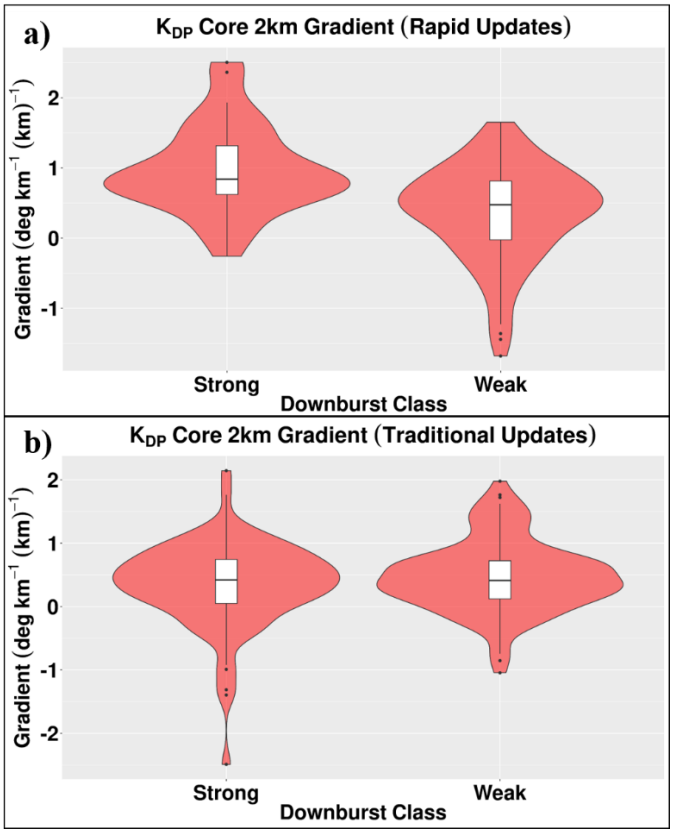

Figure 2.3.2. Violin plots showing the vertical gradient of maximum values within the K_{DP} core over 2 km for a) rapid-update (~2 min) KOUN data, and b) traditional update (~5–6 min) WSR-88D data. Strong downbursts had a maximum radial velocity of 22.5 m s^{-1} or higher, while weak downbursts had a maximum radial velocity of less than 22.5 m s^{-1}. The red area of the plot shows the probability density with a greater width indicating a higher frequency of occurrence. Associated box plots are included within each violin plot for reference. Box edges are the lower (Q1) and upper (Q3) quartiles, the horizontal black line is the median, and outliers are indicated by black dots.

Rapid-update radar data and downburst precursor signatures for hail producing storms

Rapid-update KOUN datasets were examined to evaluate potential operational benefits provided by rapid-update data in hail producing storms. In particular, five parameters that have been previously identified as precursor signature to hail formation, such as Maximum Expected Size of Hail (MESH), Storm Top Divergence (SDTD), Mid-altitude Rotational Velocity (MRV), Vertically Integrated Liquid, and Maximum reflectivity at the -20°C level height (Z_{253K}), were computed at both 1- and 5-minute intervals. Time series of each variable were then evaluated to identify whether rapid-update data were better able to identify trends that would indicate whether or not a storm might soon produce hail and/or become severe. Based on this work, cyclical maximums in Z_{DR} column size were found to sometimes occur prior to cyclical maximums in upper-level reflectivity core magnitude and MESH. The shorter volume update times from KOUN therefore provided a better representation of the rapid changes in storm intensity seen for the two hailstorms. In an examination of giant hail observations from the 31 May 2013 El Reno,

OK supercell – a storm for which data from the old SPY-1 PAR antenna were also available – there were several instances of large increases and/or decreases in MESH and STD values over time intervals that were much shorter (~2 min) than the typical update times of WSR-88D VCPs (4.5-6.5 minutes).

Hydrologic studies

Investigations into the impact of high spatio-temporal resolution data for flash flood warnings

Quantitative precipitation estimates (QPE) at high spatiotemporal resolution are essential for flash flood forecasting, especially in urban environments and headwater areas. An accurate quantification of precipitation is directly related to the temporal and spatial sampling of the precipitation system. Phased array radar (PAR) technology presents an opportunity to provide updates that are at least 4-5 times faster than the conventional WSR-88D scanning rate. As part of this project, we collected data with the KOUN WSR-88D research using rapid-update (~1 minute volume) scanning strategies that provided datasets that serve as a proxy for those collected by future phased array radars.

Two scanning strategies were adopted to observe the flash flood events that are presented in this study. The first included four elevation angles (0.5°, 1.0°, 1.6°, and 2.4°) that were sampled over a 90° sector with a volume update time of ~ 37s–38s. This strategy was used to collect rapid-update observations from 0353 to 1308 UTC of the 29 April 2017 central OK flash flood event (Fig. 2.3.3a). The second included two elevation angles (0.5° and 1.0°) that were collected over a full 360° azimuth with a volume update time of ~ 1 min. This strategy was used to collect rapid-update observations from 2037 to 0900 UTC of the 14-15 central OK flash flood event (Fig. 2.3.3b). The 0.5° elevation angle for this event was used to estimate rainfall rates at the surface and the 1.0° elevation angle was used to identify and filter out any ground clutter. Both scanning strategies employ data oversampling to achieve 0.5° azimuthal spacing, known as "super resolution" (Brown et al. 2002). Since the update times of both events are less than or around 1 min, we fixed the KOUN data on every 1-min interval by selecting the KOUN measurements at the closest time. Surface rainfall rates were calculated from KOUN surface measurements (elevation angle of 0.5°) using $R = 0.017\ Z^{0.714}$ for convective rain and hail, and $R = \max(0.0365Z^{0.625}, 0.1155Z^{0.5})$ for stratiform rain, the same R-Z relationships adopted in MRMS system. The precipitation fields from KOUN were then interpolated linearly from a spherical (azimuth, and range) to Cartesian coordinate system with a 1 km resolution centered at the KOUN radar.

(a)

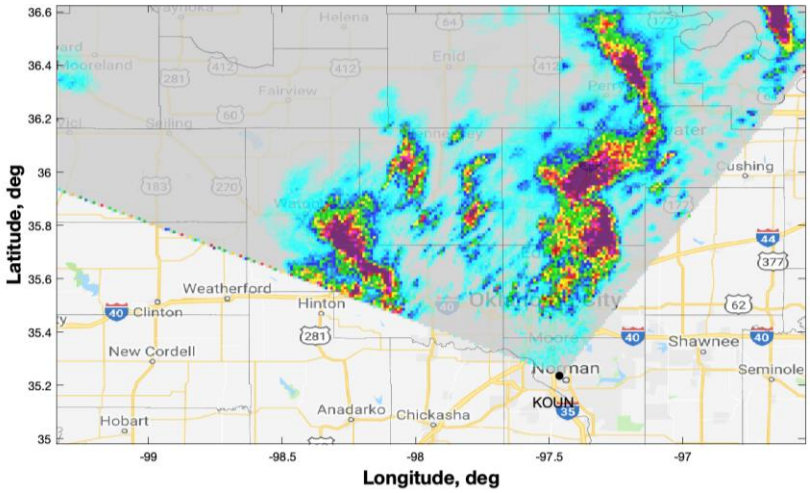

(b)

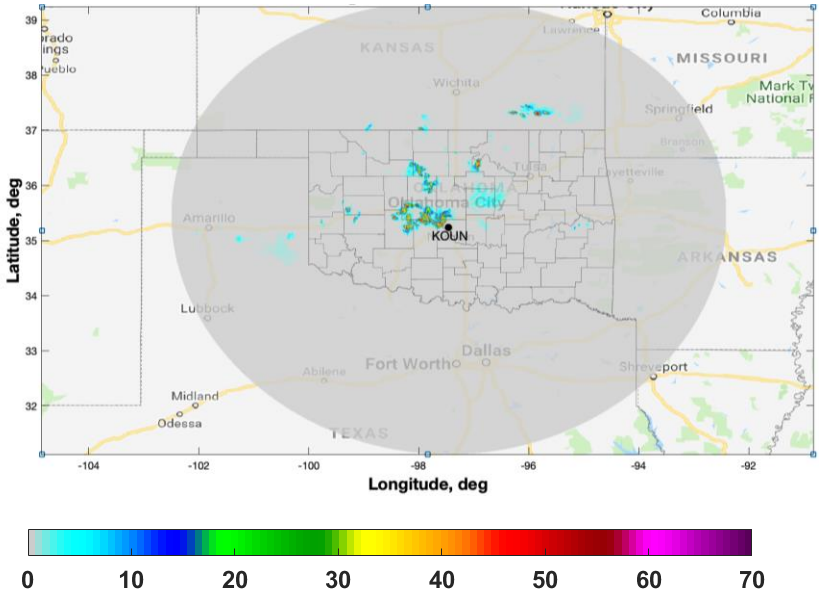

Figure 2.3.3. KOUN rapid-scan VCPs, (a) data are collected over an 90° sector with 0.5° azimuthal spacing and 250-m range resolution, with 4 elevation angles (0.5°, 1.0°, 1.6°, and 2.4°) on 29 April 2017; (b) data are collected over 360° with 0.5° azimuthal spacing and 250-m range resolution, with two elevation angels (0.5°, 1.0°) on 14 Aug. 2018.

To focus on the examination of uncertainties from rainfall's high variability instead of uncertainties from instrument measurements and retrieval algorithms, the high resolution KOUN rainfall estimates were resampled into three other spatial and temporal resolutions: 1) 1-km/5-min rainfall representing the WSR-88D radar observations, 2) 10-km/30-min rainfall

representing NASA GPM/IMERG products (Huffman and Bolvin, 2015), and 3) 1-km/60-min rainfall to focus on the hydrologic effect of hourly temporal resolution that commonly used by the hydrology community. KOUN 1-km/1-min QPE product and three other simulated QPE products were then used to force the Ensemble Framework for Flash Flood Forecasting (EF5) hydrologic model.

Figure 2.3.4 shows the time series of rainfall rates and simulated discharges at the Cottonwood Creek stream gauge near Seward, OK (USGS hydrologic unit 07159750) on 29 April 2017. As can be seen in Fig. 2.3.4b, the peak rain rate decreases as the temporal resolution gets coarser. It can also be seen that the precipitation bias resulting from poor spatial and temporal sampling propagates in the streamflow simulations. Fig. 2.3.4c shows that the discharge generated by rapid-update KOUN data better matches stream gauge observations than those generated by the precipitation products with coarser resolution. Note that all simulations underestimate discharge compared to the stream gauge observations. In this paper, we only consider the effects of precipitation sampling error on the flash flood forecasts. Therefore, we took simulated discharge forced by KOUN as truth to assess other simulations, rather than discussing the underestimation of all the simulations compared to the stream gauge observations. Compared to peak discharge from KOUN at the stream gauge location, the peak discharge from WSR-88D, IMERG and HourlyQPE is reduced by ~10%, 33% and 43%, respectively.

(a)

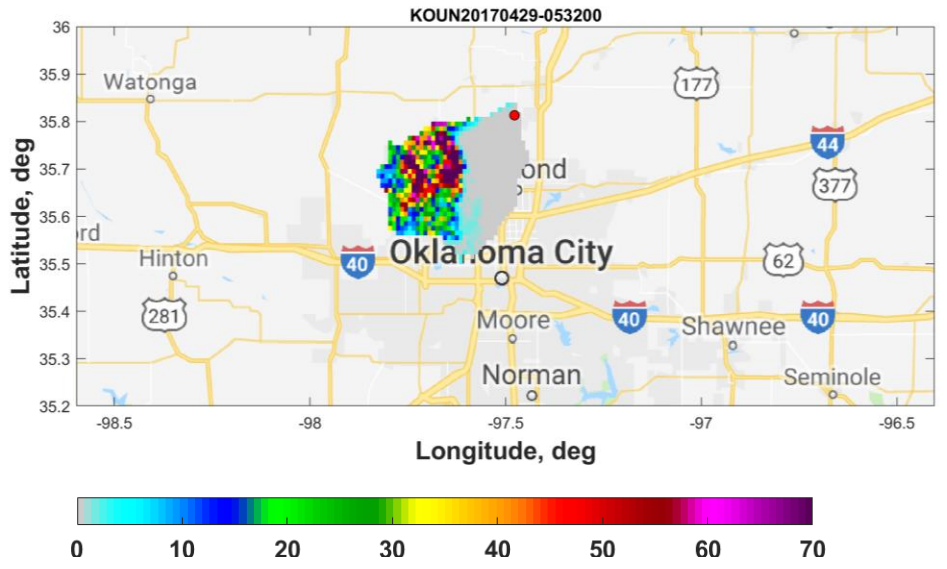

(b)

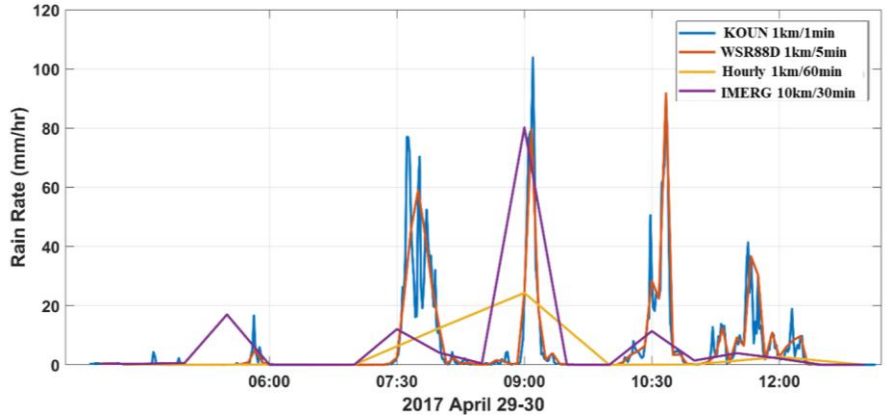

(c)

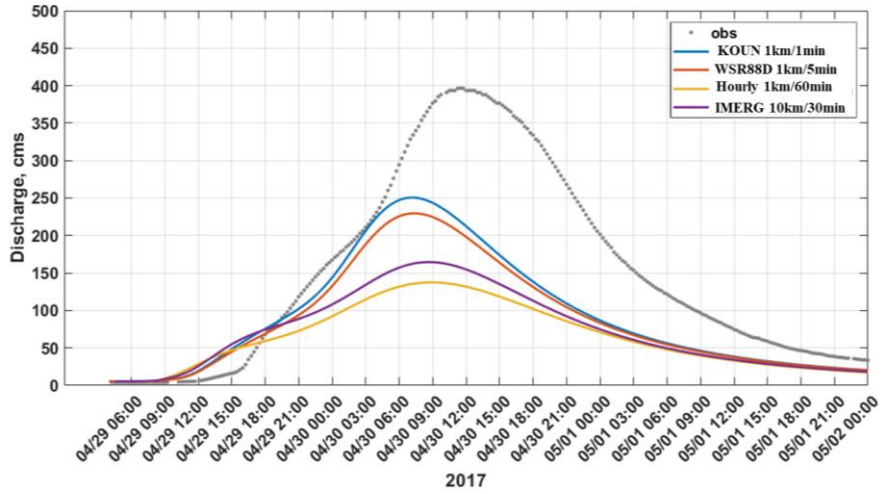

Figure 2.3.4. (a) Example of instantaneous rainfall rate measured by KOUN at 05:32 UTC on 29 April, 2017. (b) The time series data of different precipitation data at different temporal-spatial resolutions. (c) The time series data of simulated stream flow simulated from different precipitation data. In (c), the dotted gray line is observation from a USGS stream gauge (Cottonwood Creek near Seward, USGS hydrologic unit 07159750). The location of the time series data is from the stream gauge noted by the red dot in (a).

Fig. 2.3.5 presents the EF5 peak unit discharge product forced by KOUN observations for the two cases. On 29 April 2017, peak unit discharges exceed 3 $m^3s^{-1}km^{-2}$ in the southeastern part of the basin (Fig. 2.3.5a), which is consistent with NWSChat reports. It's interesting to point out that the heaviest precipitation occurred in the northwestern part of the basin (Fig. 2.3.5a), not in the southeastern part where the most severe flooding impacts were reported. Due to the increase in impervious surfaces in the Oklahoma City metropolitan area, the EF5 model has very low or

no infiltration in some areas, resulting in high values of runoff. The location mismatch of heaviest precipitation and flash flood occurrence indicate that the precipitation errors do not propagate linearly in the flash flood simulation. Basin physiographic and morphological characteristics, such as basin slope, drainage ratio, basin magnitude, infiltration rates, ruggedness number, etc, will influence the effects of precipitation sampling errors on flash flood forecasts. The peak unit discharge for 14 August 2018 is displayed in Fig. 2.3.5b. The peak unit discharge exceeds 6 $m^3s^{-1}km^{-2}$ in southern Oklahoma City, corresponding closely with media reports.

(a) 29 April 2017

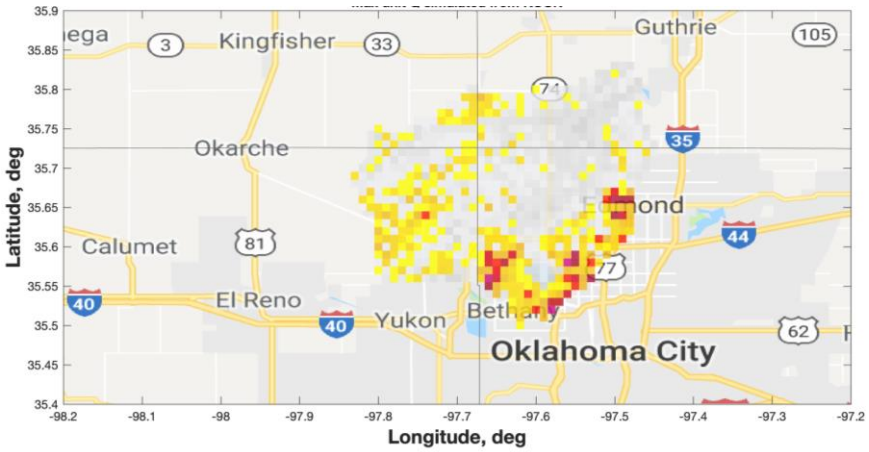

(b) 14 April 2018

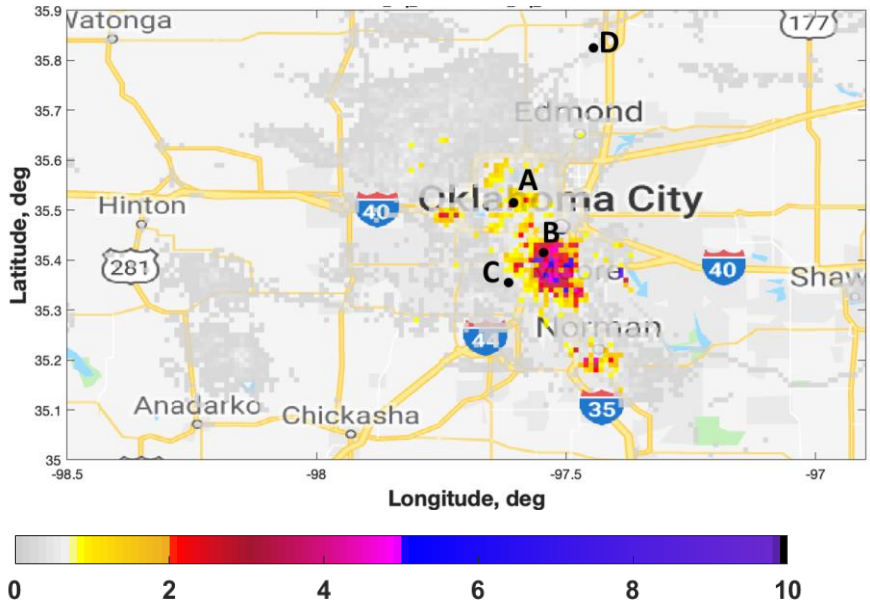

Maximum unit discharge, $(m^3s^{-1})km^{-2}$

Figure 2.3.5. Maximum unit discharge simulation using KOUN 1-min/1-km observations (a) from 0300 UTC 29 April 2017 to 0000 UTC 2 May 2017; (b) from 2100 UTC 14 August 2018 to 0000 UTC 17 August 2018.

The magnitude of peak unit discharges simulated from coarse resolution precipitation products are also assessed by comparing them to the KOUN simulations (Fig. 2.3.6). WSR-88D simulations (Fig. 2.3.6a) show a consistent negative bias over the study area for both events, while IMERG (Fig. 2.3.4b) and HourlyQPE (Fig.2.3.6c) simulations have both positive and negative biases when compared to KOUN simulations. In particular, it is easy to notice that the spatial patterns of the bias for IMERG-based simulations (Fig. 2.3.6b) depict the 10 km grid pixel. This is due to the higher spatial resolution of the hydrologic model's computational grid. The right column of Figs. 2.3.6b and c shows that the area of positive bias is adjacent to the area of negative bias, which indicates IMERG and HourlyQPE sampling frequency has difficulty capturing the movement of precipitation in fast-moving storms or isolated convective system.

(a) WSR-88D - KOUN

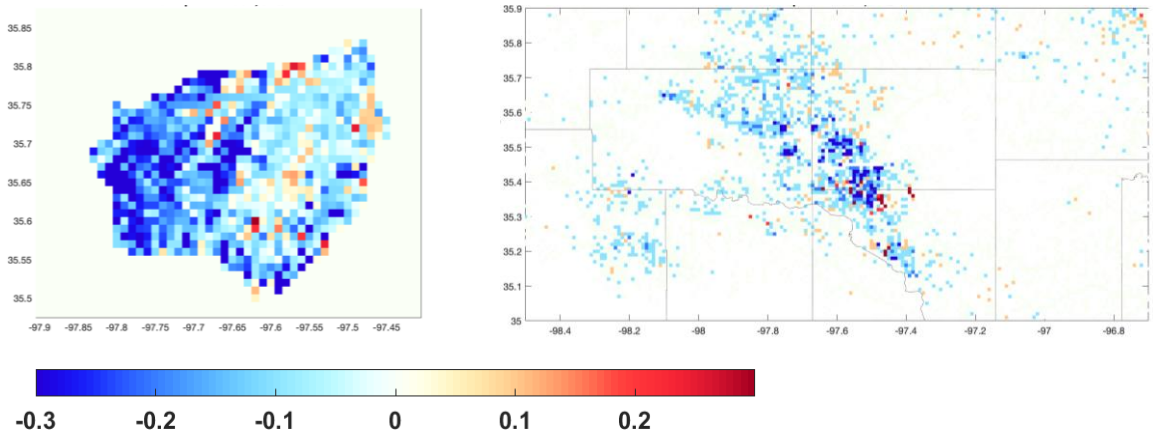

Bias of peak unit discharge, $(m^3s^{-1})km^{-2}$

(b) IMERG - KOUN

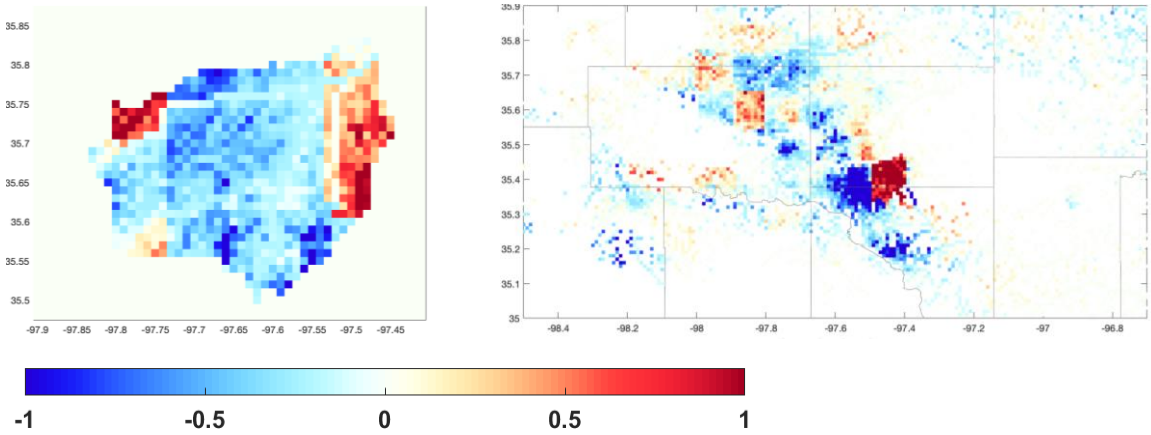

(c) HourlyQPE -KOUN

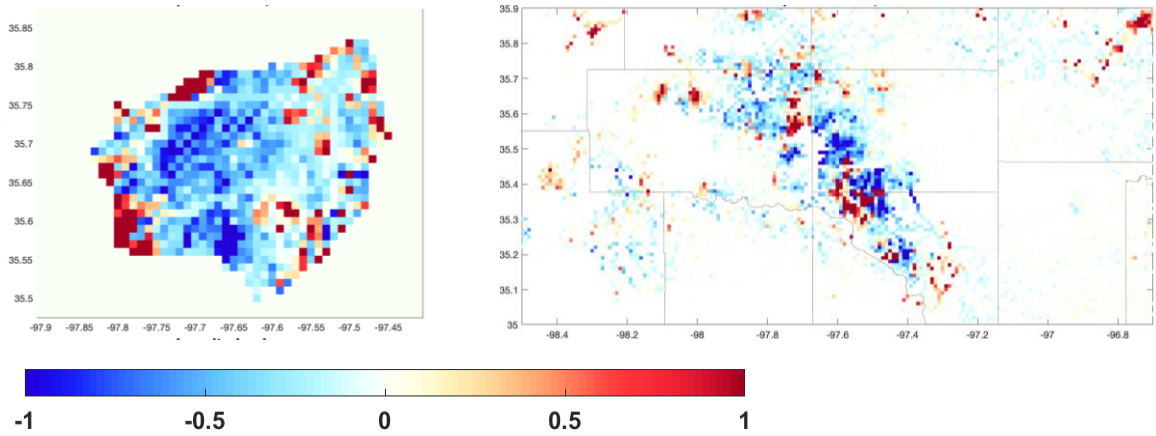

Figure 2.3.6. Bias of peak unit discharge forced by (a) WSR-88D, (b) IMERG, and (c) HourlyQPE, compared to the unit peak discharge simulated by KOUN for 29 April 2017 (left column) and 14 August 2018 (right column). Note that to demonstrate the small bias of (a) WSR-88D, the color bar ranges from -0.3 to 0.3 $m^3s^{-1}km^{-2}$, while color bars for other figures range from -1 to 1 $m^3s^{-1}km^{-2}$.

To estimate the negative impact on forecasting flash flood occurrence due to the degradation of resolution, simple metrics derived from contingency table statistics (i.e. POD, FAR, and CSI) are used. We assumed the unit discharge of 1.5 $m^3s^{-1}km^{-2}$ was the flash flood threshold and grid points with unit discharge of KOUN simulations greater than 1.5 are marked as flash flood grid points. Then we counted the number of the 'hits', 'misses' and 'false alarms' of other QPE-based simulations. Table 2.3.1 shows the POD, FAR and CSI for hydrological simulations forced by

the WSR-88D, IMERG, and HourlyQPE precipitation products. On 29 April 2017, WSR-88D data has a lower POD than HourlyQPE, but has a perfect FAR. Overall, WSR-88D data has the highest capacity to detect flash flood area compared to IMERG and HourlyQPE. However, both the CSI and POD of WSR-88D data for 29 April 2017 is only 0.38, indicating that WSR-88D data missed ~60% of the flash flooding grid points.

Table 2.3.1. The contingency table statistics benchmarked by KOUN simulations.

Event Date	QPE Products	POD	FAR	CSI
20170429	WSR-88D	0.38	**0**	**0.38**
	IMERG	**0.49**	0.75	0.20
	Hourly	0.16	0.86	0.08
20180814	WSR-88D	**0.88**	**0.01**	**0.97**
	IMERG	0.26	0.64	0.18
	Hourly	0.62	0.65	0.29

Nijssen and Lettenmaier (2004) studied the effect of error in accumulated precipitation at 0.5°×0.5° spatial resolution, due to periodic sampling (1 hr, 3 hrs and 6 hrs) of the precipitation rate, and found that streamflow errors were large for small drainage areas (5×10^3 km^2) and generally decrease for drainage areas up to 500 $\times10^3$ km^2. In this study, we also investigated the effect of precipitation sampling errors as a function of upstream drainage area but at the flash flood scale (i.e. drainages < 1000 km^2), where information with higher resolution is required. Examples of streamflow time series with different drainage areas are presented in Fig. 2.3.7, from a 1 km^2 drainage area to a river channel of 916 km^2. With drainage area increasing, the hydrographs change from narrow and sharp depicting flashy response typical of basin headwaters, to wide and smooth depicting slower response typical of main river stems. In addition, the differences between KOUN simulations and WSR-88D simulations diminish as drainage area increases. The behavior of the IMERG and HourlyQPE simulation time series at a single grid is not enough to explain the effects of sampling errors in precipitation, as 10 km spatial resolution or 60 min temporal resolution causes dramatic random error in precipitation product.

(a)

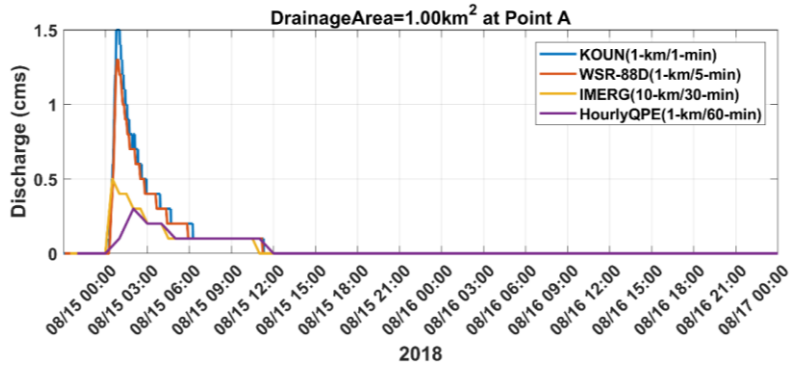
DrainageArea=1.00km^2 at Point A
KOUN(1-km/1-min)
WSR-88D(1-km/5-min)
IMERG(10-km/30-min)
HourlyQPE(1-km/60-min)
Discharge (cms)
1.5
1
0.5
0
08/15 00:00
08/15 03:00
08/15 06:00
08/15 09:00
08/15 12:00
08/15 15:00
08/15 18:00
08/15 21:00
08/16 00:00
08/16 03:00
08/16 06:00
08/16 09:00
08/16 12:00
08/16 15:00
08/16 18:00
08/16 21:00
08/17 00:00
2018

(b)

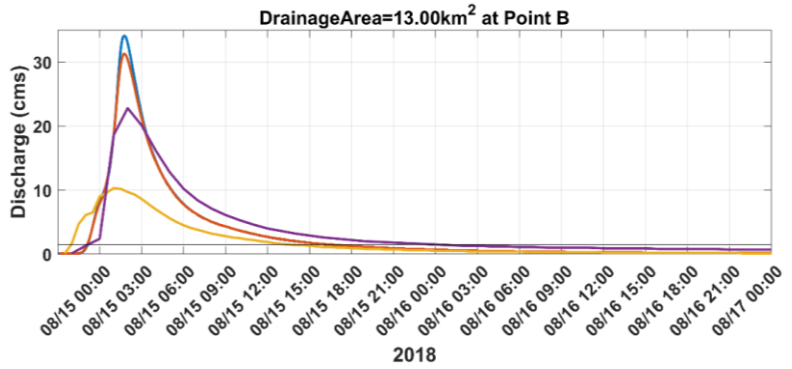
DrainageArea=13.00km^2 at Point B
Discharge (cms)
30
20
10
0
08/15 00:00
08/15 03:00
08/15 06:00
08/15 09:00
08/15 12:00
08/15 15:00
08/15 18:00
08/15 21:00
08/16 00:00
08/16 03:00
08/16 06:00
08/16 09:00
08/16 12:00
08/16 15:00
08/16 18:00
08/16 21:00
08/17 00:00
2018

(c)

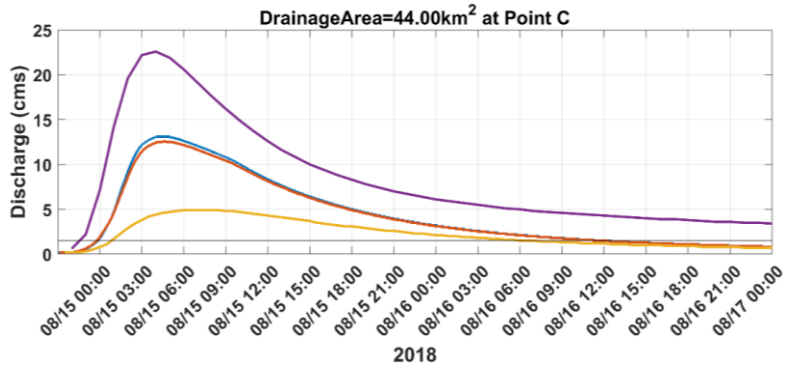
DrainageArea=44.00km^2 at Point C
Discharge (cms)
25
20
15
10
5
0
08/15 00:00
08/15 03:00
08/15 06:00
08/15 09:00
08/15 12:00
08/15 15:00
08/15 18:00
08/15 21:00
08/16 00:00
08/16 03:00
08/16 06:00
08/16 09:00
08/16 12:00
08/16 15:00
08/16 18:00
08/16 21:00
08/17 00:00
2018

(d)

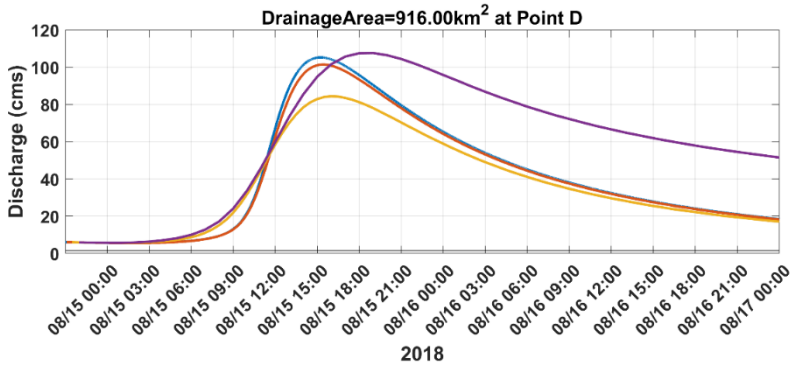

Figure 2.3.7. Time series of simulated discharge from different locations of different drainage areas. (a) From drainage area of 1 km^2 (Location A denoted as a black dot in Fig. 2.3.8b); (b) from drainage area of 13 km^2 (Point B in Fig. 2.3.8b); (c) from drainage area of 44 km^2 (Point C in Fig. 2.3.8b); and (d) from drainage area of 916 km^2 (Point D in Fig. 2.3.8b).

To summarize, this study demonstrates the quantification of precipitation errors resulting from degraded spatial and temporal sampling and their impacts on flash flood forecasts. The effect of precipitation sampling errors on flash flood forecasting was investigated using rapid-update KOUN precipitation observations at 10 km × 10 km resolution updating every ~1 minute to force the EF5 hydrological model. The simulated discharge from KOUN was then used as truth to assess simulations from three other precipitation products that had degraded spatial and/or temporal resolutions. The results show that QPE peak value decreases as the temporal resolution gets coarser and the effect of precipitation sampling error on flash flood forecasting is dependent on upstream drainage area. A future phased array radar network with the rapid-update scanning capabilities could benefit the hydrologic and meteorological communities by decreasing precipitation errors resulting from degraded spatial and temporal sampling, and therefore improve flash flood monitoring.

Investigations into hydrologic modeling improvements offered by polarimetric radar observations

In order to better assess the potential of dual-polarization phased-array observations to improve flash flood warnings, we must also develop a more complete understanding of how polarimetric radar observations – even when not collected in rapid-update mode – impact our ability to improve flash flood warnings. To address this, we collaborated with Dr. Jim Kurdzo of MIT/Lincoln Lab with the goal of comparing EF5 hydrologic simulations using three QPE products: 1) $R(Z) = 0.017\ Z^{0.714}$; 2) $R(Z,Z_{DR})=0.0142Z^{0.77}Z_{DR}^{-1.67}$; and 3) $R(A) = 4120A^{1.03}$. Fig. 2.3.8a shows the peak unit discharge simulated from EF5 using R(A) for the 31 May 2013 central Oklahoma flash flooding event. Fig. 2.3.8 b-d shows the time series of simulated discharges at three stream gauges denoted in Fig. 2.3.8a. The time series figures show that the discharge generated by R(A) matches best with stream gauge observations than those generated

by other two QPE retrieval algorithms. The preliminary results shows the hydrologic advantage brought by the R(A) algorithm. This project will be extended to include more cases.

(a)

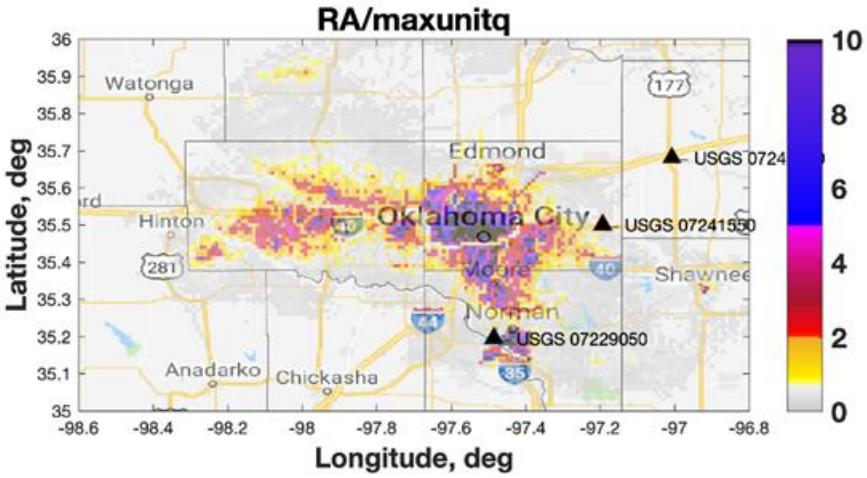

(b) USGS 07229050

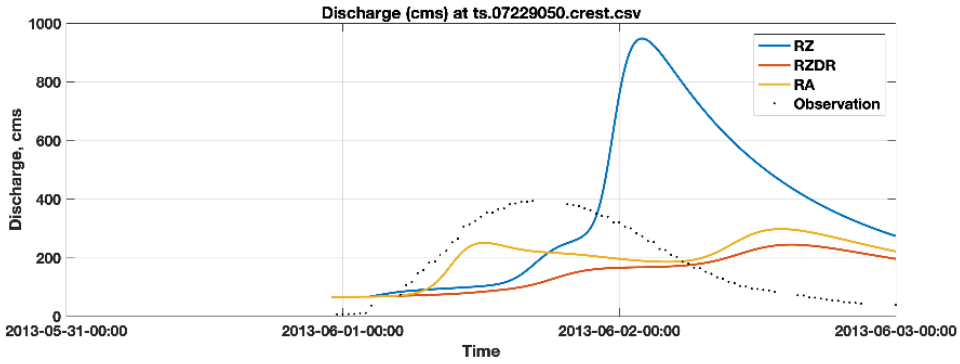

(c) USGS 07241550

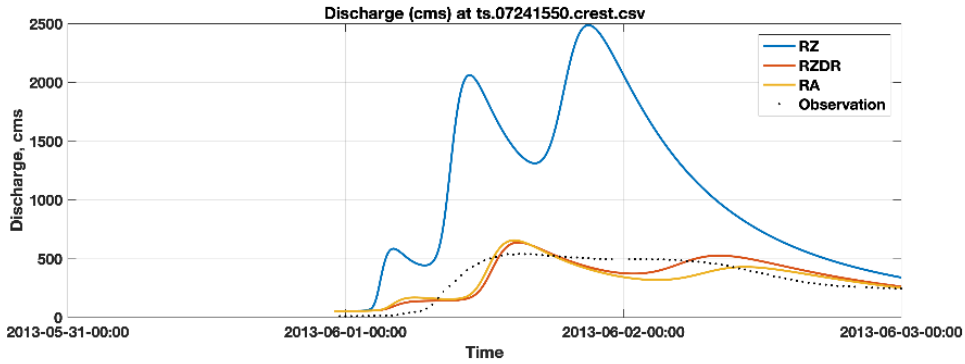

(d) USGS station 0724380

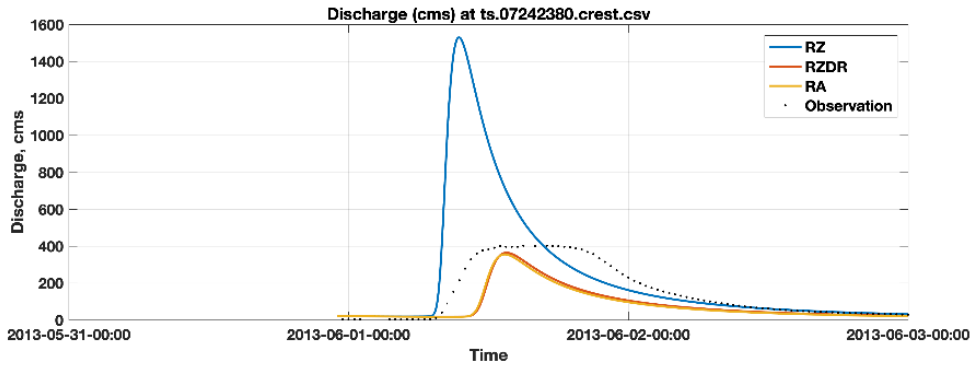

Figure 2.3.8. (a) Peak unit discharge simulated from EF5 using R(A) for 31 May, 2013, El Reno flash flooding/tornado event; (b-c) Time series of simulated discharge from three QPE products compared with stream gauge observations. The location of the three stream gauges are denoted in Fig. (a).

KOUN Data Collection

The meteorological and hydrologic studies presented here required the collection of rapid-update KOUN WSR-88D datasets using volume coverage patterns (VCP) that were designed to provide volumes with 1-2 minute update times, thereby allowing them to be used as a proxy for phased-array radar data. These data would then be analyzed to determine potential advantages of rapid-update radar data to the research and operational communities. Since September of 2017, SENSR funding supported the collection of KOUN data on 28 different days, including 9 days with tornadic storms, 4 days with downburst-producing storms, 13 days with heavy-rain and/or flash-flood producing storms, and 2 days with winter precipitation. As part of this data collection effort, KOUN was also used to collect alternating volumetric data of horizontal (PPIs) and vertical (RHIs) scans starting in the spring of 2019. These data sets will be used in future studies to evaluate how a phased-array radar's adaptive scanning capabilities, where data collection in RHI mode is much easier than with a dish antenna, might be most advantageous for observing severe thunderstorms features. Any knowledge gained from these datasets could inform future radar network design.

Summary and future work

SENSR funding was used to collect data with the dual-polarization KOUN WSR-88D radar using rapid-update sector scans that provided 1-2 minute updates that could be used as a proxy for phased array radar data in order to evaluate potential meteorological and hydrological benefits of dual-polarization phased-array radars. These studies found that:

- Rapid-update observations of Z_{DR} column depth can provide forecasters with 3.5-9.0 additional minutes to anticipate storm threats and issue severe thunderstorm warnings with greater lead time.

- Rapid-update observations of downburst precursor signatures, such as the K_{DP} core, might provide information that will allow forecasters to better anticipate the intensity of an impending downburst.
- Rapid-update observations of MESH and STD (used to predict hail production and storm severity) indicate increases/decreases in those variables over time that is much shorter than the typical volume update time of WSR-88Ds.
- Hydrologic discharge simulated from rapid-update precipitation products provides a better match to stream gauge observations than those generated by the coarser resolution products.

Future work will continue to examine severe storm precursor signatures with an emphasis placed on identifying and quantifying potential benefits that rapid-update, dual-polarization radar data might be able to provide for tornadic storms. In particular, tornadoes associated with quasi-liner convective systems (QLCS), which can be especially challenging to predict because they are short-lived, shallow, and develop very quickly. Rapid-update radar data may be able to provide precursor signatures that could give forecasters a few extra minutes of time to anticipate the development of these tornadoes (e.g., Mahale et al. 2012). Work on this objective was initiated in the summer of 2019 as a Research Experiences for Undergraduates (REU) program student identified several radar signatures that could provide such information to forecasters. Future research will quantify the evolution of these signatures relative to tornadogenesis and explore potential advantages of rapid-update radar data during QLCS events. Potential benefits provided by a PARs adaptive scanning capabilities, such as its ability to collect data in Range Height Indicator (RHI) mode, will also be examined.

SENSR-Funded Conference and Journal Articles:

Kurdzo, J. M., Y. Wen, C.M. Kuster, J.Y. N. Cho, and T. J., Schuur, Investigating the Impact of Radar Observation Height on Streamflow Modeling: The 31 May 2013 El Reno/ Oklahoma City, OK Flash Flood Case, AMS Annual Meeting, Boston, January 12-16, 2020.

Kuster, C. M., J. C. Snyder, T. J. Schuur, J. W. Brogden, R. Toomey, and P. L. Heinselman, 2018: Rapid-Scan Radar Observations of Z_{DR} Column Depth and Its Potential Use During the Warning Decision Process. *29th Conference on Weather Analysis and Forecasting*. Denver, CO, American Meteorological Society, Boston, 15A.7.

Kuster, C. M., J. C. Snyder, T. J. Schuur, T. T. Lindley, P. L. Heinselman, J. C. Furtado, J. W. Brogden, and R. Toomey, 2019: Rapid-update radar observations of Z_{DR} column depth and its use during the warning decision process. *Wea. Forecasting*, **34**, 1173–1188.

Kuster, C. M., B. R. Bowers, T. J. Schuur, J. T. Carlin, J. W. Brogden, and R. Toomey, 2019: Identifying downburst precursor signatures in K_{DP}. *Extended Abstract, 35th Conf. on Environmental Information Processing Technologies*, Phoenix, AZ, Amer. Meteor. Soc., 9B.1. [Available online at https://ams.confex.com/ams/2019Annual/mediafile/Manuscript/Paper350564/Kuster-et-al-35EIPT_Extended_Abstract.pdf]

McCauley, O. F., C. M. Kuster, V. N. Mahale, and T. J. Schuur, 2019: Evolution of dual-pol radar signatures of QLCS tornado development. [Available online at http://www.caps.ou.edu/reu/reu19/finalpapers/ McCauley-finalpaper.pdf]

Wen, Y., T. J. Schuur, H. Vergara, and C. Kuster, 2019: Effect of Precipitation Sampling Error on Flash Flood Monitoring and Prediction: Anticipating Rapid-Update Weather Radars. Submitted to *J. Hydrometeor*.

Wen, Y., T. Schuur, H. Vergara, and C. Kuster, 2019: Advancing flash flooding early warning using a proxy of PAR observations. *39th Conference on Radar Meteorology*, Nara, Japan, American Meteorological Society, Boston, Poster2-03.

Wen, Y., T. Schuur, H. Vergara, and C. Kuster, 2019: Advancing flash flooding early warning using a proxy of PAR observations. AMS Annual Meeting, Symposium on Phased Array Radar. Phoenix, AZ, American Meteorological Society.

Wen, Y., T. Schuur, H. Vergara, and C. Kuster, 2018: Advancing flash flooding early warning using a rapid-scan polarimetric radar observations. *9th Workshop of International Precipitation Working Group*, Seoul, South Korea.

Witt, A., D. W. Burgess, A. Seimon, J. T. Allen, J. C Snyder, and H. B. Bluestein, 2017: Rapid-scan radar observations of an Oklahoma tornadic hailstorm producing extremely large hail. *Mon. Wea. Rev.*, **33**, 1263-1282.

Witt, A., and C. M. Kuster, 2017: Rapid-scan dual-polarization WSR-88D observations of Oklahoma hailstorms on 26 March 2017. *38th Conference on Radar Meteorology, Chicago, IL*.

References:

Andra, D. L., E. M. Quoetone, and W. F. Bunting, 2002: Warning decision making: The relative roles of conceptual models, technology, strategy, and forecaster expertise on 3 May 1999. *Wea. Forecasting*, **17**, 559–566.

Brown, R. A., V. T. Wood, and D. Sirmans. 2002. Improved tornado detection using simulated and actual WSR-88D data with enhanced resolution. *J. Atmos. Oceanic Technol*., 19, 1759–1771.

Gourley, J.J., and Coauthors, 2011: Hydrologic evaluation of rainfall estimates from radar, satellite, gauge, and combinations on Ft. Cobb Basin, Oklahoma. *J. of Hydrometeor*., 12, 973-988.

Huffman, G.J., D. T. Bolvin, D. Braithwaite, K. Hsu, R. Joyce, C. Kidd, E. J. Nelkin, and P. Xie, 2015a: NASA Global Precipitation Measurement (GPM) Integrated Multi-satellitE Retrievals for GPM (IMERG). Algorithm Theoretical Basis Doc., version 4.5, 26 pp.

Isaminger, M. A., 1988: A preliminary study of precursors to Huntsville microbursts. Lincoln Laboratory Project Report ATC-153. 21 pp.

Kumjian, M. R., 2013: Principles and applications of dual-polarization weather radar. Part II: Warm and cold season applications. *J. Oper. Meteor.*, **1**, 243–264.

Mahale, V. N., J. A. Brotzge, and H. B. Bluestein, 2012: An analysis of vortices embedded within a quasi-linear convective system using X-band polarimetric radar. *Wea. Forecasting*, **27**, 1520–1537.

Nijssen, B., and D. P. Lettenmaier, 2004: Effect of precipitation sampling error on simulated hydrological fluxes and states: Anticipating the Global Precipitation Measurement satellites. *J. Geophys. Res.*, **109.**D02103, doi:10.1029/2003JD003497.

Roberts, R. D., and J. W. Wilson, 1989: A proposed microburst nowcasting procedure using single-Doppler radar. *J. Appl. Meteor.*, **28**, 285–303.

Ryzhkov, A. V., V. B. Zhuravlyov, and N. A. Rybakova, 1994: Preliminary results of X-band polarization radar studies of clouds and precipitation. *J. Atmos. Oceanic Technol.*, **11**, 132–139.

Snyder, J. C., A. V. Ryzhkov, M. R. Kumjian, A. P. Khain, and J. C. Picca, 2015: A Z_{DR} column detection algorithm to examine convective storm updrafts. *Wea. Forecasting*, **30**, 1819–1844.

2.4. Impact of Phased Array Radar on Aviation Weather Forecasting[4]

Motivation

The National Center for Atmospheric Research (NCAR) has conducted an observing system simulation experiment (OSSE) study to assess the benefits of rapid scan phased array radar (PAR) data for aviation weather forecasting. With the prospect that the U.S. radar network could be upgraded to PAR, it is vital to evaluate the potential benefits of PAR on data assimilation and convective forecasting with numerical weather prediction models. We performed such an evaluation using NCAR's 4DVar radar data assimilation system VDRAS (Variational Doppler Radar Analysis System) and its forecasting model on a strong weakly-forced convective case that occurred on 7-8 Aug 2018 at the NYC airport complex comprising the combined JFK, EWR & LGA Terminal Control Area (TCA). Our focus was to assess the expected improvement in 1 & 2 hour terminal area forecasts by comparing 1 minute PAR electronic volume scans to 5 minute mechanical volume scans of the WSR-88D/Nexrad & TDWR radars.

The Observation Simulation System Experiment (OSSE) is an effective tool for the purpose of observation system design & evaluation and has been used in several previous studies concerning radar data assimilation (Sun et al. 1991, Sugimoto et al. 2009, Caya et al. 2005, Chang et al. 2013). In an OSSE, synthetic "observations" are extracted from a model simulation ("truth" or Nature Run), which enables an evaluation of the impact of observation quality and network design on data assimilation and subsequent model forecasts. We designed OSSEs in the current study to answer the following questions:

- What benefit is gained by PAR to better capture the rapid evolution of convective weather and its associated aviation hazards?
- How does the PAR benefit depend on the radar coverage improvement by adding more radars?
- How much additional benefit will be gained by enhanced low level coverage?
- How will the PAR benefit be impacted by uncertainties in radar observation?

In this study we use metrics based on both standard *error estimation* of model dynamic variables (wind, temperature, moisture, etc.) and *detection statistics* of convection to verify the forecast performance. The detection statistics are performed on high reflectivity that may define the availability of the airport controlled airspace for take-off & landing operations. The verification is performed not only in the OSSE domain but also in two subdomains that approximates respectively the NYC airport area and TCA.

[4] Principal Investigators: Jenny Sun, Jeff Keeler and Zhuming Ying (NCAR)

Description of VDRAS

Radar data assimilation is a crucial component of short-term numerical weather prediction (NWP) for high impact weather. Active research has been carried out to develop suitable methodologies for effective assimilation of the Nexrad national weather radar network since the early days of its installation. NCAR is one of a few organizations who have played a major leadership role in the radar data assimilation effort over the past three decades. The pioneering research conducted by NCAR scientists using a cloud-scale model and its 4-dimensional variational (4DVar) data assimilation system, VDRAS (Sun et al. 1991; Sun and Crook 1997), encouraged a world-wide application of radar observations in NWP models. In recent years, NCAR has developed additional radar data assimilation capabilities for the WRF community model with both variational and ensemble-based data assimilation techniques including WRFDA 3DVar/ 4DVar and EnKF/DART (Xiao et al. 2005, Aksoy et al. 2010, Wang et al. 2013). These community radar data assimilation systems have been used by universities as well as mission agencies for both research and real-time operations. NCAR has also been collaborating with NSSL through the NOAA Hazardous Weather Testbed Spring Forecasting Experiments to evaluate the value of high-resolution ensemble prediction over the CONUS domain in recent years.

Although any of the above data assimilation systems can be used for the current OSSE study, we chose VDRAS because the 4DVar technique used in the system is capable of assimilating rapid update observations, making it particularly suitable for the evaluation of PAR. Compared to other 4DVar systems (e.g., Kawabata et al. 2011; Sun and Wang 2013; Wang et al. 2013; Ballard et al. 2016), the uniqueness of VDRAS is its specific application in storm-scale weather analysis and nowcasting, as it can provide rapid update cycles every 15 minutes or less (Chang et al. 2014, 2016).

The main data source for VDRAS includes volumetric radar observations of radial velocity and reflectivity and surface observations. These data are assimilated in a continuous cycling fashion with a short 4DVar window aiming to capture detailed convective-scale flow structure. The analysis and forecast fields produced by VDRAS comprise a set of high-resolution three-dimensional model state variables such as winds, thermodynamic fields, radar reflectivity and microphysical parameters.

NYC Terminal Control Area, the convective case, and OSSE design

Since our objective is to evaluate the impact of PAR on aviation applications of convective forecasting, we selected a convective case that affected the NYC Terminal Control Area (TCA). A typical isolated airport TCA is shaped generally like an upside-down wedding cake comprising the surface to 12000 feet. However, the NYC TCA (Fig. 2.4.1) is irregularly shaped because the nearby 3 airports use this common airspace that tops out at 7000 feet. We defined a simplified NYC TCA domain that approximates the actual TCA as an inverted, truncated

pyramid with a lower layer that spans at all 3 airports at the surface and expanding to a larger area at the 7000 feet top.

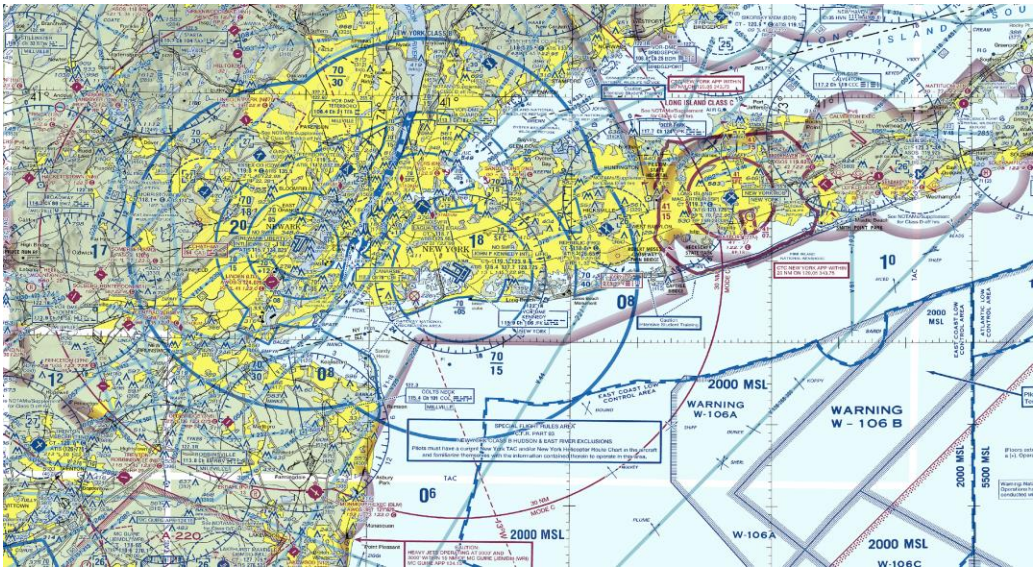

Fig. 2.4.1: New York City Terminal Control Area comprising JFK (Kennedy), EWR (Newark) and LGA (LaGuardia) airports from the NYC sectional aeronautical chart.

Experimental and Evaluation Domains. The OSSEs are conducted in Domain 1 (D1) shown Fig. 2.4.2 which encompasses the entire 220 km square domain up to 15 km. The forecast verification is performed on this domain and two other domains. Domain 2 (D2) covers a smaller 110 km x 90 km rectangular area up to 8 km where the most congested air traffic is expected to exist and Domain 3 (D3) is a close approximation to the actual NYC TCA. These domains are listed below:

D1 = Full domain - 220 km x 220 km x 15 km

D2 = Airport Terminal Control sized domain - 110 km x 90 km x 8 km

D3 = NYC Terminal Control Area (TCA) domain - inverted & truncated pyramid containing flight corridors

Base: 60 km x 40 km increasing to Top: 110 km x 90 km x 2.25 km (7000')

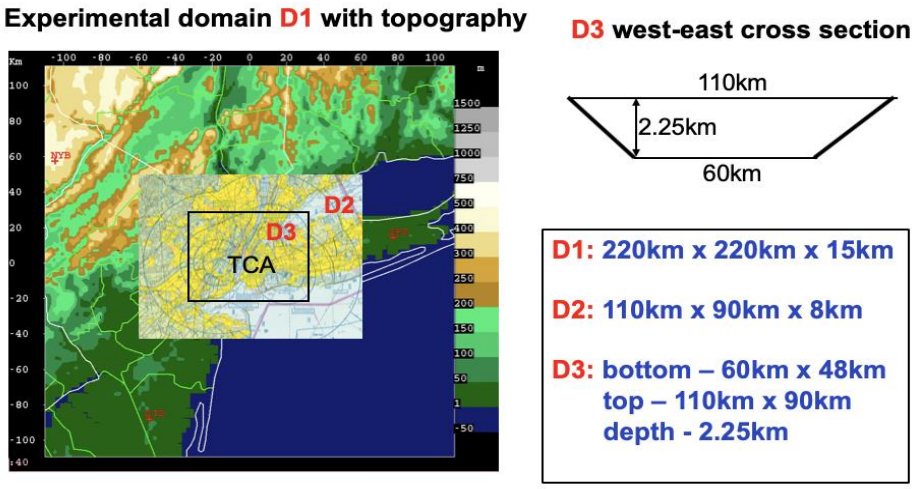

Fig. 2.4.2. The OSSE domain D1, NYC airport area D2 and Terminal Control Area domain D3.

Typically a good 1 hour forecast would be most useful to the Terminal Radar Control (TRACON) at most airports. However, in the NYC TCA the complexity of the approach & departure aircraft control for 3 major airports mandates a reliable 2 hour forecast. Consequently, we perform & critically evaluate both 1 hour & 2 hour forecasts. We use forecasts at 5 minute intervals from a "Nature Run" that is described below for the evaluation of our data assimilation experiments.

NYC Aug 7, 2018 case and Nature Run. We have chosen a strong, weakly-forced convective case that occurred on 7-8 Aug 2018 at the NYC airport complex. Fig. 2.4.3a shows the 0.5^{o} elevation reflectivity of the convective storm mosaicked by the KOKX and KDIX WSR-88D radars, starting at 22:30 UTC as it approached the NYC airport complex from the NW and generated a leading line of severe convection over the 3 airports at 23:30 and then moved southeastward.

A Nature Run is necessary for the OSSE to generate synthetic observations and to provide "truth" for forecast verification. Our Nature Run is initiated by assimilating the Nexrad Level 2 VCP12 data from KDIX & KOKX and the rather limited Level 3 low elevation scans from TJFK & TEWR TDWR radars, as that is all that was available. The Nature Run, a two hour simulation with a 1km resolution starting at 22:30 and shown in Fig. 2.4.3b, captured the gross characteristics of the storm initiation, although it is lacking in the degree of growth and other details.

Synthetic observations. Synthetic observations of radial velocity and reflectivity are extracted from the Nature Run for 5 radars (Fig. 2.4.4 shows for their locations), mimicking the Nexrad radars KOKX at Upton, NY and KDIX at Ft. Dix, NJ, the TDWR radars TEWR at the EWR airport and TJFK at the JFK airport, and a filler radar labeled "KNYB" similar to KOKX and KDIX. To generate the synthetic observations, we use the Nexrad VCP12 having 14 elevations in ~5 minute VCPs as the baseline scan with maximum range to 230 km for the Nexrad radars

and to 150km for the TDWR radars. The maximum range for clear air echoes are assumed to be 60 km for the Nexrad radars and 50 km for the TDWR radars linearly decreasing to the PBL top. The reflectivity threshold of 10 dBZ is used to limit the radial velocity coverage only in storm regions above the PBL.

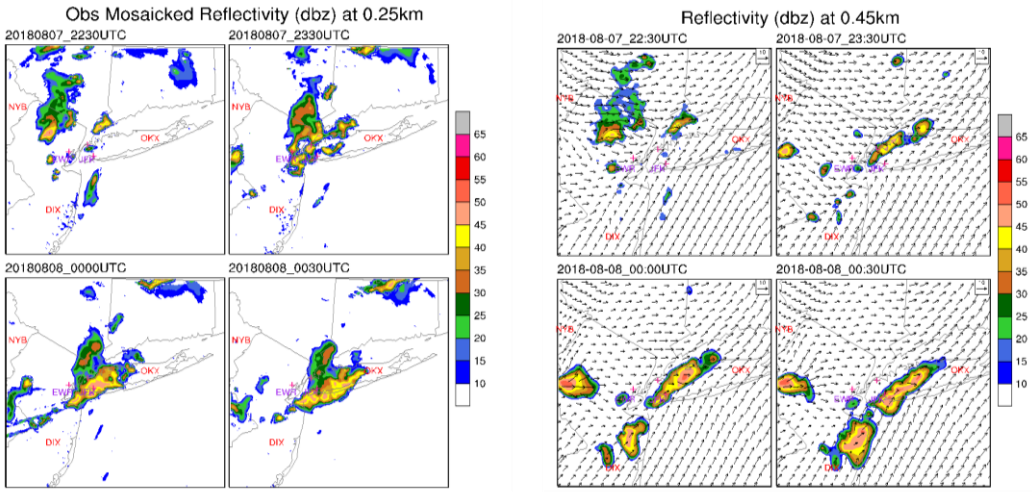

Fig. 2.4.3. (a) Left: NYC storm overview on Aug 7-8, 2018 showing mosaicked KDIX & KOKX reflectivity observations at vertical level z = 250m for four different times. (b) Right: Nature Run of VDRAS cloud model simulated reflectivity at z = 450m for the same times. The Nature Run captures the decay of the parent storm and the initiation of the convective line near the airports.

Design of data assimilation experiments. We designed eight data assimilation experiments, summarized in Table 2.4.1, assimilating varied amount of synthetic observations by VDRAS 4DVar. The first set of four experiments (will be referred to as "Nex" hereafter) assumes 5-min VCP radar data. The baseline experiment Nex-N2_14 only assimilates data from the two simulated Nexrads KOKX and KDIX (N2). We then add the two TDWR radars TEWR & TJFK (T2) that are located 10-15 km west of the respective EWR & JFK airports (Nex-N2T2_14). The experiment Nex-N3T2_14 is designed to test the benefit of a potential filler radar. We further compare the 14 scans with 15 scans that add a 0.2 degree elevation scan to VCP12 in the experiment Nex-N3T2_15. We expect the added low level scan will add important boundary layer information for forecasting storm cell initiation. The second set of four experiments ("PAR") repeats the first with the only difference being the VCP time - 5 min for Nex and 1 min for PAR experiments. It is worth noting that a comparison between 30 sec and 1 min PAR showed little difference, so all PAR experiments presented here use 1 min VCP data.

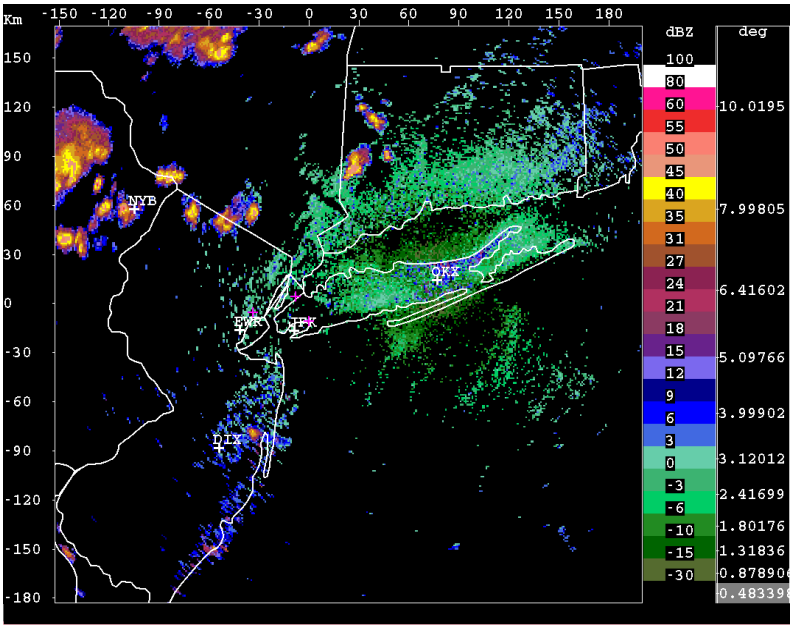

Fig. 2.4.4. NYC area airports and radar configurations used for the OSSE experiments. The two Nexrad radars are shown by the labels "DIX" and "OKX", the TDWR radars are shown by "EWR" and "JFK" and the three airports are shown by magenta "+" symbols. The third gap-filler Nexrad radar (KNYB) is shown by the label "NYB".

Nex: 5 min WSR-88D scanning
PAR: 1 min Phased Array Radar scanning
N#: number of NEXRADs
T#: number of TDWRs
_#: number of scanning elevations.

Experiment	Radars assimilated	Elevations	Purpose
Nex-N2_14	KOKX and KDIX	14 (VCP12)	Benchmark
Nex-N2T2_14	KOKX, KDIX, TEWR, and TJFK	14 (VCP12)	Impact of TDWR
Nex-N3T2_14	KOKX, KDIX, TEWR, TJFK, and KNYB	14 (VCP12)	Impact of a gap filler
Nex-N3T2_15	KOKX, KDIX, EWR, TJFK, and KNYB	15 (VCP12+0.2)	Impact of low-level scan
PAR-N2_14	KOKX and KDIX	14 (VCP12)	PAR benchmark
PAR-N2T2_14	KOKX, KDIX, TEWR, and TJFK	14 (VCP12)	PAR impact with TDWR
PAR-N3T2_14	KOKX, KDIX, TEWR, TJFK, and KNYB	14 (VCP12)	PAR impact with a gap filler
PAR-N3T2_15	KOKX, KDIX, EWR, TJFK, and KNYB	15 (VCP12+0.2)	PAR impact with low-level scan

Table 2.4.1: Summary of OSSE Experiments

The "Nex" & "PAR" data assimilation experiment structure is shown in Fig. 2.4.5. The Nature Run is initialized at 22:30 UTC by VDRAS 4DVar analysis starting from a background, or 'first guess' dataset taken from a 15 km resolution WRF run valid at 22:00. The Nature Run simulation with a 1 km resolution is then produced by the VDRAS cloud model that generates 1 minute updated fields of the model variables, e.g. (u, v, w) wind triplets, temperature, water vapor mixing ratio, rain water and snow mixing ratio, etc. Some of these fields are used to

compose radar radial velocity and reflectivity observations as synthetic data inputs to the data assimilation experiment runs. They are also used for comparison as "synthetic truth" for verification. We allow the VDRAS cloud model to evolve the Nature Run until 00:45 to produce the forecasts, actually "nowcasts", up to 2 hours.

The radar data assimilation experiments have resolution of 2 km and start from a first guess taken from the 15 km WRF forecast field valid at 21:00, 90 minutes before the actual initialization at 22:30, in considering the fact that the first guess contains error. We then perform two 5 minute assimilation cycles of synthetic observations from the Nature Run until 22:45. After the assimilation, the VDRAS cloud model is integrated forward making forecasts valid for the next 2 hour period until 00:45. The only difference between Nex and PAR is the update frequencies of the assimilated radar data.

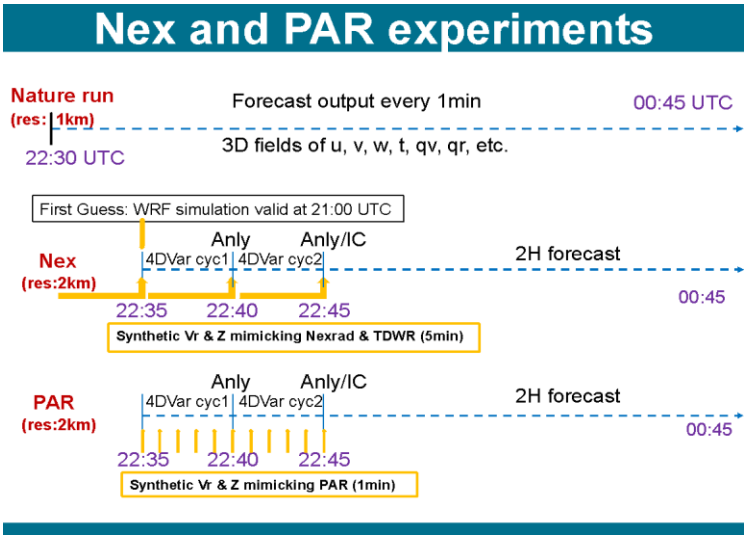

Fig. 2.4.5. Illustration of OSSEs showing Nature Run and the data assimilation runs Nex assimilating 5 minute VCP and PAR assimilating 1 minute VCP. Note that the resolution for the Nature Run is 1 km & for the OSSE radar experiments is 2 km.

Results

We first compare the reflectivity and wind fields at the initialization time 22:45 UTC from VDRAS 4DVar analysis in Fig. 2.4.6 for the 8 experiments assimilating different radar configurations defined in Table 2.4.1, with the Nature Run "truth" shown at the top left corner for verification. We have highlighted the "Current" 2 Nexrad only configuration (Nex-N2_14) and the "Hypothetical" PAR (PAR-N3T2_15) configuration using the 5 radars and added 0.2 degree elevation scan to allow a more focused comparison of the two "worst" and "best" radar configurations.

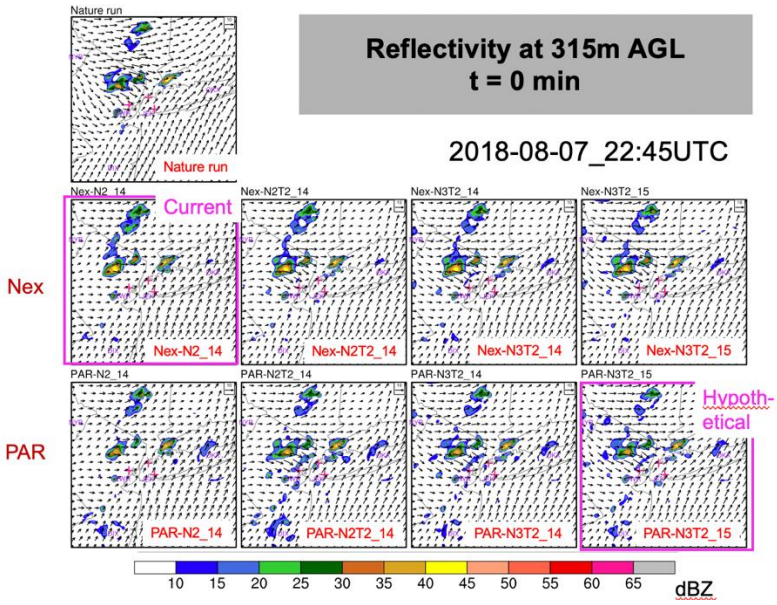

Fig. 2.4.6. 4DVar analysis fields of radar reflectivity & winds for the 4 Nex experiments (upper row from left to right: Nex-N2_14, Nex-N2T2_14, Nex-N3T2_14 and Nex-N3T2_15) and 4 PAR experiments (lower row from left to right: PAR-N2_14, PAR-N2T2_14, PAR-N3T2_14 and PAR-N3T2_15) at 22:45 UTC. The Nature Run "truth" is shown at the top left for verification.

We first note in Fig. 2.4.6 that the maximum reflectivity in the Nex experiments is overestimated compared to their counterparts in PAR and in Nature Run and the PAR experiments generate some low-echo noises although these noises quickly disappear as the model is integrated forward. The more significant differences among these 8 experiments are seen from the wind field in the northwest part of the domain. The northwesterly flow is mostly missed in the Nex_N2_14 and PAR_N2_14 experiments, but adding the two TDWR radars, the filler radar, and the low-level scan produces incremental improvements. And the best agreement with the Nature Run is shown by the experiment PAR-N3T2_15 in terms of both wind direction and speed. The initial wind differences result in differences of subsequent 2-hour convective forecasts. In Fig. 2.4.7 the reflectivity and wind forecasts at t = 75 min are shown, illustrating the impact of different data configuration on the subsequent forecasts. Although both sets of experiments capture to some degree the evolution of the strong main convective line over the airport area, but only the Hypothetical PAR 1 minute scan update captures the initiated cell near the northern boundary of the domain and the storm cell near the western boundary and its associated wind outflow moving east, potentially disrupting air traffic flow in the TCA. Not even the additional KNYB radar upstream of the NYC airport complex making 5 minute VCPs captures this cell.

In Fig. 2.4.8 we show the 2-hour accumulated rainfall forecasts from the experiments Nex_N2_14, Nex_N3T2_15, and PAR_N3T2_15, representing radar configurations of the current, the "best" radar coverage, and the hypothetical PAR. This comparison gives additional evidence of the improved forecast skill for precipitation accumulation of the Hypothetical PAR experiment over the Current two-Nexrad configuration. It also provides additional evidence of the importance of PAR for improving the local severe storms near the west and north boundaries (comparing PAR-N3T2_15 with Nex-N3T2_15) and the importance of improving radar

coverage. Forecasts of this information may have implications for the time required to return wet airport runways to operation.

Verification of model forecast RMSE. Root Mean Squares Error (RMSE) is used as a metric for comparing different experimental radar configurations. The RMSE is computed against the Nature Run using each grid point for wind, temperature, humidity, rain water/snow mixing ratio, and precipitation. Here we only show the verification results of water vapor (Qr) and velocity vector difference (VVD) because of their close relevance to airport operations.

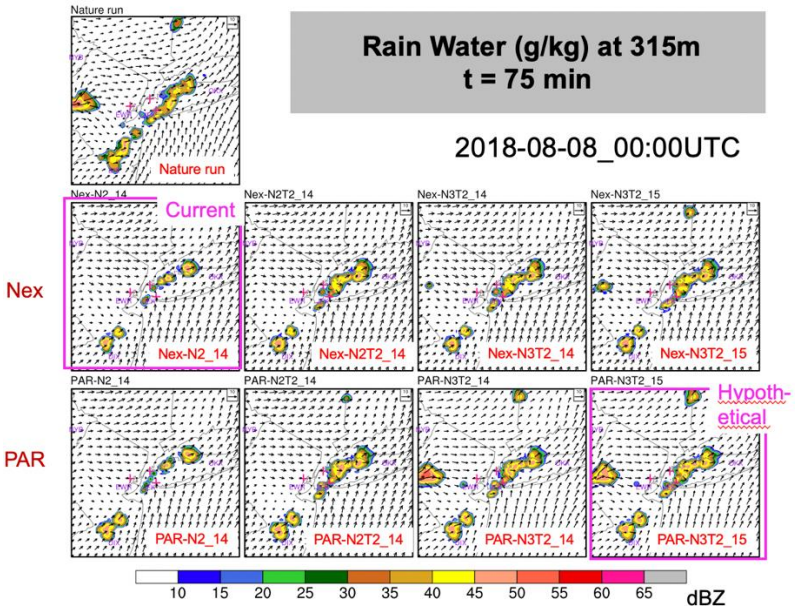

Fig. 2.4.7. Nature Run and OSSE forecasts of radar reflectivity & winds for each radar configuration (OSSE experiment) shown at t = 75 min, 00:00 UTC. The "Current" 2 radar & "Hypothetical" 5 radar forecasts are emphasized for the most relevant conclusions. Note initiation of the isolated cell at the western boundary.

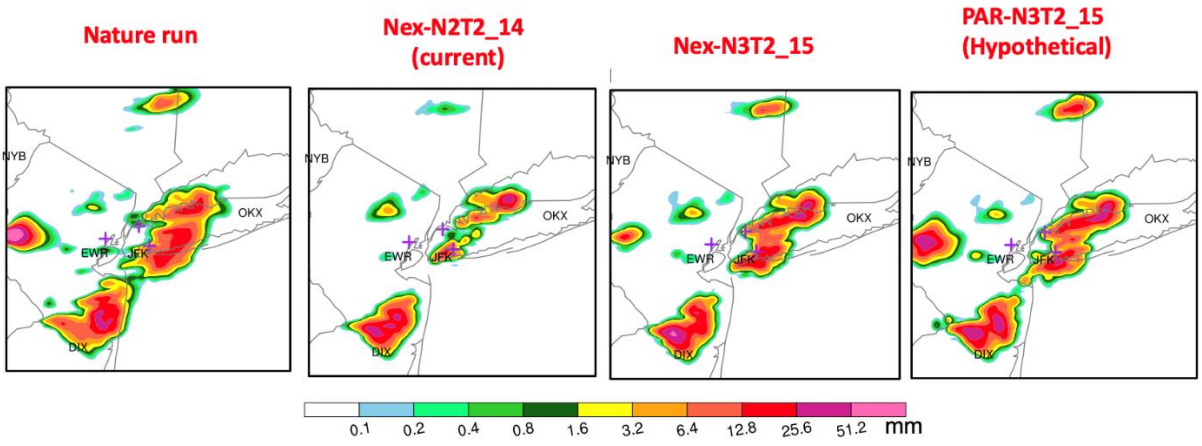

Fig. 2.4.8. Two hour accumulated rainfall of the Nature Run, the "Current" 5 minute Nex-N2_14 configuration, the Nex-N3T2_15 configuration, and the "Hypothetical" 1 minute PAR-N3T2_15 configuration. Faster update rates & better low PBL coverage give improved precipitation forecasts.

Fig. 2.4.9a and 2.4.9b compares the RMSEs of Qr and VVD respectively for the 8 experiments in all three domains. The following observation can be made from this verification. The RMSE differences of VVD occur mainly at the forecast time beyond 30 minutes in all the domains. The largest impact on wind forecasts is produced by PAR_N3T2_14, Nex_N3T2_15, and PAR_N3T2_15, suggesting the large sensitivity of wind forecasts to radar coverage and PAR scanning especially near the three NYC airports. When the two TDWR radars are assimilated, the RMSE of Qr are much reduced from the experiment that assimilates only the two NEXRAD radars, whether or not the 1 minute PAR scanning is assumed. The VVD verification in D3 indicates that the assimilation of TDWRs (all experiments except for Nex_N2_14 and PAR_N2_14) significantly improves the wind analysis but the benefit lasts only for 30 min and from that time on the low level scan and the PAR scan play a crucial role.

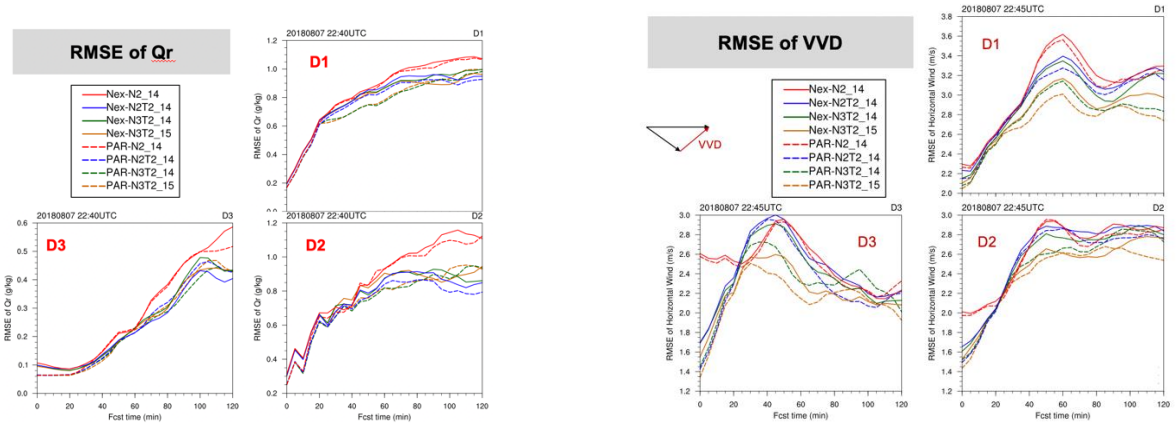

Fig. 2.4.9. (a) left: Verification of rainwater mixing ratio (Qr) forecasts in all domains (D1-upper right; D2-lower right; D3-lower left) using RMSE. (b) right: Same as (a) but for the magnitude of the Velocity Vector Difference (VVD).

Verification of radar reflectivity detection. We performed verification for radar reflectivity using detection metrics of POD, CSI, FAR and FBI, which are summarized below:

- POD (Probability of Detection) from 0 (poor) to 1 (good)
- FAR (False Alarm Ratio) from 0 (good) to 1 (poor)
- CSI (Critical Success Index) from 0 (poor) to 1 (good)
- FSS (Fractional Skill Score) from 0 (poor) to 1 (good)
- FBI (Frequency Bias Index) from <1 (under-forecast), =1 (unbiased), >1 (over-forecast)

For our purpose the "event" to be detected is "Airspace open", meaning a grid point measurement of Z < 35 dBZ. If the experiment shows Z < 35 dBZ at the same grid point as in the Nature Run, we have a 'detection' and build up statistical contingency tables of detection statistics for this "Airspace open" event. Fig. 2.4.10a and 2.4.10b give the detection statistics in Domains 1 and 2 respectively. The statistics in Domain 3 are not shown because they have similar characteristics to those in D2.

Study of these dBZ detection statistics clearly shows three important conclusions. First, the POD, FAR & CSI scores are all quite poor in general. This condition may reflect the manner in which we performed the grid point by point detection computation. For aircraft control, these poor statistics may not be a problem if enough open airspace exists for operations to continue wherever that open airspace may occur. We address this fact in our Domain Available Airspace tests later in the report. Second, the experiment using only the two Nexrad radars (Nex-N2_14, the red curves) gives significantly lower forecast skill than when adding the two TDWR radars or the gap filler Nexrad radar to the two Nexrad radars. This means that better radar coverage in the experimental domain is extremely important in making better forecasts, as is expected. The only exception is that the FAR is generally better, i.e. smaller, in all domains during the first hour but that factor does not show up in the CSI statistic, which seems to be dominated by the POD instead of the FAR. Furthermore, the FBI scores show that the present two Nexrad configuration significantly under-forecasts convective activity in all three domains. Third, the 1 minute VCP PAR systems show improvement in all the detection statistics in all the domains but is most clearly evident in D1.

Domain Airspace Availability (DAA). An extremely useful metric of aviation forecast improvement is the TCA domain airspace availability forecast. If we use the radar reflectivity Z as a measure of how much airspace may be 1) open due to Z values less than some threshold dBZ or closed due to Z values greater than the same or a larger threshold dBZ, then we may calculate the percent of total TCA that is open airspace available for flights as well as airspace closed to flights. Here, we define the instantaneous DAA by the fraction of grid points with dBZ values smaller than 35 dBZ. We also verified the temporally accumulated airspace availability (TDAA) using the accumulated coverage area of 35 dBZ reflectivity between the forecast issue time and the forecast valid time, which provides a measure of airspace availability up to that forecast valid time. In Fig. 2.4.11, the two inserts in the middle of upper row illustrate how DAA and TDAA are defined. We expect that a reduced error in forecast DAA or TDAA of the PAR system at all forecast times would assist in validating the PAR rapid & adaptive scanning network.

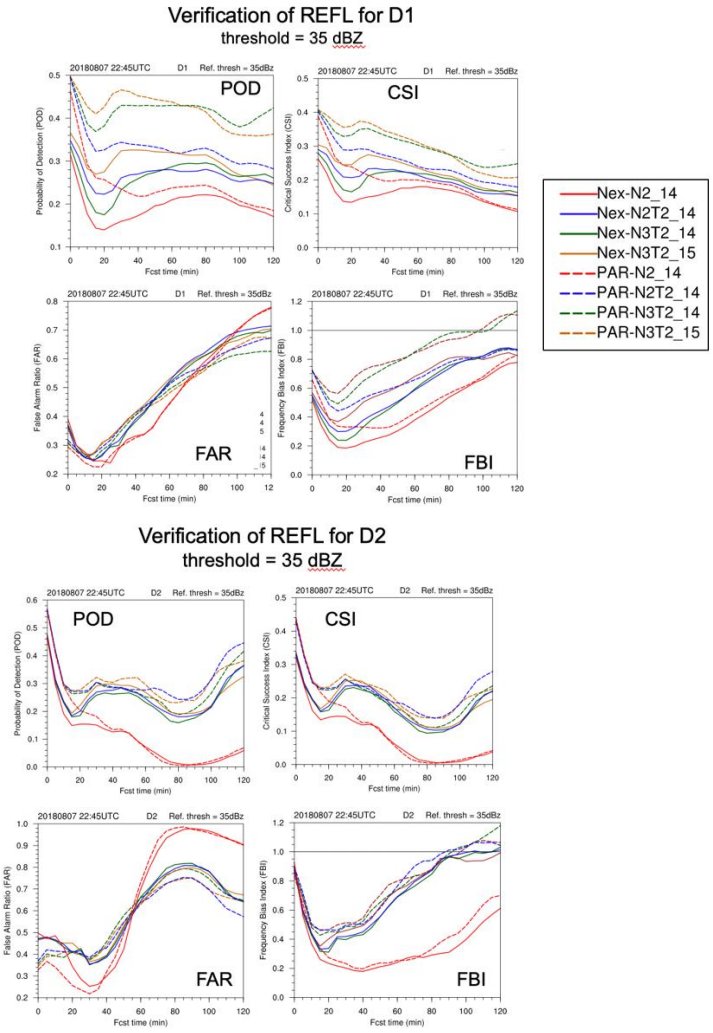

Fig. 2.4.10. (a) left: Verification of radar reflectivity detection statistics (POD, FAR, CSI & FBI) in the full domain D1 for Z = 35 dBZ threshold. (b) right: Same as (a) but for D2.

Both Fig. 2.4.11a and b show that all forecasts overestimate the airspace availability with the Nexrad only experiment (Nex-N2_14, red) performing the worst. The Nexrad only experiment does not provide the coverage required to accurately forecast open airspace in any of the domains. The addition of the low level PBL coverage from the TDWR & gap filler radars provide much better forecasts of DAA. The exception to the overestimation is the individual DAA estimates at longer forecast valid times in D3, which match within 2%. Note again that the assimilation of the two TDWR radars improves the forecast significantly. The positive impact of PAR 1 minute VCPs is shown in all verification domains but a larger impact is achieved only in the larger domain.

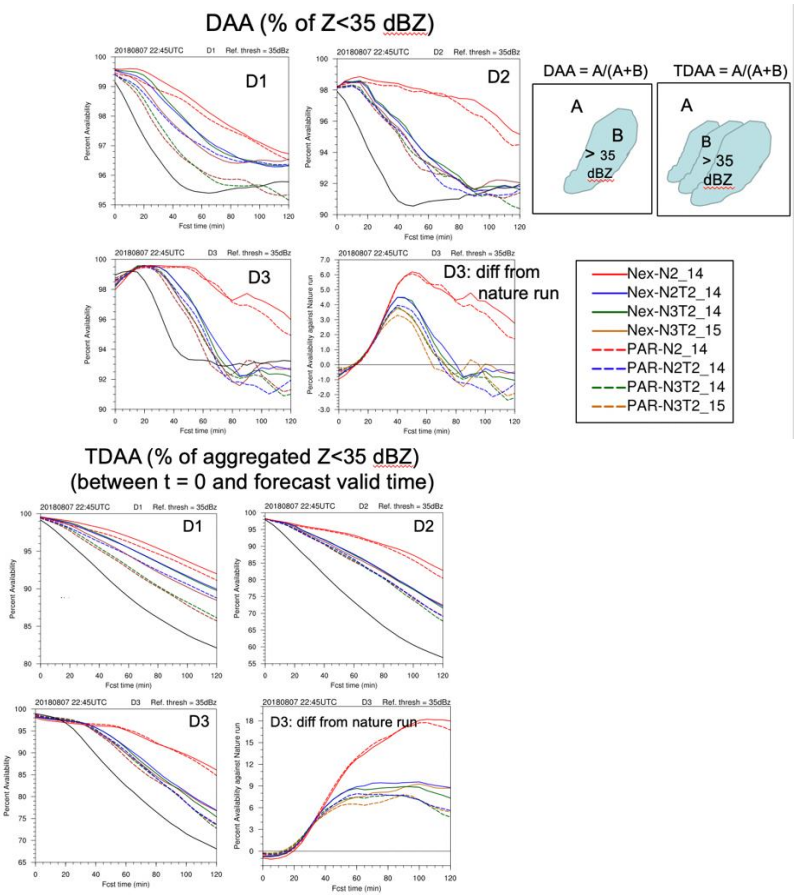

Fig. 2.4.11. (a) left 4 panels: Domain Airspace Availability percent for radar reflectivity Z < 35 dBZ in domain D1 (upper left), D2 (upper second) and D3 (lower left). Note the black curve is the DAA from the Nature Run, representing the "truth". The difference of DAA between the Nature Run & the OSSE forecasts for D3 are shown in the lower second panel. (b) right 4 panels: Same as (a) but for Temporally accumulated Domain Airspace Availability. The upper middle two panels illustrate the DAA and TDAA definitions.

Impact of observation error

To evaluate the effect of radar observation errors on data assimilation and convective forecasting, we added random observation errors with a constant error variance to all the gridded reflectivity & winds synthetic observations. We use observation standard deviation error of ±2 dBZ for the radar reflectivity Z and ±1 m/s for the radial wind Vr measurements. At some point it may make sense to use inhomogeneous errors, e.g. larger errors in the convective areas than errors in the surrounding quiescent atmosphere. We may be further justified in using larger observation errors in the PBL than in the stable upper layers above.

We repeated all of the 8 experiments in Table with the added observation errors. In this report we present the results for the two pairs of experiments with the "best" radar coverage (Nex-N3T2_15 vs. Nex-N3T2_15+err and PAR-N3T2_15 vs. PAR-N3T2_15+err). Figure 2.4.12

shows the 2-hour accumulated precipitation forecasts valid at 00:45 UTC for the two pairs of experiments. The comparison in Fig. 2.4.12 indicates that adding observation error degrades the forecasts of the two isolated convective cells near the western and northern boundaries in the 5-min VCP experiment (middle column), but it does not appear to cause noticeable degradation in the 1-min VCP experiment (right column).

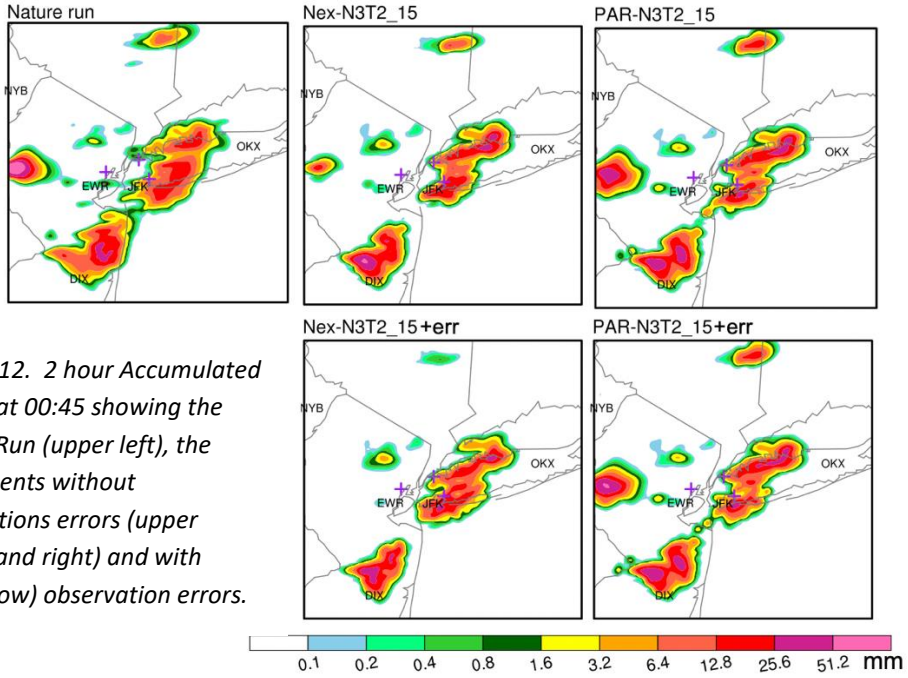

Fig. 2.4.12. 2 hour Accumulated rainfall at 00:45 showing the Nature Run (upper left), the experiments without observations errors (upper second and right) and with (lower row) observation errors.

Statistical verification. The impact of the observation errors is evaluated by computing the RMSE of the model variables as well as the reflectivity detection statistics for all three domains. Compared with the VVD, the Qr RMSE has less difference between the error and no-error experiments, therefore here we only show the VVD verification results in Fig. 2.4.13. The RMSE of VVD is increased beyond the 30 min forecast range when the observation error is added to the Nex-N3T2_15 experiment, as might be expected more generally. However, the PAR experiment shows little or no difference in RMSE with observation error. Thus, we may conclude that typical Vr observation error of ±1 m/s does not have a significant effect on the RMSE of the 1 minute PAR forecasts of wind but it does increase the RMSE of the 5 minute Nex experiment forecasts of wind after about 30 minutes. This reduction in wind error with PAR is important for providing improved aviation wind forecasts.

The detection verification of radar reflectivity forecasts using POD, FAR & FBI is shown in Fig. 2.4.14. Since the observation error impact is most significant for the large domain D1, we only show the statistics of D1 in this figure.

The PODs for reflectivity with observation error are better than the error free data, whereas the FARs are more equal. The FBI values show less biased forecasts during the second hour period

when the observation error is added. The conclusion is that some observation error may improve the forecasts but the reasons are not clear if not due to the "dithering" effect. Similar to the above VVD verification, the reflectivity verification also suggests that the amount of observation errors added in our experiments is not detrimental to the forecasts when the PAR VCP is applied, which is another indication of potential benefit of PAR system.

We have previously described the Domain Available Airspace indicated by the percentage of each domain available for aviation operations, meaning Z < 35 dBZ for our definition at this time. Fig. 2.4.15 shows the instantaneous DAA at each forecast time with and without observation errors for the three domains. The negative effect of the observation error occurs only in the Nex experiment in the first 80 min mainly in D1 because the observation error has an detrimental effect on the two isolated rapid evolving storms in the experimental domain.

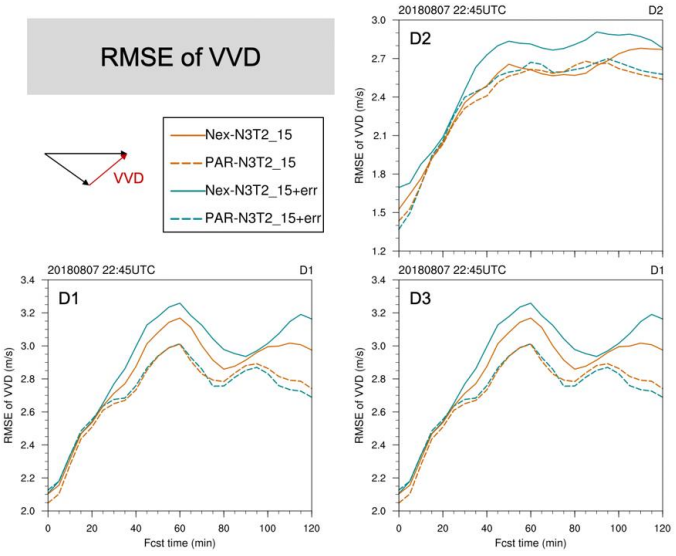

Fig. 2.4.13. RMSE of VVD for the experiments without (Nex-N3T2_15 and PAR_N3T2_15) and with (Nex-N3T2_15+err and PAR_N3T2_15+err) observation error for domain D1 (lower left), D2 (upper right) and D3 (lower right).

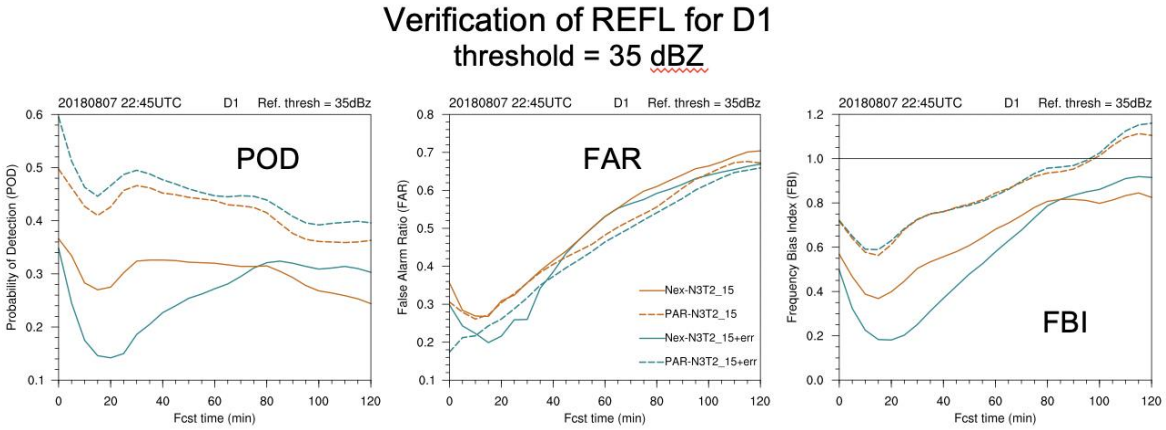

Figure 2.4.14. Verification statistics for radar reflectivity Z = 35 dBZ in domains D1 for the experiments without (Nex-N3T2_15 and PAR_N3T2_15) observation errors and with (Nex-N3T2_15+err and PAR_N3T2_15+err) observation errors.

Findings & Conclusions

OSSEs based on the Aug 7, 2018 storm observations in New York City airspace demonstrate that both rapid scanning and the addition of radars beyond the KDIX and KOKX WSR-88Ds improve analysis and forecasts of the timing of convective initiation and evolution of storms. Indeed, the benefit of PAR based rapid scanning appears to improve as incremental assimilation of data from the NYC TDWR radars, a hypothetical "gap-filler" to the northwest of NYC, and an additional low level scan are included in the data assimilation experiments. Below is a summary of the main conclusions based on our NYC case study:

1. The benefit of PAR to data assimilation and subsequent 0-2 hour forecasts increases as the radar coverage improves, indicating that the two work synergistically. Although all 1 minute PAR experiments result in some improvement over the 5 minute Nexrad counterparts, the best result is obtained by the experiment assimilating all 5 radars (two WSR-88D, two TDWR, and one gap filler) with a low level scan additional to VCP12 pattern and PAR rapid scan. When only the current two WSR-88D radars in the domain are assimilated, PAR shows no or little impact on data assimilation and forecasts.

2. PAR 1 minute VCPs are especially beneficial to rapidly evolving local storms and wind forecasts. Our evaluation on different stages of storm forecasts (not shown here) also indicate PAR is more beneficial to storm initiation stage than mature stage.

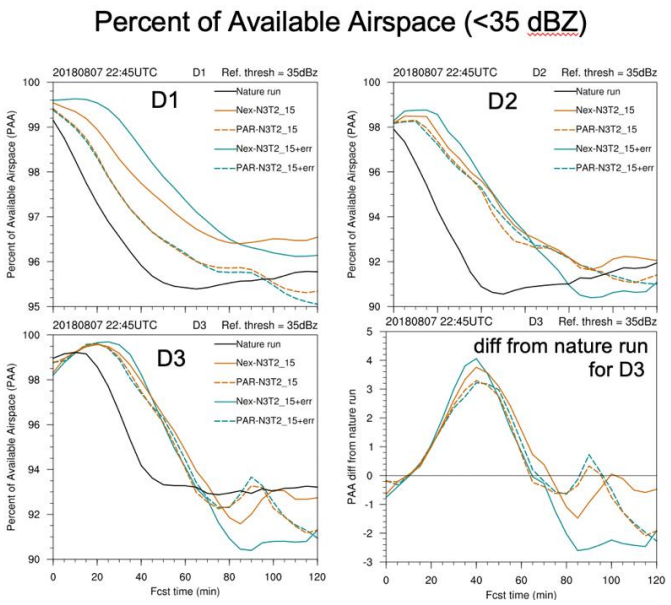

Fig. 2.4.15. Upper row (left for D1 and right for D2) and lower left (D3): DAA curves showing Nature Run (black) and the two experiments without (Nex-N3T2_15 and PAR_N3T2_15) and with (Nex-N3T2_15+err and PAR_N3T2_15+err) observation error. Lower right: The difference of DAA between the Nature Run &

3. The additional low-level (0.2 degree) elevation scan is crucial for wind analyses and forecasts, especially in the small domains (D2 and D3) encompassing the airports.

4. The addition of the TDWR & low level scans to the two Nexrad radars give significant improvement for the NYC airport environment, evaluated by the domain airspace availability. PAR 1 minute VCP yield an additional improvement above the 5 minute VCP.

5. The PAR experiment with the 5 radar hypothetical radar network is less sensitive to realistic simulated observation errors and better capture convective cell initiation and rainfall accumulation than its 5 minute Nexrad counterpart.

Future work

These VDRAS-based OSSE experiments have shown that rapid scan PAR data assimilation offers some improvement in forecast skill over the slower mechanically scanned Nexrad & TDWR radars for this moderate evolving convective case of Aug 7, 2018. However we have not explored all the advantages of the PAR nor explored other important aspects of using PAR for aviation applications, especially for large-scale rapidly evolving convective systems. In future studies we need to investigate the following topics:

1. Additional cases. For severe weather all meteorological conditions are different so it is important to test a wide variety of convective cases to determine what is really important for operational use in aviation. We propose to use additional cases (of which there are many) of scattered & linear storms plus winter storms at NYC and other major airports. These additional test cases may show what measurements or trends at the majority of airports that are important for a PAR network design. More realistic observation errors, composed of both instrumentation error and grid point representativeness error can be used in future experiments.

2. Additional data assimilation systems. Other data assimilation and forecasting systems are available with various advantages & disadvantages over VDRAS. For example, the Weather Research and Forecasting Data Assimilation system (WRFDA) (Barker et al. 2012) is a component of the WRF modeling system. Using more than one data assimilation and forecasting systems enables us to make broader assessment of PAR's benefits. In addition, the WRF data assimilation and forecast system is capable of forecasting the high level en-route flight paths and hence evaluating the PAR benefits on en-route weather forecasting.

3. Aviation metrics. The verification metrics for aviation application can be refined by collaborating with research and operational FAA staff. In our study we have used the Domain Airspace Availability measurement error and detection statistics to estimate the open vs closed airspace in the TCA. Realistically, we would rather make these measurements along the flight corridors rather than the entire airspace.

4. PAR targeted observations (adaptive scanning). One of the biggest advantages of PAR E-scan radars is their ability to rapidly probe evolving areas of convective formations, approaching cells and convergent winds that may pose a hazard to aviation. PAR scans can

rapidly monitor cores of convective cells that may be changing in ways known to create microbursts and other wind hazards. Less critical areas of nearby convection may be less frequently monitored for new cell initiation and existing cell's growth and decay. An important aspect of PAR adaptive scanning is the additional time available to collect low level PBL scans by following the ground horizon to minimize ground clutter and measure the important low level convergent flows that may lead to new initiation.

References

Aksoy, A., D. C. Dowell, and C. Snyder, 2010: A multi-case comparative assessment of the ensemble Kalman filter for assimilation of radar observations. Part II: Short-range ensemble forecasts. *Mon. Wea. Rev.*, **138,** 1273-1292.

Barker, D. M., X.-Y. Huang, Z. Liu, T. Auligné, X. Zhang, S. Rugg, R. Ajjaji, A. Bourgeois, J. Bray, Y. Chen, M. Demirtas, Y.-R. Guo, T. Henderson, W. Huang, H.-C. Lin, J. Michalakes, S. Rizvi, and X. Zhang, 2012: The Weather Research and Forecasting Model's Community Variational/Ensemble Data Assimilation System: WRFDA. Bull. Amer. Meteor. Soc., 93, 831–84.

Caya, A., J. Sun, and C. Snyder, 2005: A comparison between the 4D-Var and the ensemble Kalman filter techniques for radar data assimilation. Mon. Wea. Rev., 133, 3081-3094.

Chang, S.-F., J. Sun, Y.-C. Liou, S.-L. Tai, and C.-Y. Yang, 2013: The influence of erroneous background, beam-blocking and microphysical nonlinearity on the application of a four-dimensional variational Doppler radar data assimilation system for quantitative precipitation forecasts. Met. Apps, 21, 444–458. doi: 10.1002/met.1439.

Sun J., D. Flicker, and D. K. Lilly, 1991: Recovery of three-dimensional wind and temperature from simulated single-Doppler radar data. J. Atmos. Sci., 48, 876-890.

Sun J., and N. A. Crook, 1997: Dynamical & microphysical retrieval from Doppler radar observations using a cloud model and its adjoint: Part I. Model development and simulated data experiments. J. Atmos. Sci., 54, 1642-1661.

Sugimoto, S., N. A. Crook, J. Sun, Q. Xiao, and D. Barker, 2009: Assimilation of Doppler radar data with WRF 3DVAR: Evaluation of its potential benefits to quantitative precipitation forecasting through observing system simulation experiments. Mon. Wea. Rev., 137, 4011-4029.

Wang, H., J. Sun, X. Zhang, X. Huang, and T. Auligne, 2013: Radar data assimilation with WRF-4DVAR: Part I. system development and preliminary testing. Mon. Wea. Rev. 141, 2224-2244.

Xiao, Q., Y.-H. Kuo, J. Sun, W.-C. Lee, E. Lim, Y. Guo, and D. M. Barker, 2005: Assimilation of Doppler radar observations with a regional 3D-Var system: impact of Doppler velocities on forecasts of a heavy rainfall case. J. Appl. Meteor. 44, 768-788.

3. Simulations Assessing Data Quality Characteristics of Phased Array Radar[5]

Introduction

National Weather Service functional requirements for a replacement radar system consist of threshold requirements, which must be met by the replacement radars, and objective requirements, which the replacement radars should try to approach without compromising any threshold requirements (NOAA/NWS 2015). To meet these demanding requirements, any replacement radar system will likely involve tradeoffs between performance and cost, which must be evaluated in a manner that can lead to a preferred solution. For example, conventional radar technology (e.g., a dish-antenna system) can meet most of the threshold requirements but would have difficulties in meeting the objective one-minute-or-less volume update-time requirement. On the other hand, a four-face phased-array radar (PAR) could achieve the desired volume update time but would require a more expensive aperture to meet the angular resolution requirements. Additionally, complex calibration would be needed to ensure that the quality of the polarimetric data from a phased-array system is comparable to that of the WSR-88D (Lei et. al 2015). Radar data quality, which impacts the decisions and products generated by radar data users, is a major aspect of system performance that will be involved in the tradeoffs with system cost. Therefore, to properly balance system cost and performance, it is important for decision makers to understand the impacts of changing radar data quality on end users. Since the NWS forecasters use radar data as a primary source of information in their threat assessment and warning decisions, they are likely to be impacted by data quality changes. This work is a first step to characterize the relationships between data quality changes and their impacts on forecasters.

Studying the impacts of data quality changes on forecasters requires both a process to produce radar data with different data quality and a method to quantify the data quality impacts. One way to produce radar data with different data quality for the same weather event is to build prototypes of different radar designs and collect data at the same time. However, this approach is expensive and impractical. A more practical way to produce radar data with different data quality for the same weather event is through realistic simulations. The Signal Processing and Radar Characteristic (SPARC) simulator offers a flexible framework for studying the impact of signal processing techniques and radar system characteristics on radar-variable estimates required to support the NWS weather-surveillance mission (Schvartzman and Curtis 2019). It is a versatile two-dimensional weather-radar time-series scenario simulator that ingests archived fields of spectral moments and polarimetric variables (also referred to as base data) and produces time-series (I/Q) data, which can be processed to produce base data as it would be observed by different radar systems. In contrast with other simulators, the SPARC simulator allows for an end-to-end evaluation that considers the interactions between radar sub-systems (e.g., the transmitter, the antenna, the receiver), scanning strategies (e.g., the pulse repetition time, the

[5] Principal Investigators: Feng Nai, Jami Boettcher, David Schvartzman, Chris Curtis and Sebastian Torres (CIMMS)

number of samples per dwell), and the signal processing. This makes the SPARC simulator a suitable tool to simulate data with different degrees of quality.

Simulated radar data with varying quality must be analyzed and compared in a systematic way to quantify the impacts on forecasters. The statistical biases and variances of the radar-variable estimates can be used to quantify the data quality changes, but they are not enough to completely characterize the impact on forecasters. For example, the spatial distribution of biases could matter more than the magnitude of the biases when a forecaster is assessing the potential threat of a storm. To account for data quality changes that affect forecasters' interpretation of the radar data, our evaluations of the data quality impacts are based on the preservation or presentation of important weather features in the data. We developed scoring systems to quantify the amount of data quality impacts for scenarios in which the data quality changes were progressive. Alternatively, we used comparative analysis to determine the better data set for scenarios in which the data quality changes were subtle. While any data quality change will also impact algorithms that use those data, these impacts are outside the scope of this work and should be investigated in future studies.

In this study, we used the SPARC simulator to simulate data from radar systems with different spatial resolution, azimuthal sampling, and/or sensitivity. The different radar characteristics (e.g., varying beamwidth and sidelobe levels) and scan strategies (e.g., varying azimuthal sampling) used in this study were selected to correspond to potential tradeoffs associated with a PAR, which is a promising candidate to replace the WSR-88D. The simulated data were analyzed by one of the investigators (Boettcher), who has over 20 years of experience training NWS forecasters as well as 10 years of operational forecasting experience. Her vast experience in interacting with a variety of NWS forecasters (from novices to experts) makes her uniquely qualified as a representative for the broader NWS forecaster population. To support her goal of seeing the data through the eyes of a broad population of NWS forecasters, she had numerous discussions with operational forecasters throughout data collection and analysis. Based on our results, we characterized the relationship between any degradations to the spatial resolution, azimuthal sampling, and/or sensitivity of the radar system and their impacts on forecasters. Our conclusions can be used by decision makers to evaluate future radar designs in the context of tradeoffs between system performance and cost.

Owing to its length, the full report on our data quality analysis is provided as a separate document. This covers in detail the impacts of changing the radar's spatial resolution (beamwidth and sidelobe levels), azimuthal sampling grid and sensitivity (i.e., average power, antenna gain, integration time). Methods and results are summarized in the sections below.

3.1 Impact of Antenna Sidelobes and Beamwidth

To understand the relationship between sidelobe levels and impact on forecasters, we simulated radar data for the same weather event as though it was observed by radar systems with different sidelobe levels. The change in integrated sidelobe level relative to the WSR-88D antenna pattern

(ΔISL) was used to quantify the overall sidelobe levels for 11 specific antenna patterns. We analyzed 12 storm cases and scored the simulated data (on a scale of 1=fully acceptable to 5=unacceptable) based on the amount of "distractions" to forecasters caused by sidelobe associated compromised data. That is, noisy velocities and/or false circulation signatures at lower elevation angles. Figure 3.1.1 shows these data quality scores for the separate storm cases as a function of the antenna pattern ΔISL.

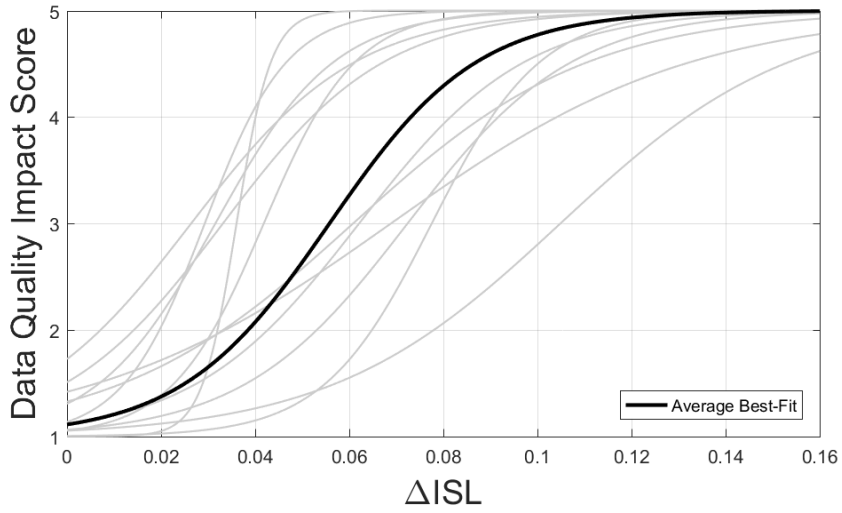

Fig. 3.1.1. Fitted Data Quality Impact Score versus ΔISL *for all 12 non-outlier storm cases, and the average best-fit curve (black line). The x-axes is ΔISL in linear units, which increases with larger (less acceptable) sidelobe levels.*

The impact model depicted in Figure 3.1.2 relates changes to sidelobe levels to impacts on NWS forecasters and can be used by decision makers to evaluate future radar designs and proposed sidelobe requirements. The impact model is a function of the reflectivity gradients in the storm under analysis. For the "upper bound" cases that we chose, the reflectivity gradients are close to the maximum that the WSR-88D can observe without producing compromised data.

Such an impact model could be used by decision makers in two ways. The first use is to estimate the consequences of sidelobe degradation for a given radar design. The second use is to evaluate the robustness of a given design to storms more demanding than the "upper bound" storm. To use the impact model for these applications, we would first need to convert the x-axis into the absolute ISL, which is usually inversely related to system cost. With this conversion of the x axis, any potential radar design could be placed directly on it using its absolute ISL. Moreover, we would also need to shift the model curve on the x axis to match the required "upper bound" storm. The refinement of such decision-making applications of our model is ongoing.

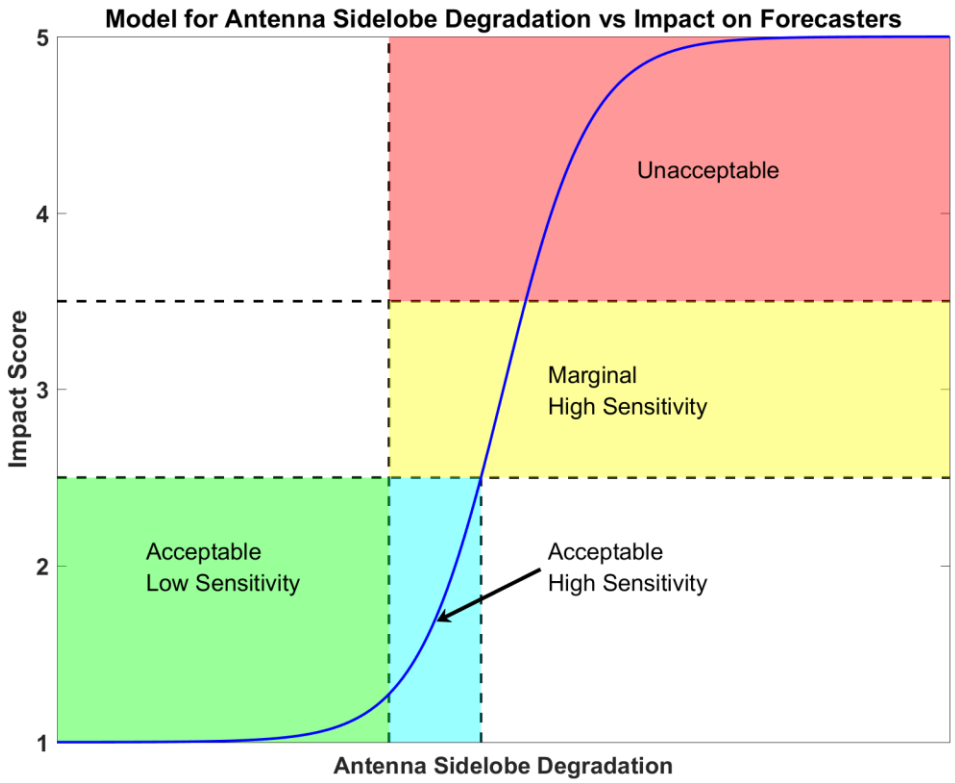

Fig. 3.1.2. Model for the relationship between relative sidelobe degradation and impact on forecasters. Based on the impact score, there are three regions: acceptable, marginal, and unacceptable. Within the acceptable region, the model curve falls in two separate regions: low sensitivity and high sensitivity. Sensitivity describes how quickly the impact score changes when the relative antenna sidelobe degradation changes.

To evaluate the impacts of PAR scan-dependent beam broadening on forecasters, we simulated a scaled PAR with a beamwidth that varies between 1° and 1.4° and two reference systems with a constant beamwidth (CB) of 1° and 1.4°, respectively. By simulating different types of weather with weather features of interest located at different locations with respect to the array, we showed that the beam broadening effect does not cause any artifacts in the data that would have negatively impact forecasters' interpretation of radar data. Moreover, for a large majority of non-circulation cases, all three systems performed similarly. For circulation cases, the scaled PAR performs better than the CB-1.4° system, implying that a full-size PAR could perform better than the WSR-88D assuming other aspects of the radar (e.g., sidelobe levels, sensitivity, etc.) are identical. Lastly, comparisons between the scaled PAR and the CB-1.0° system show that the scaled PAR system is worse only when the weather feature is located close to ±45° from the broadside of the array. For a PAR with four stationary faces, these results show that the current beamwidth requirements (i.e., beamwidth ≤ 1° for all scanning angles) must be satisfied to prevent negative impacts on forecasters since the location of the weather feature with respect to

array broadside cannot be controlled. However, for a PAR with rotating faces and limited electronic steering in azimuth (i.e., electronically steer the beam to scan only within ±22.5° of the broadside), our results suggest that it may be possible to relax the beamwidth component of the angular resolution requirement to reduce the system cost. That is, a rotating PAR with a beamwidth of 1° at broadside that only electronically steers within ±22.5° can perform similarly to the WSR-88D.

3.2 Impact of Azimuthal Sampling

Phased array radar facilitates sampling of meteorological echoes at smaller azimuthal sampling intervals than can be practically achieved using a mechanically scanned reflector antenna. For example, digitally formed simultaneous receive beams can be spaced at sampling intervals smaller than the antenna beamwidth, thus effectively "oversampling" in azimuth (or elevation).

We investigated the potential impacts of changing the azimuthal sampling grid on forecasters. We compared simulated data from a scaled PAR for the same weather event collected with three different azimuthal sampling grids. Two grids had uniform azimuthal sampling interval (0.5° and 0.7°) while the third grid had an azimuthal sampling interval that varied from 0.5° to 0.7° as the radar scanned from broadside of the array to ±45°. This sampling grid with variable azimuthal sampling interval is referred to as sine-space sampling and is a natural sampling grid for a PAR that has varying beamwidth. For non-circulation cases, we found that a denser sampling grid is always preferred. For circulation cases, the preferred sampling grid is case dependent. In all the cases analyzed, using sine-space sampling does not cause any artifacts in the radar data that can negatively impact forecasters' data interpretation and threat assessment.

To further study the azimuthal sampling effects on radar observations of circulations, we used a simplified model to quantify the performance of different sampling grids. Storm circulation observations were grouped according to their beamwidth-to-apparent-diameter ratio (BADR), where the apparent diameter (AD) is defined as the distance between the extrema of the radar-observed velocity profile before sampling. Our simulation results showed that decreasing the azimuthal sampling interval leads to a reduction in the underestimation of the V_{rot} for all BADRs.

Our simulations also showed that, for all BADRs, grids with a 0.125° (0.25°) azimuthal sampling interval result in radar-observed circulation strengths that are within 99% (95%) of their theoretical maxima. Moreover, decreasing the azimuthal sampling interval also reduces the impacts of azimuthal sampling for all BADRs. That is, the difference between the best and the worst radar-observed circulation strengths among all sampling-grid relative positions decreases as the azimuthal sampling interval gets smaller.

To corroborate our simulation results, we processed time-series data for two circulations and produced velocity fields corresponding to different sampling grids. The variation of V_{rot} as a function of azimuth shift for different sampling grids showed the same features as the simulation results. That is, higher and more consistent radar-observed circulation strengths were measured

when using sampling grids with smaller azimuthal sampling interval. Results from simulations and real data also showed that the improvements get progressively smaller as the azimuthal sampling interval decreases, which implies that the majority of the benefits can be realized without using the finest possible sampling grid.

3.3 Impact of Radar Sensitivity

In this study, we focused on the impact of sensitivity changes on forecasters. We simulated data for the same weather event as collected by radar systems with progressively lower sensitivity by adding white noise to simulated weather data while keeping all other radar characteristics constant. For each case, we varied the sensitivity of the simulated radar system from matching that of the WSR-88D to 20 dB lower. The simulated data were analyzed and a Data Quality Impact Score was assigned. Analogously to the assessment described in section 3.1, the scoring system was based on the amount of erosion of the footprint of the storm and key weather features.

Using the scores, we fit sigmoidal curves for each weather case and developed an average best-fit that captures the relationship between sensitivity loss and impact on forecasters (Figure 3.3.1). An extension of this approach to include a larger number of cases and greater diversity of events can be used to generate a more robust impact curve. This impact curve can be used by decision makers to evaluate future radar designs by directly comparing the sensitivity of the proposed system to the sensitivity of the WSR-88D.

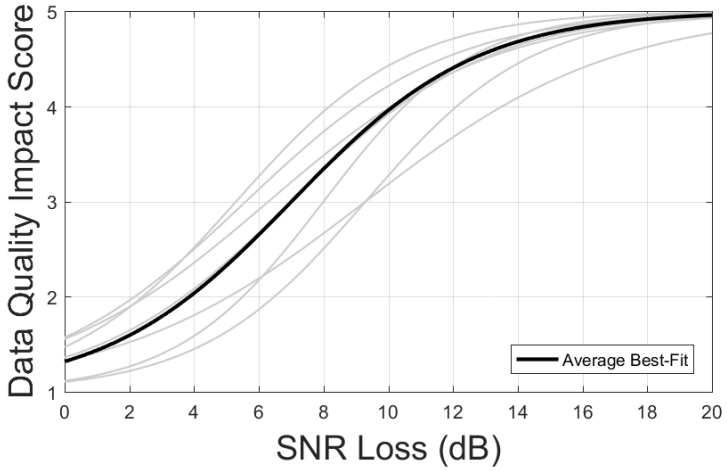

Fig. 3.3.1. Fitted Data Quality Impact Score versus SNR loss for all 12 6 storm cases, and the average best-fit curve (black line). The x-axes are SNR loss in dB units. Note that the curve fitting minimizes the mean squared error and captures the trend of the scores. The average best-fit curve uses parameters that are the average of all cases.

4. Simulations Assessing Phased Array Radar Scanning Strategies ("Command and Control")[6]

Introduction

In order to improve the capabilities of the current parabolic-reflector-based WSR-88D network and to achieve the current and future needs to support the National Weather Service (NWS) mission, evolutionary concepts of operations (ConOps) for weather surveillance using different radar systems to meet threshold functional requirements have to be developed. One way to meet functional requirements is to exploit Phased Array Radar (PAR) technology by performing adaptive scanning. By means of adaptive techniques, the radar can dynamically modify the scan to observe regions with significant meteorological echoes and provide the users (i.e., forecasters and automatic algorithms) the information they need, when they need it, to make critical decisions. For example, isolated tornadic supercell storms can have a relatively narrow azimuthal extent, which can be frequently scanned with the agile electronic beam of a PAR system to provide rapid updates for this fast evolving hazardous storm. However, designing and testing adaptive scanning algorithms is not a trivial task. In addition to quantifying impacts of different scan strategies and trading off radar resources in real-time, adaptive scanning algorithms have to maintain good performance across different precipitation systems (e.g., stratiform or convective systems). An objective and robust way to design and evaluate adaptive scanning techniques requires an emulator capable of producing radar data as it would be seen by different radar systems and of using arbitrary adaptive scanning techniques.

A Command and Control (CC) simulator that produces realistic time-series dual-polarization weather radar data as would be seen by different types of radars was developed to study candidate radar architectures operating with a variety of adaptive scanning techniques. The core of the command and control simulator is the module that produces simulated time-series data for a single time step using a scan definition passed as input. It is based on the Signal Processing and Radar Characteristics (SPARC) simulator, a versatile two-dimensional weather-radar time-series scenario simulator able to ingest archived dual-polarization data and produce time-series data as it would be observed by a given radar system. The CC offers a flexible framework for studying the impact of signal processing techniques and radar system characteristics on radar-variable estimates required to support the NOAA-NWS weather-surveillance mission. After processing the simulator output using conventional weather-radar signal-processing techniques, apples-to-apples analyses can be carried out to evaluate the impacts of the simulated radar on the coverage, timeliness, and quality of the data.

The CC simulator consists of a system-level simulation framework designed to account for the combined effects of the radar system coupled with adaptive scan strategies that modify the scan to be executed in the subsequent simulation time-step. In contrast with other simulators, the CC

[6] Principal Investigators: Sebastian Torres and David Schvartzman (CIMMS)

simulator allows for an end-to-end evaluation that considers the interactions between radar sub-systems (e.g., the antenna), the scanning strategy (e.g., PRT, number of samples), and the signal processing techniques. By ingesting and pre-conditioning archived radar data, it allows the user to produce realistic fields of simulated radar variables from a vast selection of weather events observed by WSR-88D radars. This data has radar sampling artifacts, some of which are mitigated by the data conditioning function. Regardless of these artifacts, researchers should compare the simulated data to the ground truth data that comes out after data conditioning. It is worth noting that radar-variable fields from other radars or another source (e.g., model data) could also be ingested to overcome contamination and practical limitations found in real radar data. This makes the CC a suitable framework to study and better understand the implications of adopting different technologies (e.g., phased-array antennas) based on the requirements provided by the NWS for the Weather Surveillance mission. High-level block diagrams of the CC framework and the SPARC simulator are presented in Figs. 4.1 and 4.2.

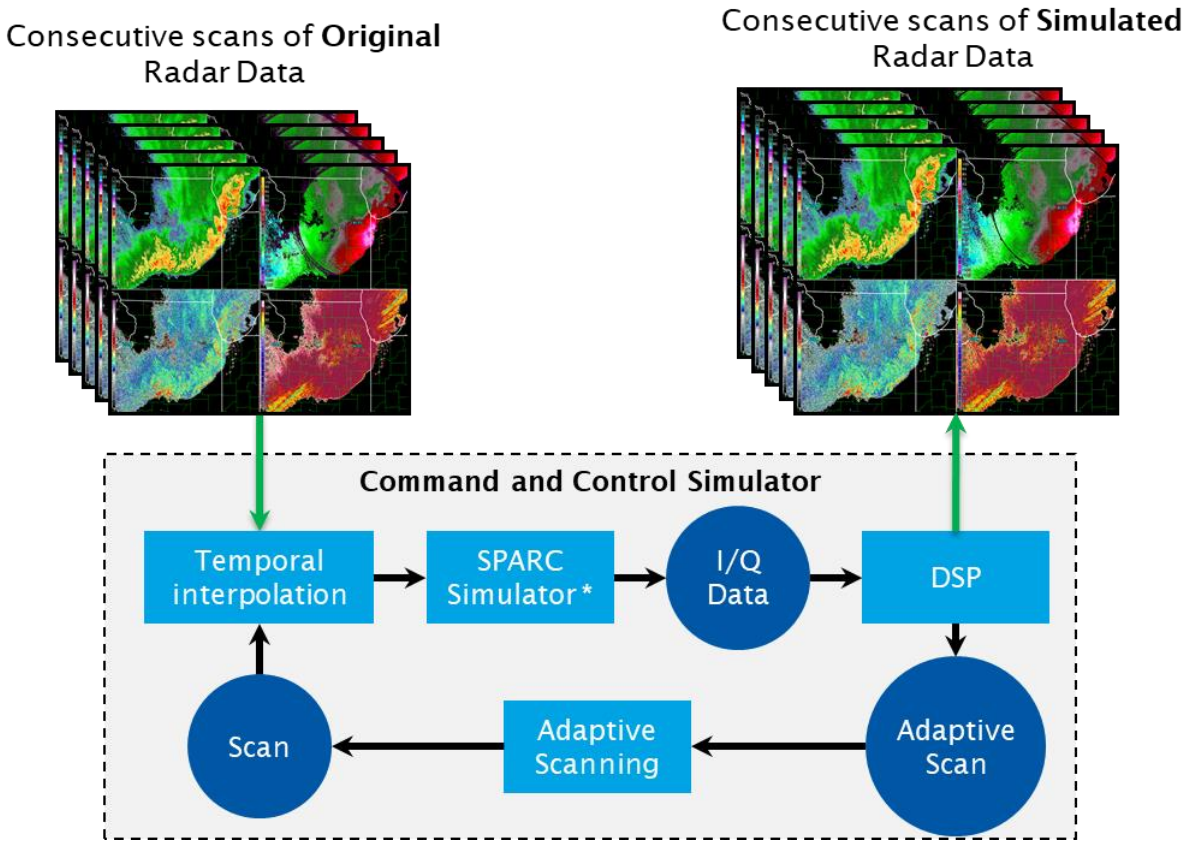

Figure 4.1. High-level block diagram of the Command and Control simulation loop. After a case is selected for simulation, base radar data from the WSR-88D are ingested into the simulator. A data conditioning and temporal interpolation step prepares the data for simulation. The SPARC simulator produces time-series signals that incorporate radar sampling and signal processing effects on the data. Data are then processed by the Digital Signal Processor (DSP) and passed to the adaptive scanning algorithms to redefine the following scan. The produced adaptive scan restarts the CC loop, which continues producing volumes of radar data as it would be seen by the

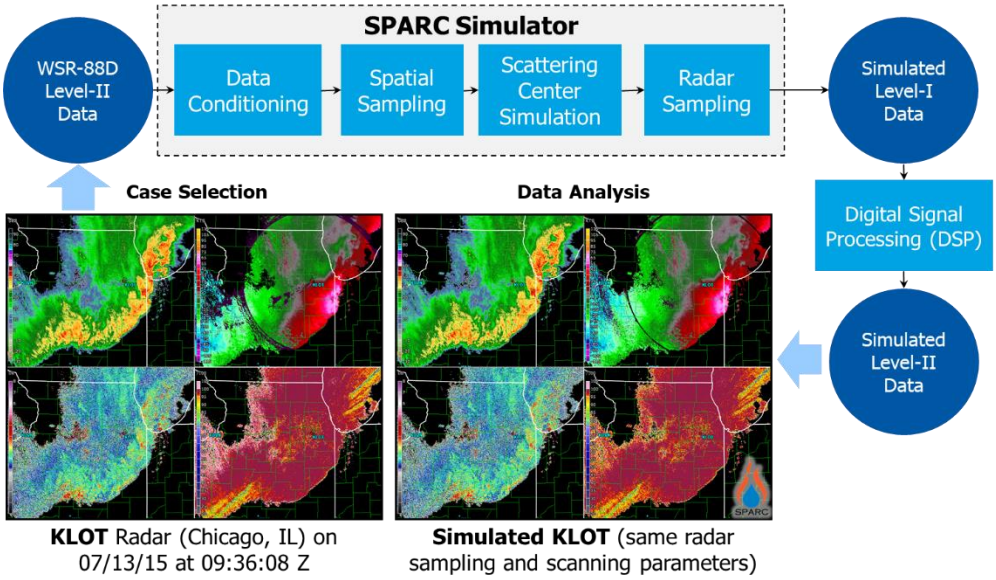

Figure 4.2. Simplified block diagram of the SPARC simulator. The images to the left represent the input data to the simulator which are processed sequentially as indicated in the blocks of the diagram. Six radar variables are ingested into the SPARC simulator: reflectivity (Z_h), radial velocity (v_r), spectrum width (σ_v), differential reflectivity (Z_{DR}), differential phase (Φ_{DP}), and co-polar correlation coefficient (ρ_{hv}). After signal processing of the simulated time-series data, we get the simulated radar-variable estimates as would be observed by the desired radar system. The simulated output fields are on the right image.

4.1 Radar Architectures

The CC framework allows researchers to emulate different types of radar architectures (conventional parabolic-reflector radars, single-face PAR, and 4-face PAR), and their associated sampling characteristics (e.g., antenna patterns, waveforms, pulse-repetition times, number of samples, etc.). These are illustrated in Fig. 4.3. It is important to consider the performance of different architectures in terms of meeting the functional requirements and to allow the framework to change the scan sampling parameters dynamically as dictated by the adaptive scanning algorithms.

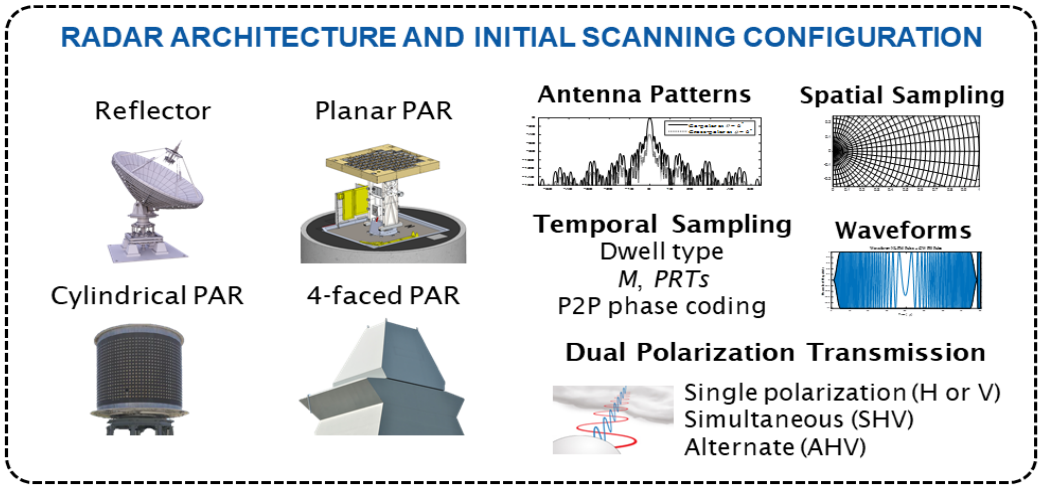

Figure 4.3. The CC framework allows users to emulate different radar architectures and scan strategies.

Data conditioning and Temporal Interpolation

Using archived WSR-88D data available from the National Centers for Environmental Information (NCEI) gives users the possibility to simulate a variety of weather events. Through this vast collection of archived weather events, the user can choose to simulate different types of weather (e.g., convective or winter storms, stratiform precipitation), as would be observed by a user-specified radar system. However, archived data are typically stored after being processed by several signal processing techniques, which might result in several range gates being filtered, censored, or simply marked as containing unresolved overlaid echoes. In addition to the radar artifacts mentioned, archived data have a pre-defined sampling grid on which radar variables are produced. In the case of the WSR-88D, using super-resolution azimuthal sampling and a PRT on the order of 3 ms, the sampling grid (at the lowest elevation angle of 0.5 deg) has 720 azimuth positions and approximately 1800 range locations. However, the intended simulation could require a different sampling grid, or a scan time that is not available within the time resolution of the WSR-88D (approximately 5 minutes).

The data conditioning function performs a two-dimensional interpolation of the radar variables to match the desired sampling characteristics, it de-aliases the radial velocity field, and it fills in range locations with missing or censored data. Furthermore, we developed and integrated a temporal interpolation routine that uses adjacent scans (from NCEI) to produce a new ‘scan’ collected at an arbitrary time between the NCEI inputs. While this temporal interpolation routine may not be suitable for a meteorological study to show the benefits of rapid updates (given that it does not produce new information), it is sufficient for the purposes of evaluating adaptive scanning techniques and producing realistic fields of adaptively scanned radar variables.

Adaptive Scanning Techniques

The versatile scan definition in the CC framework allows users to design and integrate arbitrary adaptive scanning techniques that modify the scan on each cycle of the simulation loop to produce data as would be observed using the defined radar architecture and adaptive scanning

methods. Three adaptive scanning algorithms were developed and implemented within the CC framework with the goal of reducing the scan update times. The ConOps utilizes both a fast surveillance and an adaptive weather scan. The surveillance scan is executed first and it informs the adaptive scanning function that produces the adaptive weather scan. The frequency of each scan in the scan table is determined by either a number of repetitions or a timer. Once the repetitions are reached or the timer expires, the simulator executes the next scan in the table.

The algorithms implemented include the Adaptive Digital Signal Processing Algorithm for PAR Timely Scans (ADAPTS) algorithm, a beam clustering algorithm that selects a variable transmit beam spoil factor based on the reflectivity gradients observed, and an adaptive dwell determination technique that selects the number of pulse-repetition times (PRTs) and samples to be used at a particular beam position. ADAPTS selects significant beam positions to be scanned based on the significance and continuity of the weather echoes. The requirement-driven beam-clustering algorithm determines the spoiling factor (e.g., 1, 3, 5) based on the reflectivity bias of the cluster computed on the fly. The adaptive dwell determination technique is capable of reducing a multi-PRT dwell to a dual- or single-PRT dwell when no echoes beyond the maximum unambiguous range of the shorter PRT(s) are found. The integration of these techniques is not trivial, and we made reasonable considerations in the context of a real ConOps for each technique. For example, if one beam in a cluster is determined to be "significant" by ADAPTS, then the whole cluster is scheduled to be scanned (and thus, more beams can be received for a single dwell period). Otherwise, if all receive beams are "non-significant," the whole cluster is disabled and therefore not executed in the subsequent simulation. Illustrative examples of these techniques are presented in Fig. 4.4.

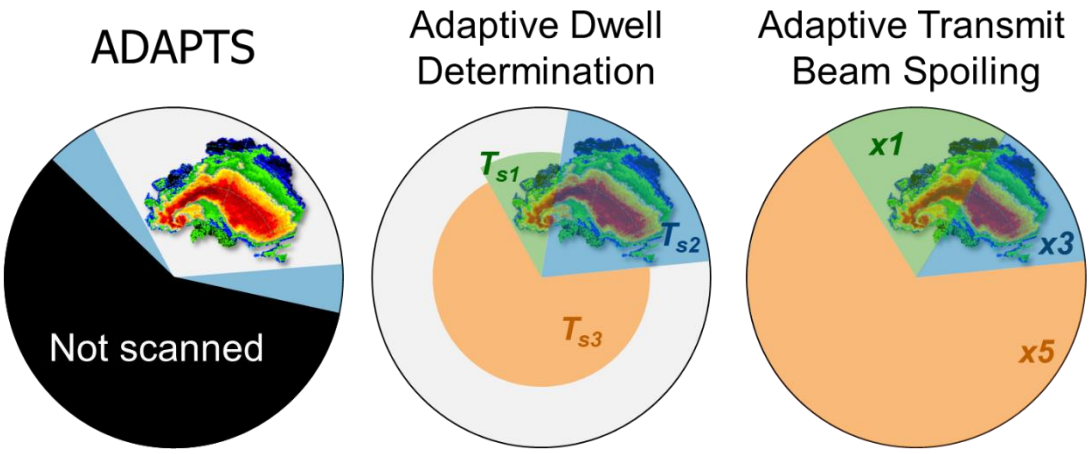

Figure 4.4. Adaptive scanning techniques implemented into the CC framework to demonstrate its capabilities to produce realistic simulations using diverse Concept of Operations.

Simulated Radar Data

Using the ConOps mentioned previously, namely, fast surveillance scan followed by adaptive weather scan, we simulated several weather events. For these simulations, we adopted a 4-faced

PAR (also referred to as MPAR) architecture as shown in Fig. 4.5. The fast surveillance scan uses a uniform PRT with a short dwell time (low number of pulses), a full coverage strategy with azimuthal sampling of one beamwidth (i.e., no super-resolution), and no beam spoiling (i.e., scans using a "pencil" beam). The data produced by this scan are not intended to be displayed to the users but rather to be consumed by adaptive scanning algorithms to produce a high-quality adaptive weather scan. This surveillance scan takes approximately 4 seconds. Even though the data quality associated with this surveillance scan is relatively low, it provides enough information to drive the adaptive scanning techniques that define the adaptive weather scan. The focused weather scan incorporates adaptive techniques that reduce the scan time while meeting data quality and spatial resolution requirements. As mentioned previously, the frequency of each scan in the scan table is determined by either a number of repetitions or a timer and, based on this definition, a round-robin scheduler cycles through the scans in the table. An illustration of this ConOps is shown in Figure 4.6, where the surveillance scan is executed once. Based on the information obtained, the adaptive weather scan determined is subsequently executed twice. These scheduling parameters are arbitrary and can be set to any desired configuration for simulation.

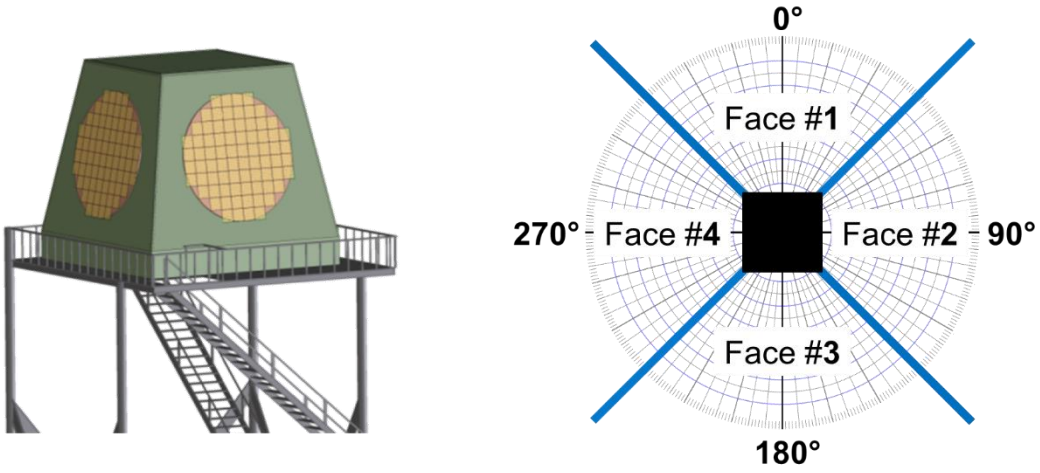

Figure 4.5. Full 4-faced MPAR architecture adopted to demonstrate the CC framework developed.

After implementing and integrating the mentioned adaptive scanning techniques into the CC framework, we simulated several weather events using each technique individually and using all of them together. These techniques have strengths and limitations in terms of the resulting scans, but their careful and informed integration results in approaching the objective scan-time requirements without sacrificing data quality or spatial coverage of significant weather echoes. Examples of the simulated cases are presented next. (1) The deterministic full resolution weather scan (i.e., similar to WSR-88D) is shown in Fig. 4.7; (2) the adaptive scan using the ADAPTS technique is shown in the top panel of Fig. 4.8; (3) the adaptive scan using adaptive beam

clustering is shown in the center panel of Fig. 4.8; (4) the adaptive scan using adaptive dwell determination is shown in the bottom panel of Fig. 4.8; and (5) the adaptive scan with all adaptive techniques combined is in Fig. 4.9. These simulations show the flexibility and potential of the CC framework to study the impacts of adaptive scanning algorithms on data quality, update times, and spatial sampling.

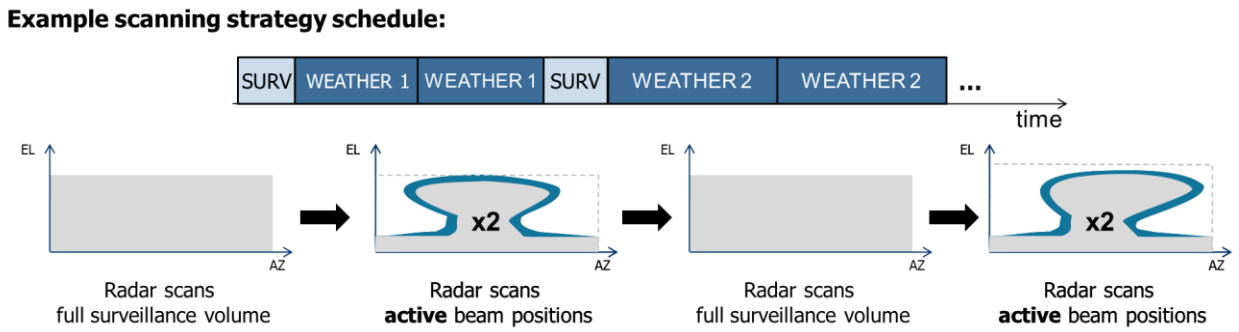

Figure 4.6. Example of the implemented Fast Surveillance + Adaptive Weather ConOps.

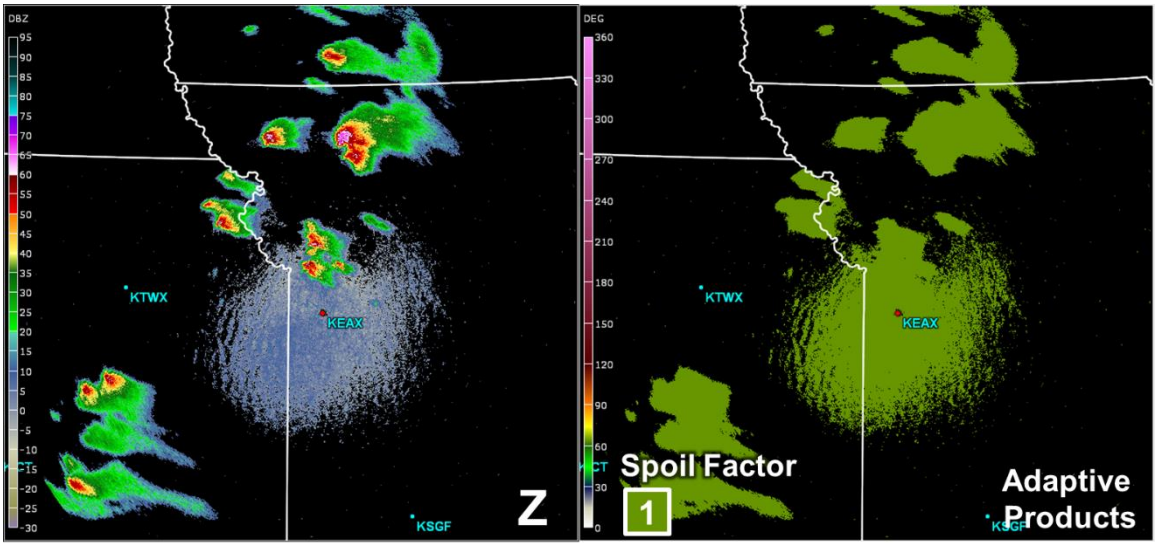

Figure 4.7. Deterministic full resolution weather scan (i.e., similar to WSR-88D). The left panel shows the simulated radar reflectivity, and the right panel shows the adaptive products (all "pencil" transmit beams in this case).

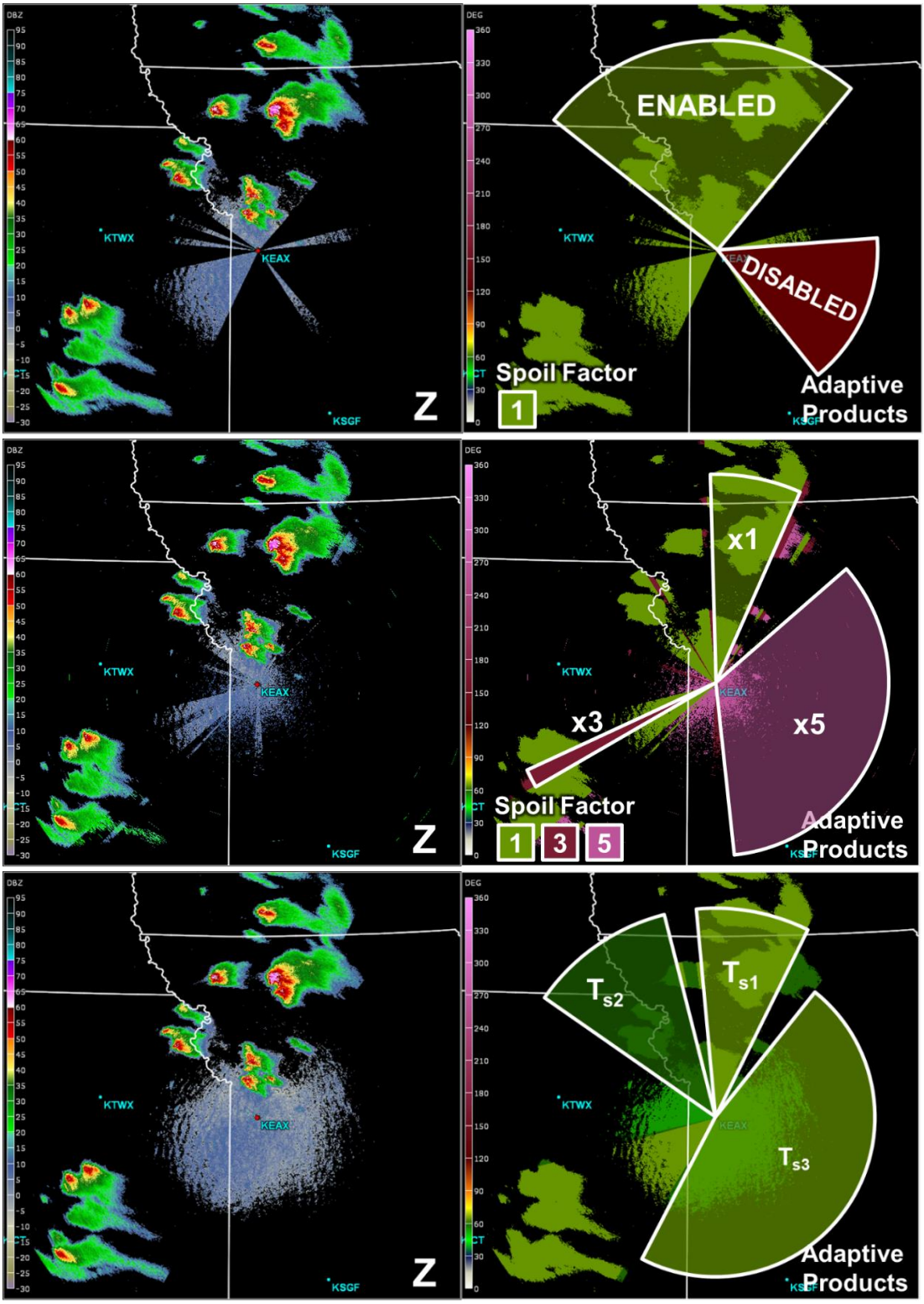

Figure 4.8. Adaptive scanning techniques implemented in the CC framework: (top) adaptive scan using the ADAPTS technique, (center) adaptive scan using adaptive beam clustering, (bottom) adaptive scan using adaptive dwell determination.

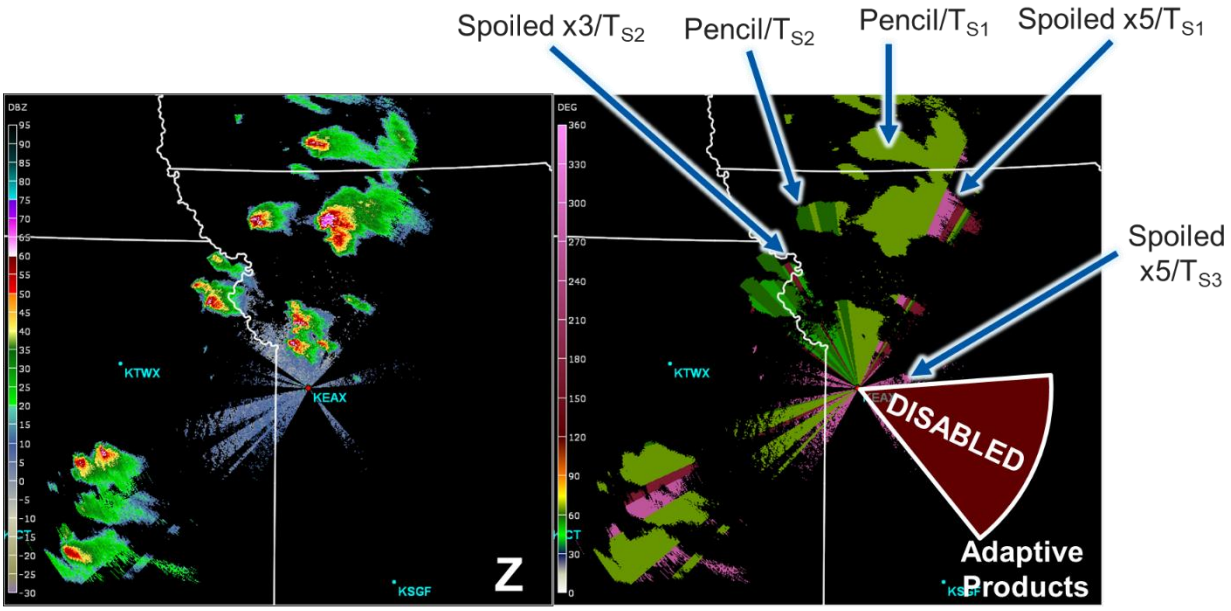

Figure 4.9. All adaptive scanning techniques implemented in the CC framework used simultaneously to produce high quality weather scans that attempt to meet the temporal resolution requirement without sacrificing data quality.

Finally, to quantify the time reduction of each technique individually and the reduction when using all techniques simultaneously, we computed the update times on each of the four PAR faces as a function of time. These are presented in Fig. 4.10. It is clear from the results that each technique individually contributes to reducing the scan times and that the fastest updates (i.e., shortest scan times) are obtained when using all techniques together.

Summary

The Command and Control framework developed in the context of the SENSR program provides the ideal tool for the design, development, and testing of adaptive scanning techniques. Developing adaptive scanning techniques is a long-standing challenge given that it is difficult to objectively quantify their performance for the same weather event and also to quantify the performance of one of the techniques across different types of weather events. With this framework, fair comparisons can be carried out in a systematic way to quantify their performance and the degree to which functional radar requirements are being met. In conjunction with results from the Data Quality study, the CC framework could be used to explore adaptive scanning techniques under different concepts of operations and for several radar architectures.

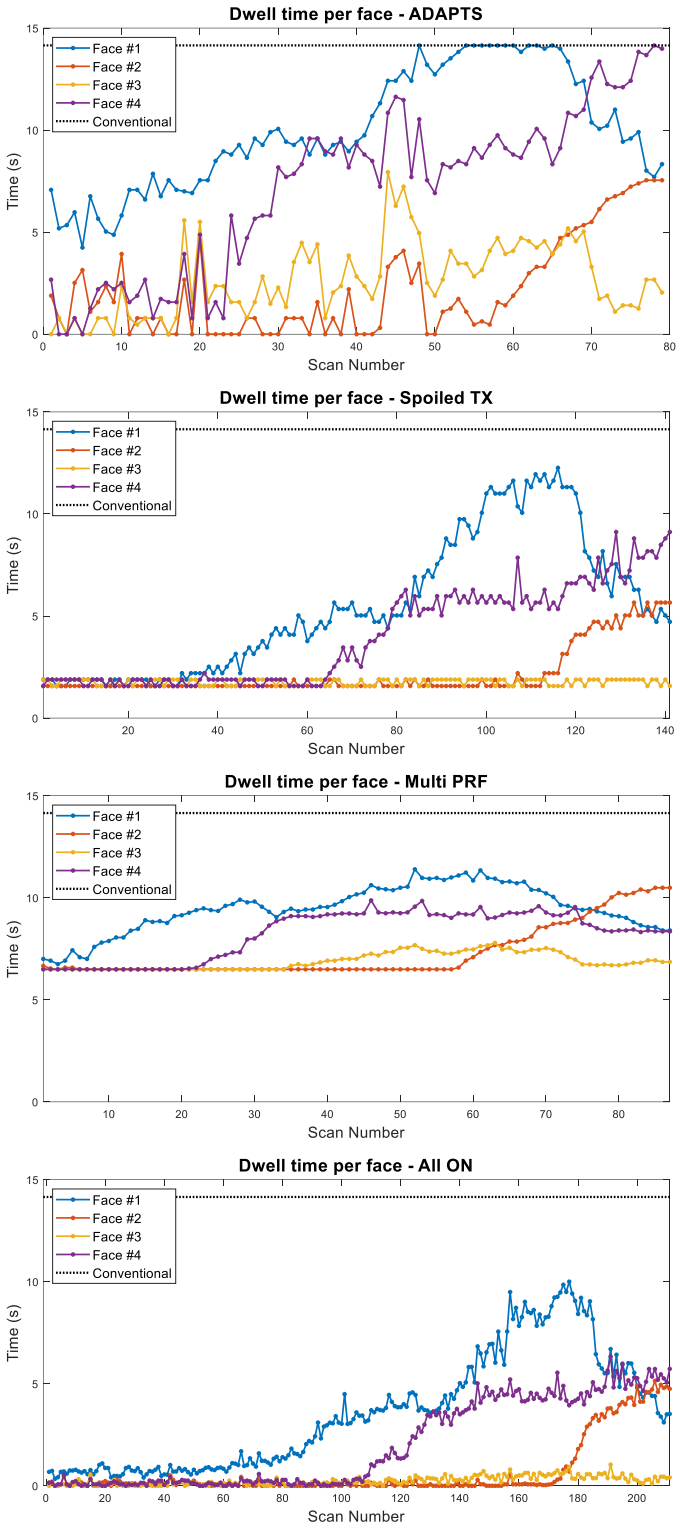

Figure 4.10. Scan times as a function of scan number using the adaptive scanning techniques developed and integrated into the CC framework.

5. Radar Network Benefit Monetization Studies[7]

In planning for a future operational weather radar network, monetization of their benefits is needed to assess the trade-off between more-expensive options (higher performance and/or coverage) and the benefits provided. Meteorological radar's most direct impacts are made through the detailed and continuously updated depiction of hazardous weather for real-time decision making. Sometimes these decisions are life or death matters. In the last thirty years (1989-2018), the top three weather-related fatality causes in the U.S. were excessive heat, floods, and tornadoes. The National Weather Service (NWS) issues warnings for these phenomena, and weather radar data plays a crucial role for tornadoes and flash floods. Thus, we focused on these two hazards in quantifying the benefits that meteorological radars provide to society.

For these studies, we hypothesized that better radar coverage/performance improves warning performance, which, in turn, reduces casualties. To characterize radar coverage, we employed a fraction of vertical space observed (FVO) metric, which integrates the effects of the Earth's curvature, terrain blockage, and the radar's overhead "cone of silence" due to its limited elevation scanning angle. As the key radar performance characterization, we used the cross-radial horizontal resolution (CHR) as a metric. For tornadoes, we also included volume scan update rate, because the phased array radar innovative sensing experiments (PARISE) allowed us to model the dependence of tornado warning performance on update rate. Statistical regression analyses on many years of historical data proved our hypothesis to be true for both tornadoes and flash floods. Subsequently, radar network geospatial benefit models for both phenomena were developed based on these statistical relationships, and benefit estimates were computed for different network configurations.

A fine-resolution (1/120° × 1/120°) latitude-longitude contiguous United States (CONUS) grid was used for all model development and usage computations. Fatalities were monetized according to the Department of Transportation's value of statistical life (VSL), which was $11.6M in 2019 dollars. Injuries were valued as fractions of VSL at $3.1M (hospitalized) and $0.55M (treated and released).

Details of model development and results are documented in the following publications:

- Cho, J. Y. N., and J. M. Kurdzo, 2019: Monetized weather radar network benefits for tornado cost reduction. Project Rep. NOAA-35, MIT Lincoln Laboratory, 88 pp., https://www.ll.mit.edu/sites/default/files/publication/doc/monetized-weather-radar-network-benefits-cho-noaa-35.pdf.

- Cho, J. Y. N., and J. M. Kurdzo, 2019: Weather radar network benefit model for tornadoes. *J. Appl. Meteor. Climatol.*, **58**, 971–987, https://doi.org/10.1175/JAMC-D-18-0205.1.

[7] Principal Investigators: John Cho and James Kurdzo (MIT LL)

- Cho, J. Y. N., and J. M. Kurdzo, 2020: Weather radar network benefit model for flash flood casualty reduction. *J. Appl. Meteor. Climatol.*, under review.

Below, we provide brief synopses of the tornado and flash flood analyses.

Tornadoes

Using 21 years (1998-2018) of data, we were able to establish in a statistically robust way that better radar coverage/performance (as measured by FVO and CHR) improves tornado warning performance (detection probability and false alarm ratio). We augmented these dependencies with the results from PARISE that showed rapid-scan (one-minute volume update period) radar data leading to enhanced tornado warning performance (detection probability, false alarm ratio, and lead time), relative to a volumetric update period of four minutes, which is more typical of today's radars. In combination, these relationships allowed us to generate geospatial maps of estimated tornado warning performance for a given weather radar network configuration.

Next, we were able to show that tornado casualty rate was meaningfully dependent on population inside the tornado path, tornado surface dissipation energy, fraction of population residing in mobile housing, local historical false alarm ratio, and warning lead time. The resulting regression model could then be used to generate casualty rate estimates on a geospatial grid, given the outputs of the tornado warning performance model, population, tornado occurrence rate (parsed by Enhanced Fujita [EF] number), and mobile housing statistics. In addition to casualty cost, we also estimated the cost of time lost by people taking shelter on false tornado warnings, since we saw that false alarm rates could be reduced by better radar coverage/performance.

The tornado benefit model was run on the existing CONUS weather radar network as well as on hypothetical configurations. For the current case, in addition to the WSR-88D, we included the Terminal Doppler Weather Radar (TDWR) in response to a survey that we conducted showing that NWS forecasters rely heavily on TDWR data (where available) in making tornado warning decisions. Key results were as follows (values are given in 2019 dollars):

- Current weather radars provide a tornado-based benefit of $535M per year.
- The remaining benefit pool is $676M per year (see Figure 5.1 for geospatial distribution).
- About half of the benefit pool ($333M per year) can be claimed by upgrading the current radars with rapid-scan (one-minute volume coverage update) capability.
- Over 99% of the current tornado-related benefit is realized east of the Rockies.
- The highest single-site gap-filling benefit exists in northern Alabama and is about $4M per year ($7M per year with rapid-scan capability).

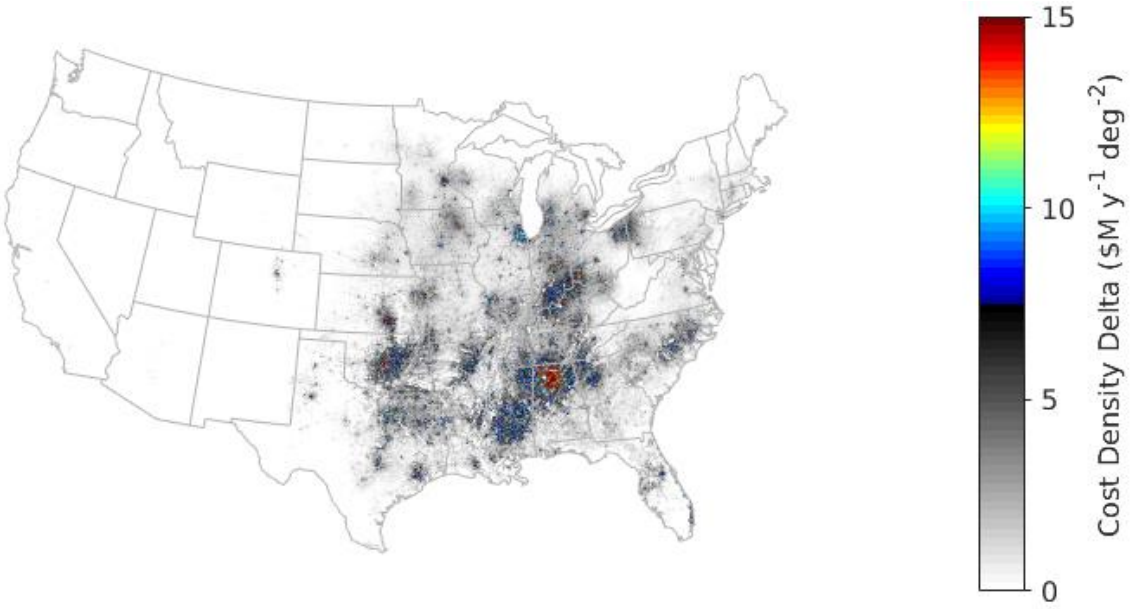

Figure 5.1. Density map of the remaining benefit pool for tornadoes.

The model also enabled estimation of the present-day net benefit (casualty reduction benefit minus sheltering cost) of tornado warnings ($1921M per year), as well as the benefit associated with the transition from county-based to storm-based tornado warnings ($732M per year).

The quantification of rapid scan effects is based on a small number of past experiments and is less robust than the other parts of the benefit model. In order to drive down this uncertainty, it is recommended that more statistics be gathered on the effects of faster volume scans on tornado warning performance by utilizing existing and new radars capable of fine temporal resolution observations.

Flash Floods

In the U.S., operational flash flood warning decisions are primarily based on comparing flash flood guidance (FFG) with precipitation estimates. FFG outputs estimates of rainfall accumulation needed to cause flash flood conditions on a typical small stream or urban area in the region of interest. By definition, flash floods occur within six hours of the causative event. Thus, when the cause is heavy rain, in order for forecasters to issue timely flash flood warnings, they mostly utilize multi-sensor precipitation estimator (MPE) products for comparison with FFG thresholds (waiting for flow level measurements from stream gauges delays the decision, and, in any case, many potential flash flood areas are in ungauged headwaters). MPE ingests radar, rain gauge, and satellite data; rain gauge data are used to help correct biases in the radar and satellite estimates. The dominant MPE contributor is radar quantitative precipitation estimation (QPE), while satellite-based QPE is mainly used to fill gaps in radar coverage.

The flash flood warning decision process, therefore, depends on the accuracy of the FFG and MPE products. FFG threshold errors are dependent on FFG type and are specific to each catchment basin. There are various sources of MPE errors, and the situation is further complicated by the fact that forecasters do not utilize a uniform set of data products and decision support tools. To analyze the impacts of input data errors on flash flood warning performance would require an in-depth case study at a particular forecast office using a detailed hydrological model of a catchment basin—this is not conducive to a national-scale statistical analysis.

In this study, we took a simple approach. Since poor radar coverage is a significant source of radar QPE error, we hypothesized that flash flood warning performance would depend on radar coverage, even without taking into account the other error sources in the warning decision process. Using 11 years (October 2007 to December 2018) of historical data, we showed that, indeed, better weather radar coverage (as measured by FVO and CHR) led to improved flash flood warning performance (detection probability and false alarm ratio). By linking radar coverage directly to warning performance, we bypassed the very complex problem of characterizing MPE and FFG product errors, considerably streamlining the analysis.

Next, we were able to show that flash flood casualty rate was meaningfully dependent on population, fraction of population residing in mobile housing, and the presence of a warning. The resulting regression model could then be used to generate casualty rate estimates on a geospatial grid, given the outputs of the flash flood warning performance model, population, flash flood occurrence rate, and mobile housing statistics.

The flash flood benefit model was run on the existing CONUS WSR-88D network as well as on other basic scenarios. Key results were as follows (values are given in 2019 dollars):

- Current weather radars provide a flash-flood-based benefit of $316M per year.
- The remaining radar-based benefit pool is $13M per year (see Figure 5.2 for geospatial distribution).
- The current flash flood warnings provide a benefit of $392M per year.
- The remaining warnings-based benefit pool (obtained with 100% of flash floods warned) is $69M per year.
- There is no statistically meaningful difference in flash flood warning performance between the pre-dual-polarization and post-dual-polarization WSR-88D periods.

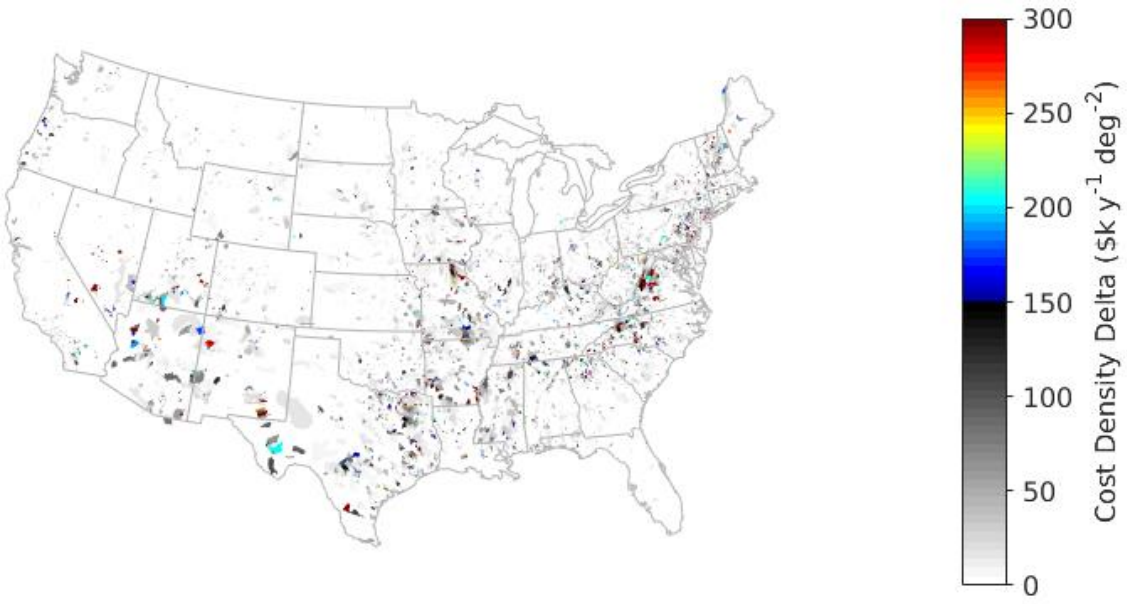

Figure 5.2. Density map of the remaining radar-based benefit pool for flash floods.

The circumstances of flash flood casualties are very complex and difficult to model statistically. Many flash flood fatalities in the U.S. occur while the victim is away from their residence, which cannot be precisely characterized with population data. It is difficult to capture factors like real-time access to flash flood warnings and likelihood of response, while data on event characteristics such as flow speed and depth are not universally available. In our casualty regression analysis, we considered potential causative factors with data available geospatially on a national basis, and discarded those that were not statistically reliable predictors. The resulting regression model is necessarily a simple one, but the large number of data points used in the analysis provides a high level of statistical robustness that would not be available in a more detailed case study.

The remaining radar-based benefit pool of \$13M yr^{-1} is modest, which is indicative of the effective coverage provided for flash floods by the current weather radar network. If faster volume scan updates could be shown to improve flash flood warning performance, this pool may increase. Such an analysis is recommended as a follow-on to this study.

Weather Radar Network Quantitative Precipitation Estimation Accuracy

QPE has been an intense research focus area for decades due in part to its critical impact on flash flood warning guidance. Due to the relative lack of rain gauge density, especially in rural and mountainous areas, radar provides invaluable rainfall estimation information in times of torrential rainfall and flash flooding. However, the accuracy of QPE is a topic of nearly constant investigation. There are numerous methods for QPE, ranging from reflectivity factor/rainfall rate relationships (Z-R) to the use of polarimetric estimates for Z/differential reflectivity/rainfall rate (Z-Z_{DR}-R), specific differential phase/rainfall rate (K_{DP}-R) and specific attenuation/rainfall rate R(A). Each has its own strengths and weaknesses, and all of the methods have been investigated extensively in the literature.

As the National Weather Service develops radar observation enhancements (e.g., polarimetric capabilities) and considers deployment of "gap-filler" radars or other network augmentations, QPE accuracy will continue to be a central concern due to the role weather radars are expected to play in flash flood forecasting. Not only do different methods for QPE have varying characteristics, but the radar network itself has a significant impact on QPE performance and capability. The specific attenuation, or R(A) method, does not perform reliably within and above the melting layer. Z-Z_{DR}-R is also unreliable within and above the melting layer. For these reasons, the Z-R relationship is still used in these regions, even when polarimetric estimates are available. Given the different methodology of the Z-R technique, and, hypothetically, less-accurate results due to its use above the melting layer, one could postulate that radar network density is a driving factor in QPE accuracy, especially in areas far from a radar.

The NWS Radar Operations Center (ROC) has recently approved moving forward with switching the WSR-88D operational QPE method to R(A), due in part to difficulties in managing polarimetric bias within the WSR-88D fleet. Along with concerns regarding polarimetric calibration in future network designs (e.g., as part of a phased-array architecture), the eventual switch to R(A) could conceivably provide a more reliable and uniform QPE technique across the WSR-88D (or a future) network. Of the available methods, given its relatively recent advancement, R(A) is yet to be extensively studied on very large datasets, although the National Severe Storms Laboratory (NSSL) and the ROC have made great headway in this area. Additional comprehensive studies of R(A) accuracy will be beneficial.

QPE errors have been studied in various ways, including with and without polarimetric radar, using disdrometers, and using both quality-controlled and non-quality-controlled rain gauges. Different error metrics and models have been used, but in general, the goal is to determine how closely the remotely sensed radar estimates mirror in situ measurements. Many of the aforementioned studies have utilized one radar; however, network-based studies are less prominent in the literature. Among the most common network-based studies are those that quantify accuracy of the multi-radar multi-sensor (MRMS) QPE methodology, a mosaic QPE

technique using the entire WSR-88D network. However, MRMS studies have not investigated how different network designs would change overall method accuracy.

In this study, we present the development of a support vector regression (SVR) method for modeling QPE accuracy based on a variety of system-based factors. The errors in this analysis are quantified using a large database of collected cases truthed with Automated Surface Observing System (ASOS) rain gauges. The factors considered for error sources are height of the beam above ground level (including topography effects), cross-range resolution, and gauge-observed rainfall rate. The trained model is then applied to the WSR-88D network in order to generate a quantification of network-wide, system-level QPE error. Different rainfall rates (based on climatological ASOS data) are considered. Finally, the model is applied to example future network scenarios in order to show its potential usefulness for network design.

Details of methodology and results are documented in the following publication:

- Kurdzo, J. M. and J. Y. N. Cho, 2020: QPE accuracy benefits for weather radar network design. *J. Appl. Meteor. Climatol.*, under review.

Current Network Analysis

The primary analysis focused on the R(A) QPE method, since this is the technique the NWS will be moving towards in the near future. A total of 4,750 1-hr cases were manually identified across three consecutive summer seasons (May – August of 2015 – 2017), and were processed using the R(A) method. The QPE at all local ASOS sites was calculated and compared to the gauge measurements over the 1-hr timespan. Using this data collection technique, over 220,000 ASOS data points with measurable precipitation were used in this study.

The data were then fed into an SVR in order to train the model based on various metrics. The primary metrics for comparison were the gauge-measured rainfall rate and the height of the beam above ground level. The SVR then estimated QPE error for these combinations, with negative errors indicating underestimates and positive errors indicating overestimates. Results from the SVR for the R(A) method are shown in Figure 5.3, assuming a beam elevation angle of 0.5 deg.

In order to apply these results climatologically, the NOAA Atlas project was used to calculate rainfall return rates for the entire CONUS. A 2-year, 1-hr return rate was selected, as it most-closely related to the frequency of flash-flood events in the CONUS. The combined Atlas dataset for this “flash flood rainfall rate” is shown in Figure 5.4. The existing WSR-88D network was then used to compute minimum beam heights across the CONUS. Both of these datasets were fed into the SVR in order to generate the CONUS-wide QPE error expectation for flash-flood events, shown in Figure 5.5.

Areas with strongly negative errors indicate significant underestimates of rainfall by the closest WSR-88D. This can indicate the tendency to under-warn in areas of high rainfall rate and far

from a radar, which was at least partially confirmed in our benefit analysis in the previous sections. In these cases, if QPE is being underestimated, it may cause a flash flood warning to be issued too late, or not at all, in cases where a flash flood warning would have been issued with correct rainfall estimates or observations. This issue could lead to injuries or, in extreme circumstances, loss of life.

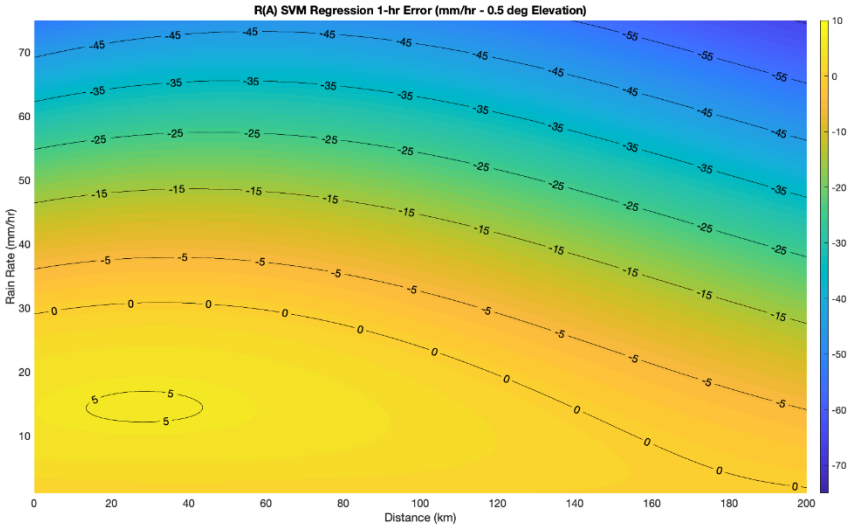

Figure 5.3: SVR model results for the R(A) QPE method using 4,750 cases across the CONUS. Rain rate is the gauge-measured "truth" rainfall rate. The shading and contours represent the expected errors at different combinations of range and observed rainfall rate based on a comparison of radar and ASOS gauge data in the collected cases.

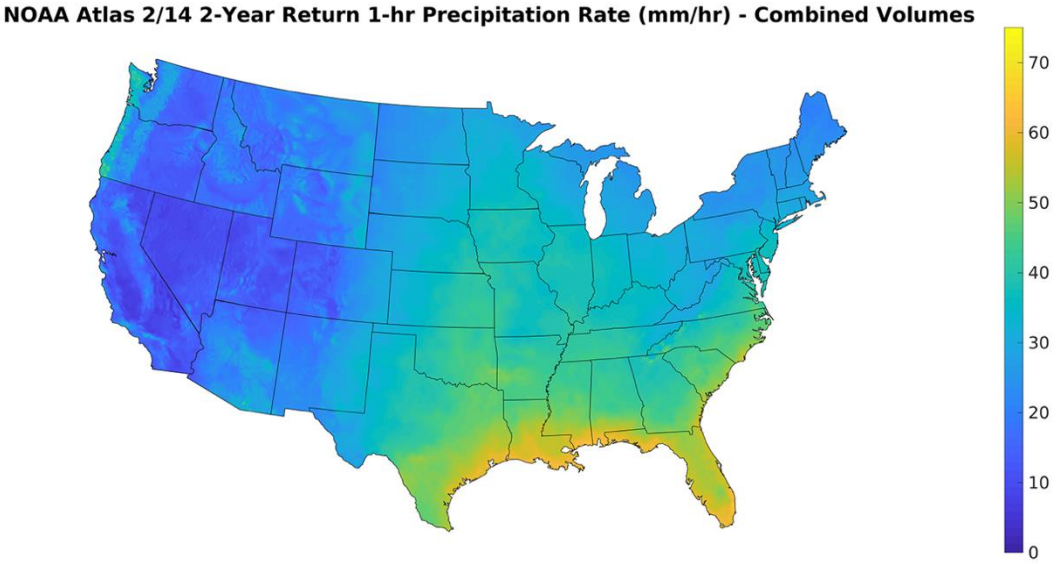

Figure 5.4: Atlas-derived 2-year/1-hr return rainfall rates across the CONUS, in mm hr^{-1}. A combination of all Atlas 14 and Atlas 2 volumes was completed, with linear interpolation at volume boundaries. The Atlas 2 data were interpolated in time in order to match the 2-year/1-hr returns native to Atlas 14.

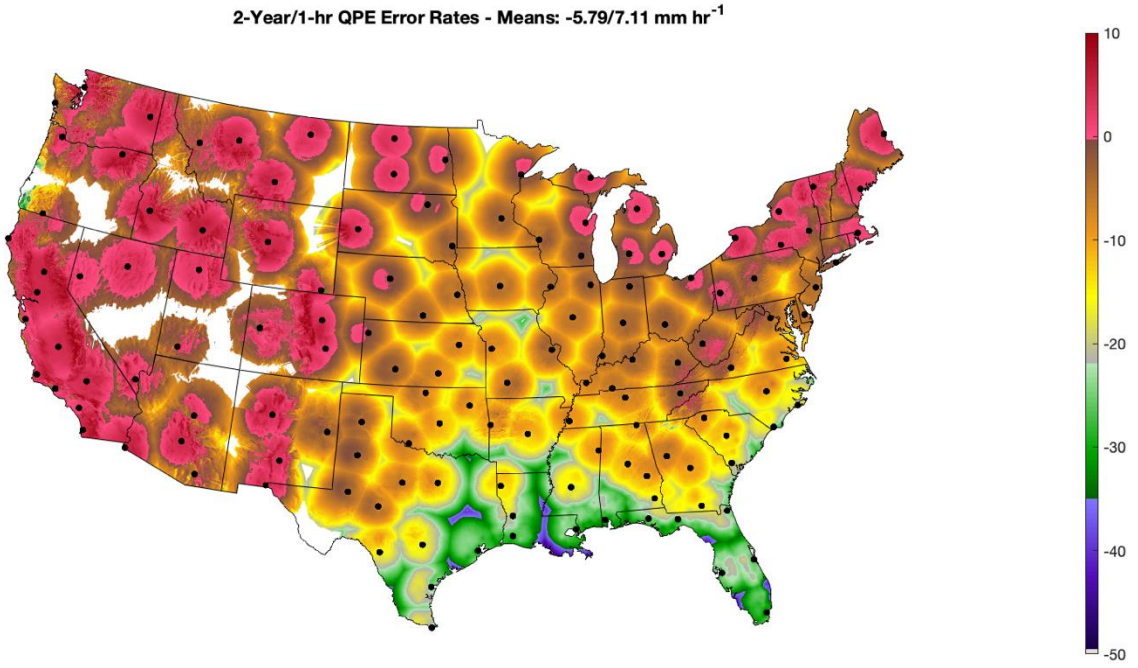

Figure 5.5: Application of the R(A) SVR model results from Figure 3 to the current WSR-88D network across the CONUS. Atlas-derived 2-year/1-hr return rainfall rates are assumed (see Figure 4). The shading is expected QPE error in mm hr^{-1}. The means in the header (-6.79 and 7.98 mm hr^{-1}) represent the total and absolute value means across the CONUS, respectively. Radar sites are marked by black dots.

Future Network Analysis

One advantage of this modeling effort is the ability to apply the results to future potential weather radar network designs. This allows for the ability to compare the current network to potentially new network designs in order to quantify benefit from improvement. We took two means of the error across the CONUS—a true mean, and a mean of the absolute value of error. Eight different scenarios were analyzed for their improvements relative to the WSR-88D network. A combination of WSR-88D, TDWR, Airport Surveillance Radar (ASR) with the Weather Systems Processor (WSP), all other ASRs, Air Route Surveillance Radar (ARSR-4), and Common ARSR (CARSR) were used to create the scenarios. An example of Scenarios 3 and 4 is shown in Figure 5.6, while all of the scenario values are listed in Table 5.1.

All of the scenarios assume that each radar is fully polarimetric, although the replacement radars were considered to have the range and beamwidth of the radars they were replacing. We assumed that the replacement radars were pencil-beam systems, with both azimuthal and elevation beamwidths approximately equal to the effective azimuthal beamwidth of the radars they replaced. This means that replacements of TDWR, ASR, ARSR-4, and CARSR had maximum ranges of 90, 111, 467, and 370 km, respectively, and beamwidths of 1.0, 2.0, 1.7, and 1.7 deg, respectively. Note that although the TDWR has a 0.5-deg beamwidth, the processed data are at 1.0-deg azimuth spacing. Additional scenarios that replaced radars with non-polarimetric

versions were considered, but offered limited improvement due to the use of the R(Z) method. These scenarios are not included in this study.

A listing of the scenarios and their mean 1-hr QPE error is presented in Table 5.1. Scenarios 4, 7, and 8 include all ASR sites, and represent the most significant improvements in mean error, with 46.80%, 52.50%, and 59.93% improvements over the current WSR-88D network, respectively. The addition of the CARSR sites (Scenario 6) also provides an improvement of 26.42%. Without inclusion of all ASR sites, such as in Scenarios 2, 3, and 5, only modest improvements to the baseline mean error are observed, with 3.63%, 12.26%, and 11.92% improvements in mean total error, respectively.

Much of the impact on improvement from these scenarios rests with the location of the added sites relative to current gaps in coverage. This is also heavily impacted simply by the number of CONUS sites, which for TDWR, ASR with WSP, remaining ASR, ARSR-4, and CARSR options are 44, 33, 261, 40, and 73, respectively. Therefore, it makes intuitive sense that inclusion of the ASR sites would make the most significant impact, with the CARSR sites having a secondarily large impact. Of course, Scenario 8, which includes all radars, displays the most significant improvement relative to the baseline. It is important to note that none of these scenarios alone would make sense due to the overlapping nature of many radar sites. A future network, at least in the United States, would likely use some combination of sites that provide the most benefit without significant overlap. The scenarios listed here are simply a thought exercise to compare with previous analyses in the literature and to show the capabilities of the technique described in this study.

There is significant overlap when including all WSR-88D, TDWR, and ASR radars due to their common proximity to airports. To generate more realistic scenarios, we created a cost-benefit metric that determines the ideal locations for new radars. This metric is called Possible Improvement Factor (PIF), and it considers the possible QPE error improvement multiplied by a base-10 logarithm of population density. The possible QPE error improvement is determined by assuming every grid point is 1 km from a radar (but still maintains the Atlas-defined rainfall rate). This generation of a “perfect” error map shows the best-possible scenario for radar coverage given the CONUS-wide rainfall rates. The perfect error map, along with a population density database, is used to generate the PIF at full-grid resolution. The PIF for the existing WSR-88D network is shown in Figure 5.7. Note areas of western North Carolina and southeast Pennsylvania that are devoid of WSR-88D coverage and have relatively high rainfall rates (resulting in higher errors but a high possibility for improvement), while also presenting a relatively high population density.

TABLE 5.1. Evaluation of total and absolute mean QPE error across the CONUS for Scenarios 1-8. Scenario 1 is the existing WSR-88D radar network, while all other scenarios provide a relative improvement compared with the WSR-88D network. The scenarios are marked by the inclusion of different radar networks, including WSR-88D (W), TDWR (T), ASR with WSP (AW), all other ASR (A), ARSR-4 (4), and CARSR (C).

Scenario	Total Mean 1-hr QPE Error	Improvement from WSR-88D	Mean Absolute 1-hr QPE Error	Improvement from WSR-88D
S1: W	-5.79 mm hr^{-1}	–	7.11 mm hr^{-1}	–
S2: W + T	-5.58 mm hr^{-1}	3.63%	6.93 mm hr^{-1}	2.53%
S3: W + T + A*w*	-5.08 mm hr^{-1}	12.26%	6.81 mm hr^{-1}	4.22%
S4: W + T+ A*w* + A	-3.08 mm hr^{-1}	46.80%	5.97 mm hr^{-1}	16.03%
S5: W + T + 4	-5.10 mm hr^{-1}	11.92%	6.74 mm hr^{-1}	5.20%
S6: W + T + 4 + C	-4.26 mm hr^{-1}	26.42%	6.17 mm hr^{-1}	13.22%
S7: W + T + A*w* + A + 4	-2.75 mm hr^{-1}	52.50%	5.88 mm hr^{-1}	17.30%
S8: W + T + A*w* + A + 4 + C	-2.32 mm hr^{-1}	59.93%	5.55 mm hr^{-1}	21.94%

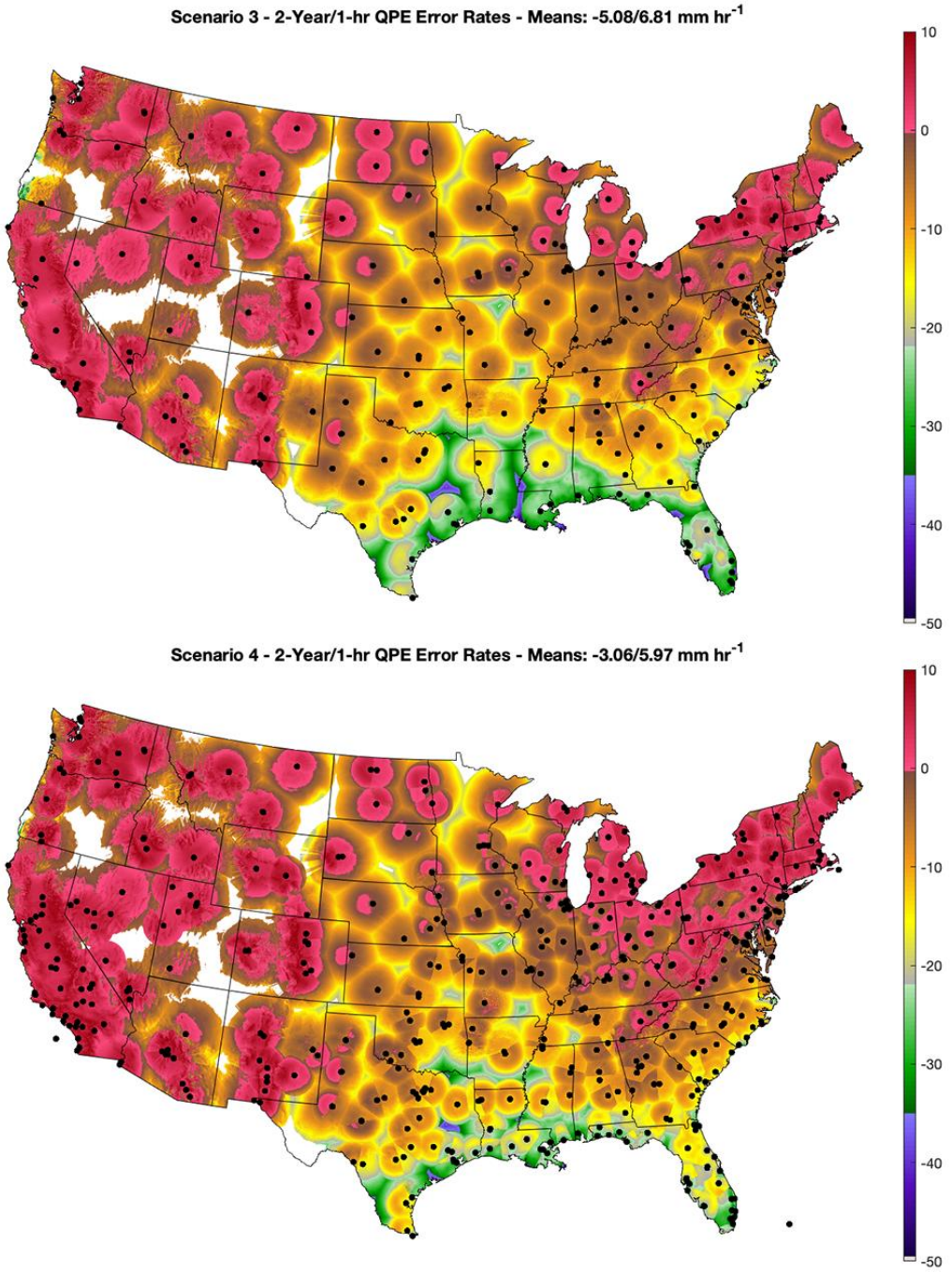

Figure 5.6: As in Figure 5.5, but for the R(A) method in Scenarios 3–4 for radar network design. These scenarios are designated in Table 5.1.

Our experimental optimization then used the PIF to place radars at all possible locations and assess cost-benefit. The possible locations investigated included all TDWR, ASR, ARSR, and CARSR locations. Note that this is clearly not exhaustive, but it does significantly limit computational complexity. The first radar is placed in western North Carolina, and the second

radar is placed in southeast Pennsylvania (not shown). This continues, lowering the remaining available PIF with each additional radar. We ran this algorithm out past 350 additional radars and generated a PIF vs. additional radars plot, shown in Figure 5.8. The original benefit is high due to the steep drop in available PIF early in the curve, but the benefit levels out with more radars. The benefit pool is cut in half after roughly 80 additional radars, and stagnates after roughly 200 additional radars. This methodology is a useful way to assess cost-benefit for the upcoming stages of this study. All radars added in this example are WSR-88D-type radars (i.e., pencil-beam, 1-deg, polarimetric, full range, etc.).

Key results for this portion of the study were as follows:

- The use of R(A) is anticipated to greatly improve QPE accuracy across the WSR-88D fleet.
- QPE accuracy is dependent on height of the beam and actual rainfall rate.
- A denser radar network has the potential to improve mean QPE error by over 50%.
- Approximately 80 “gap-filler” polarimetric radars offers half of the remaining QPE benefit pool, while the cost-to-benefit stagnates at approximately 200 additional radars.

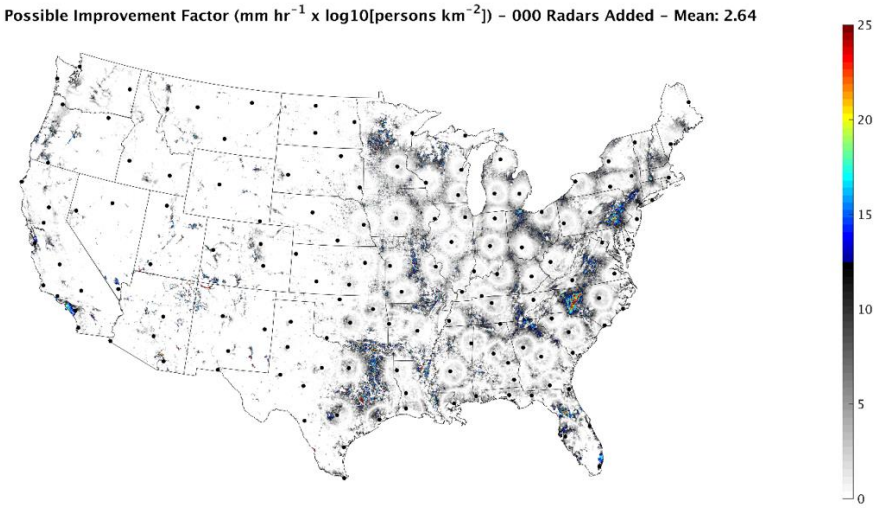

Figure 5.7: Possible Improvement Factor (PIF) for the CONUS, considering only the existing WSR-88D network. PIF is defined by the possible improvement of error relative to "perfect" multiplied by the base-10 logarithm of population density. Western North Carolina and southeast Pennsylvania areas provide the highest PIF.

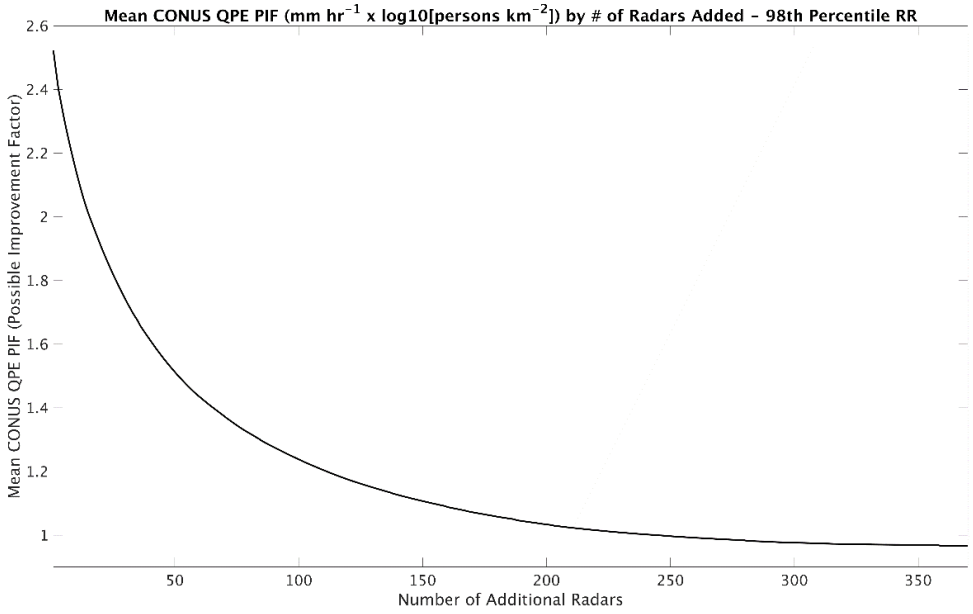

Figure 5.8: Mean CONUS PIF as related to the number of additional radars in the network (relative to the existing WSR-88Ds). Note that additional radars for this example are only considered at existing TDWR, ASR, ARSR, and CARSR locations. The original benefit is high due to the steep drop in available PIF early in the curve, but the benefit levels out with more radars. The benefit pool is cut in half after roughly 80 additional radars, and stagnates after roughly 200 additional radars.

6. Dual Polarization Calibration and Correction

Introduction

The meteorological radar research community has been exploring the use of dual polarization since the 1970's, and the technology and science reached sufficient maturity for operational deployment at the beginning of this decade. Previously unavailable microphysical information on hydrometeor size, shape, orientation, density and water content has significantly improved NOAA's capabilities across mission areas including flood warning, hail detection, tornado detection and winter weather warnings. The capability to provide high-quality dual polarization observations has quickly become a non-negotiable requirement for any future operational radar.

To be operationally useful, dual-polarization scattering properties of precipitation must be measured with very high accuracy. For example, biases of a few tenths of a decibel in estimates of "differential reflectivity (Z_{DR})" – the ratio of the received horizontal (H) and vertical (V) signal components - may increase rain rate estimate errors by 10% or more, which is significant in comparison to other sources of error.

Such accuracies are readily achieved with a reflector antenna but can be much more problematic when using an electronically steered array. For practical radiating elements, the horizontal and vertical polarization patterns of the radiating antenna elements vary by many decibels as the beam is electronically steered in azimuth and/or elevation angles well away from broadside. In addition to this "geometric" bias, electronic coupling between the H and V channels can be significant relative to the desired measurement accuracy.

This section summarizes analysis and technology development addressing PAR capability to achieve the required accuracy for polarimetric variable estimates. Section 6.1 describes computational electrodynamic modeling (CEM) methods that, with further development, will provide an analytic basis for interpretation of experimental results. Recent experimental results using the Advanced Technology Demonstrator, a large, S-band dual polarization phased array are discussed in Section 6.2. In Section 6.3, we discuss the development of mutual coupling calibration techniques and a novel drone-based far-field phased array radar calibration method.

6.1 Computational Electrodynamic Modeling Research[8]

Here, we present a computational electromagnetic (CEM) study of the Ten Panel Demonstrator (TPD), a 640-element S-band, dual-polarization phased array that utilizes the same active array architecture as the ATD. The study includes modeling of the TPD's antenna from the single element to the full array with and without radar's radome (protective cover of the antenna). Of special interest is the comparison of CEM solvers applied to the single panel, common to the ATD and the TPD, in terms of numerical complexity, solving time, and accuracy. We present a more detailed information about these topics is in the report by Mirkovic and Zrnic (2019).

[8] Principal Investigators: Dusan Zrnic and Djordje Mirkovic (NSSL and CIMMS)

Problem of Calibration

The modeling process can be subdivided into three stages. First is the modeling of a single radiator (Fig. 6.1.1d), second is modeling of a single panel (Fig. 6.1.1c) and finally the full radar array modeling (Fig. 6.1.1b). Naturally, complexity of the model increases with the number of elements. As the modeling of three-layer stacked patch differentially fed antennas is well documented we skip the single element model and start with the single panel.

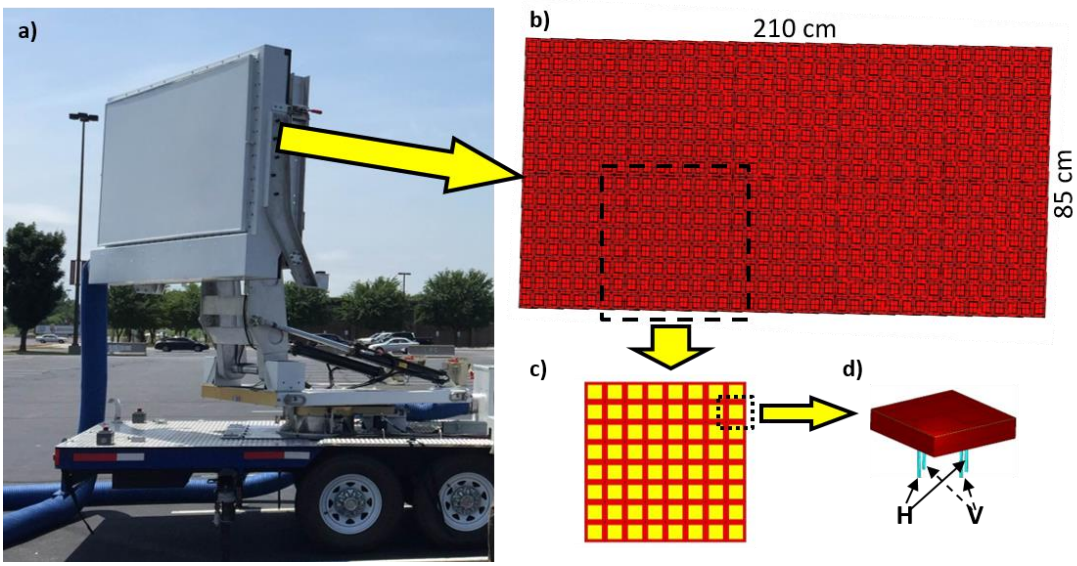

Fig. 6.1.1. ***a)*** *The Ten Panel Demonstrator radar;* ***b)*** *the antenna model;* ***c)*** *antenna panel;* ***d)*** *the antenna element with four differentially fed probes.*

The single panel consists of 64 radiating elements arranged in 8 by 8 array. This array was measured and modeled with only one of the central elements active, while the others were load-matched. We measured and compared both copolar and cross-polar radiation patterns in the E plane (i.e., in the plane of the electric field E_h here assumed to be horizontal), H plane (the plane of the magnetic field orthogonal to E and herein vertical), and D the diagonal plane. For brevity only the H and D cuts are presented. In collaboration with the OU ARRC, we simulated the array using the same computing capabilities in WIPL-D, CST, and HFSS solvers (commercial software). As it is obvious in Fig. 6.1.2, the HFSS had some convergence issues on our machine, however these results are comparable. Simulation of the patterns at both polarizations by WIPL-D took 3 h and 20 minutes, by CST about 5 h and 30 minutes, while HFFS achieved partial convergence (the parameter of convergence $\Delta_S = 0.027$) after 6 hours of simulation. It is important to note that simulation on our machine failed at this point.

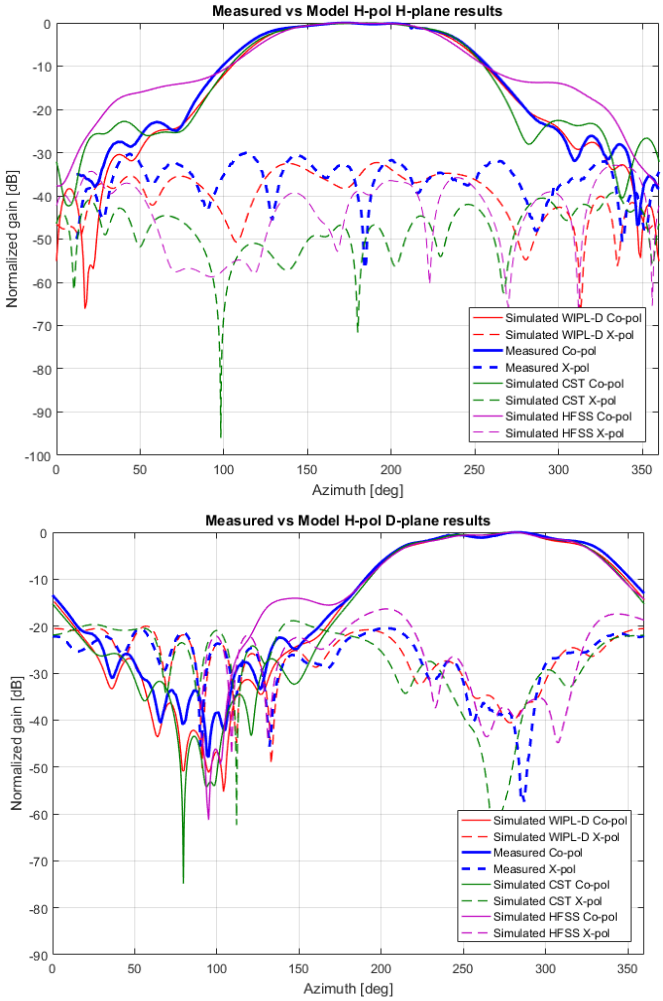

Fig. 6.1.2. Measured and simulated patterns of the single panel array with only one central element excited and others load matched. Compared are simulations using WIPL-D, CST and HFSS solver for the E_h polarization in the vertical plane (left) and in the diagonal plane (right).

From Fig. 6.1.2 (top) we see that all simulated patterns agree quite well with the measurement in the 100^o to 250^o region (this is the span of the main beam) although the measured main lobe is slightly wider. CST and WIPL-D main lobe patterns between 50^o and 150^o match well but the measured main lobe is a bit higher. The pattern computed with HFSS misses the sidelobes, due to convergence problems. On the opposite side of the main lobe (200^o to 275^o), the pattern computed with CST falls off quicker compared to the measured and WIPL-D simulated patterns. The computed cross-polar patterns by the CST solver are about 15 to 20 dB lower than the measured and simulated patterns by WIPL-D. The pattern computed with the HFSS is in-between the patterns from these two simulators.

For the D-plane cut (Fig. 6.1.2 bottom) within the main lobe, the shape of the sidelobes computed by WIPL-D is in better agreement with measurement than the shapes computed by the other two solvers. This is important because the cross-polar lobes, within the main lobe region,

are the main contributors to the biases in the polarimetric variables. For example, if the sidelobes within the main lobe exhibit four symmetric peaks, the bias in polarimetric variables caused by coupling is significantly reduced (Zrnic et al. 2010, Galletti and Zrnic 2011). The ones computed with CST agree almost as well except at angles 0^o to 50^o. The D-plane has the strongest cross-polar radiation because it cuts through the two peaks within the main lobe. Thus, it can serve as a benchmark for quantifying the cross-pol simulation results.

Full array modeling

The full TPD array consists of ten panels arranged in 2 by 5 configuration. The array has 640 elements with an area of about 2 m^2. For the CEM simulators, this array is fairly large as the problem would yield about 1.2 million unknowns. However, this number can be decreased by employing the symmetry option in the WIPL-D solver. The symmetry argument should be applied to the full topological structure while keeping all excitations independent of each other. Using the symmetry, we were able to model this size array and implement beam steering capability into the model. The complete model is driven by 2560 excitations, for H and V polarization, that are separately controlled. To our knowledge, this is the first time that the simulation of such magnitude has been achieved in a commercial software.

Implementing the full 3D CEM model is of special importance, because approximate techniques, such as infinite array method, may fail to provide necessary precision in the model of cross-polar radiation patterns. To make this point clear we present in Fig. 6.1.3 the results of simulations by the HFFS software.

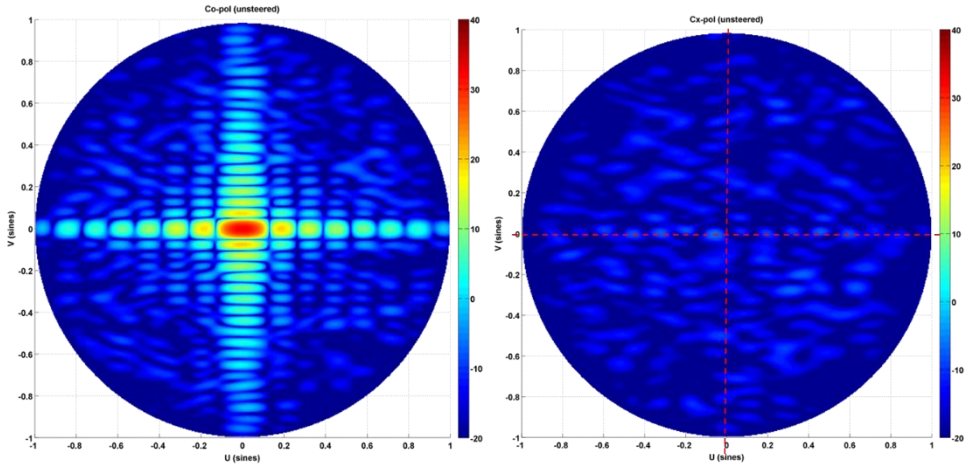

Fig. 6.1.3. Ten Panel Demonstrator copolar (left) and cross-polar (right) radiation pattern at broadside calculated using the infinite array method in HFFS software. The color bar is dBi and the red dotted lines in the cross-polar patterns facilitate reading.

Comparing the results in Fig. 6.1.3 with WIPL-D broadside results in Fig. 6.1.4, we see that the copolar main lobe and sidelobes in the principal planes are well approximated. However, out of

the principal plane, copolar far sidelobes in Fig. 6.1.3 (left) are not symmetric. A more significant deficiency of the approximate technique is evident in the cross-polar pattern. The symmetry of the cross-polar pattern is absent in the results in Fig. 6.3 (right). Furthermore, the results do not predict four symmetrical cross-polar lobes located at the diagonals. This is especially important as the phases of adjacent lobes differ by 180^o. This phase difference cancels the first order bias terms in the polarimetric variables. Without this cancelation the cross-polar lobes would produce the largest contribution to the cross-polar voltage patterns and therefore to the ensuing polarimetric variables.

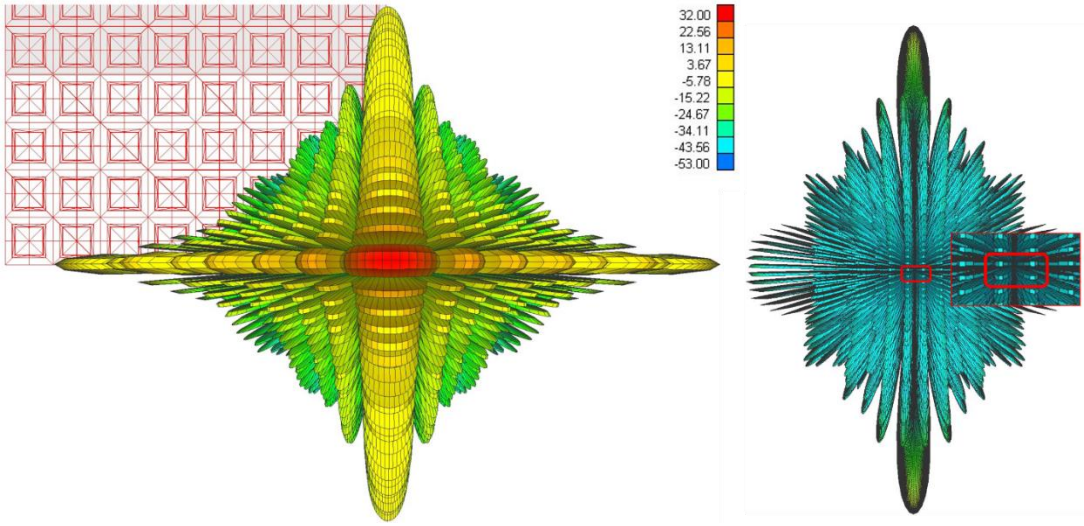

Fig. 6.1.4. Antenna patterns of the ten-panel demonstrator, (left) copolar $f_{hh}(\theta, \phi)$, (right) cross-polar $f_{vh}(\theta, \phi)$ and its enlarged values within the main beam (encompassed with the rectangle). The beam is pointing broadside. The peak to peak isolation within the main lobe is over 50 dB while the cross-polar minimum is aligned with the copolar peak. The color bar indicates values in dBi.

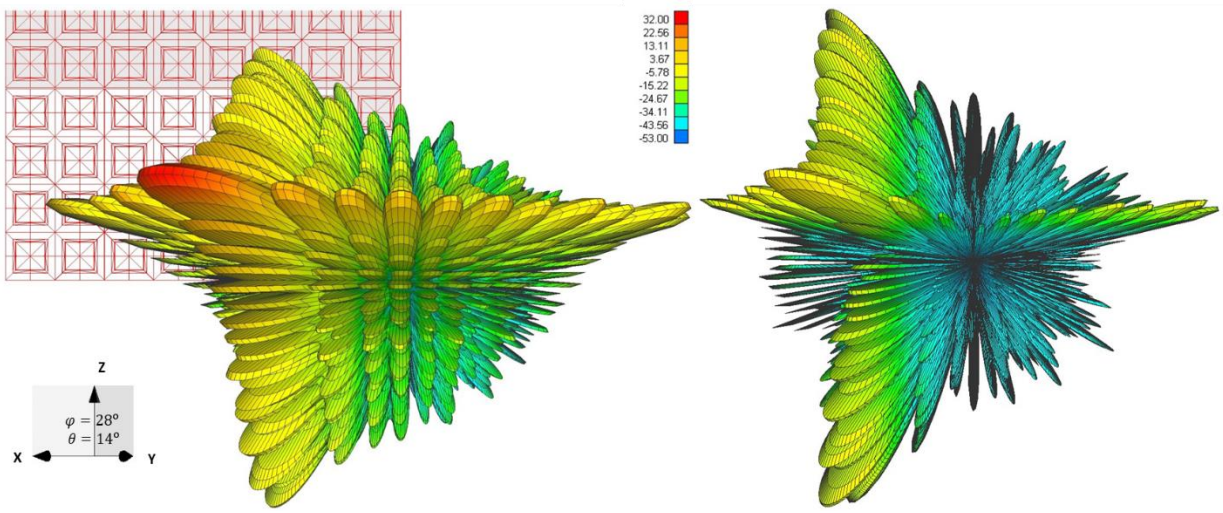

Fig. 6.1.5. As in Fig. 6.1.4 but the beam is pointing at 28º in azimuth and 14º in elevation. The peak to peak isolation is about 24 dB and the cross-polar peak is within the main beam of the copolar pattern. The color bar indicates values in dBi.

If the beam is steered away from the principal planes (e.g., by a command in azimuth ϕ = 28º, and elevation θ_e = 14º), (Fig. 6.1.5) the cross-polar lobe formation changes significantly. The copolar beam axis is at the azimuth 28.5º and elevation 12.25º. Clearly, the executed direction is offset from the commanded one. This may not be very significant considering that the beamwidths are relatively large; still, it should be accounted for. The cross-polar peak is within the main beam of the copolar pattern but is positively offset from its center in azimuth by 1º and negatively offset in elevation by 0.5º. It is about 24 dB below the copolar main lobe and is caused by the geometrical coupling and "non-radiating" sides of patches. Low isolation will cause bias in the case of SHV (simultaneous transmission and reception of the H and V polarized fields) polarimetric mode. This mode is implemented on the WSR-88D and on almost all other operational weather radars. If the phase coding/filtering is used in the SHV mode (to eliminate the first order bias terms) the 24 dB isolation might be sufficient. Nevertheless, this is not the total isolation between the channels as the backend may introduce additional coupling.

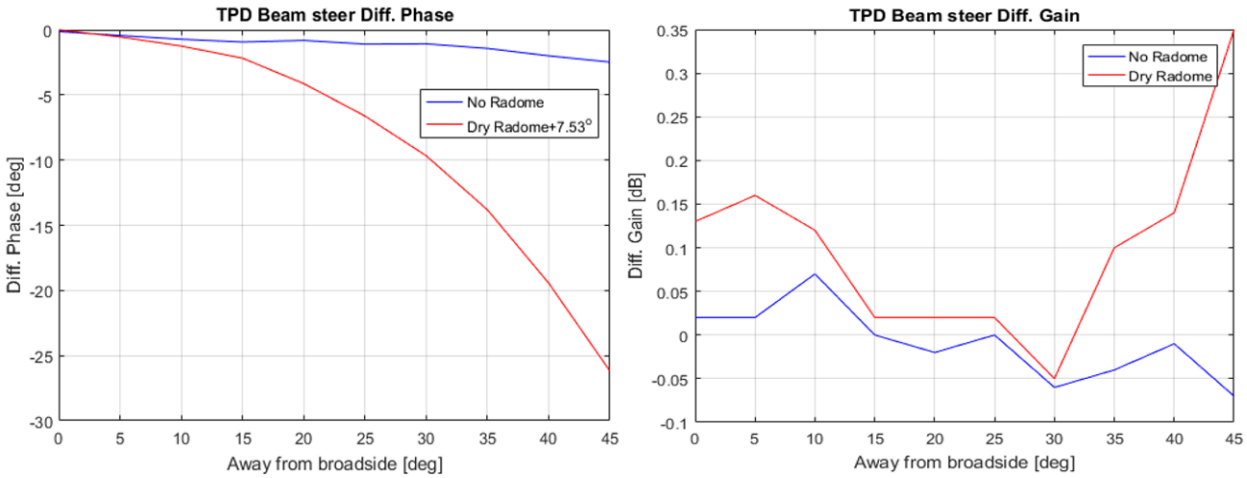

Fig. 6.1.6. - Differential phase and differential gain calculated at the beam peak of the TPD antenna as a function of beam position. Curves in blue represent the values for the antenna without radome whereas the red curves represent values for the radome-covered antenna.

The antenna creates a differential phase between the horizontally and vertically oriented fields. Angular dependences of the differential phase and gain of the TPD as a function of beam pointing direction in the horizontal principal plane are plotted in Fig. 6.1.6. The values in Fig. 6.1.6 are calculated for the antenna without radome cover (blue) and with radome cover (red). The differential phase (Fig. 6.1.6 left) of the TPD antenna with the radome cover exhibits significant change. The dependence is similar to the one observed at zenith pointing measurements (Mirkovic and Zrnic 2018a, Mirkovic and Zrnic 2018b). One should note that the phases in Fig.6.1.6 are one-way, whereas the total differential phase affecting radar measurements is the two-way (transmit and receive) value. In general, transmission and reception antenna effects are not identical (i.e., there can be taper on reception) thus should be calculated separately.

Differential phase change by the TPD antenna without the radome is on the order of 2 to 3^o and is due to the change in the phase center position while beam steering. With the radome, the differential phase increases to about 26^o, at the azimuth of 45^o. This significant difference is caused by the reflection/refraction properties of the radome that are not the same at the two polarizations. While the vertically (V) polarized fields have parallel incidence to the radome, the horizontally (H) polarized fields have oblique incidence as the beam is steered in the horizontal plane.

Conclusions

CEM tools had very limited use in quantifying the performance of phased array antennas meant for weather observations. Herein we examined the precision of the WIPL-D and other tools in modeling polarimetric phased array weather radar antenna and compare their simulation times and accuracy. Specifically we have applied these tools to build step by step a model of a large

phased array dual polarization antenna. In this case the antenna is part of the Ten Panal Demonstrator, a polarimetric radar serving to inform the design of PAR larger antennas with dual polarization capability for weather observations.

Our first step in building the model was to simulate the patterns of a single patch antenna designed by the MIT Lincoln Laboratory (Mirkovic and Zrnic 2019). In the current paper we simulated the patterns of one excited patch (element) embedded in an 8x8 pannel. We have determined that the WIPL-D solver yielded the patterns that were closest to the measured ones. Of special importance is that the cross-polar patterns within the mainlobe agree best with the measurements, because these patterns determine the largest part of the bias in the polarimetric variables. We also demonstrate that the infinite array approach in modeling the antenna is inadequate for quantitative assessment of the cross polar patterns.

The second step on the way to full simulation of large PAR antennas is our simulation of the patterns (copolar and cross-polar) on the Ten Panel Demonstrator (TPD) antenna. This phased array antenna is most likely among the largest that can be fully modeled and thus represents an important milestone in developing hybrid techniques to address larger antenna arrays.

References

Galletti, M., and D. S. Zrnic, 2011: Bias in copolar correlation coefficient caused by antenna radiation patterns. *IEEE Trans. Geosci. Remote Sens.*,**49,** 2274-2284.

Mirkovic, Dj., and D. S. Zrnic 2018a: Polarimetric Weather Radar Calibration by Computational Electromagnetics. *Applied Computational Electromagnetics Society Journal*. 2019;34(2):342-346.

Mirkovic, Dj., and D. S. Zrnic, 2018b. Polarimetrie calibration using the computational electromagnetics approach. *IEEE Radar Conference (RadarConf2018),* Oklahoma City, OK, 2018, pp.1348-1352 Doi:10.1109/RADAR.2018.8378760 .

Mirkovic, Dj., and D. S. Zrnic, 2019: Computational Electromagnetic Tools Applied to the Polarimetric Phased Array Antenna. *National Severe Storms Lab. (NOAA) Report p* Web: https://www.nssl.noaa.gov/publications/mpar_reports/

Zrnic, D.S., R.J. Doviak, G. Zhang, and R.V. Ryzhkov, 2010: Bias in differential reflectivity due to cross-coupling through the radiation patterns of polarimetric weather radars. *J. Atmos. Oceanic Technol*., **27**, 1624-1637.

6.2 Preliminary Calibration Results Using the Advanced Technology Demonstrator (ATD)[9]

The Advanced Technology Demonstrator (ATD) is an S-band planar polarimetric phased array radar (PPPAR) that is funded through a joint collaboration of the National Oceanic and Atmospheric Administration (NOAA) and the Federal Aviation Administration (FAA). It is being developed by the National Severe Storms Laboratory (NSSL), MIT Lincoln Laboratory, and General Dynamics Mission Systems (Stailey and Hondl 2016). The main purpose of this system is to serve as testbed for evaluating the suitability of phased array radar (PAR) technology for weather observations (Zrnić et al., 2007).

One of the major obstacles to the use of PPAR technology for weather surveillance is the calibration needed to achieve measurements comparable to those of the systems using parabolic-reflector antennas (Zrnić et al., 2012). This is due to the existence of significant cross-polar antenna patterns, as well as the scan-dependent measurement biases, inherent to PPAR (Ivić 2018, Fulton et al. 2018). The former induces cross coupling between returns from the horizontally and vertically oriented fields resulting in the biases of polarimetric variable estimates. Furthermore, the inductive and capacitive coupling in hardware is likely to exacerbate the cross-coupling effects.

Pulse-to-pulse phase coding in either the horizontal or vertical ports of the transmission elements has been proposed to mitigate the cross-coupling effects (Zrnić et al., 2014, Ivić 2017a, Ivić 2017b, Ivić 2018a). This approach, however, does not address the scan-dependent system biases in PPAR estimates. These are caused by the horizontal (H) and vertical (V) copolar antenna patterns which vary with beamsteering direction. The effects of these variations must be addressed via corrections using appropriate values at each boresight location. If the cross-coupling effects are sufficiently suppressed with phase coding and given sufficiently narrow antenna main beam, the corrections can be conducted using only the measurements of the copolar patterns (Ivić 2018b). But, the pulse-to-pulse phase coding cross coupling mitigation efficacy is inversely proportional to the cross-polar pattern levels. Thus, at boresight locations where the cross-polar pattern levels are too high the correction using the measurement values of both the copolar and cross-polar patterns needs to be conducted. Furthermore, the effects of active electronic components in transmit and receive paths in PAR systems can result in significant differences between transmit and receive patterns. For these reasons it is important to characterize both transmit as well as receive copolar and cross-polar antenna patterns (Ivić 2019).

The ATD antenna is designed by MIT Lincoln Laboratory (Conway et al., 2013) and uses differential-fed single radiating elements (Bhardwaj and Rahmat-Samii, 2014). The antenna is composed of 76 panels arranged as shown in Fig. 6.2.1. Each panel consists of an 8×8 set of radiating patch-antenna elements with dual linear polarization (H and V), for a total of 4864 elements. This arrangement of antenna elements, spaced by $\lambda/2$, results in a ~4×4 m aperture

[9] Principal Investigators: Igor Ivić and David Schvartzman (CIMMS)

which produces a beam that is ~1.6° wide at broadside. On receive, the antenna is partitioned into overlapped subarrays (consisting of 8 panels each) to produce lower sidelobes and suppress grating lobes outside of the main beam of the subarray pattern (Herd et al, 2005). The operating frequency band of the antenna is 2.7-3.1 GHz.

Here, an overview of the of data correction efforts on the ATD system is presented. Note that the efforts described herein aim at correcting beamsteering biases (i.e., biases relative to a reference point such as broadside) to achieve self-consistency whereby the data bias remains the same for all beamsteering positions (i.e., beamsteering self-consistency). If this is achieved, the ATD calibration reduces to that of a parabolic antenna radar.

Fig. 6.2.1. ATD site and the antenna under the radome.

Data corrections using near-field measurements

Prior to installation in Norman OK, the ATD antenna transmit and receive copolar as well as cross-polar patterns were measured in the near-field (NF) chamber at the MIT-Lincoln Laboratory facilities during March-April 2018 (Conway et al., 2018). The patterns were collected for a total of 2859 electronic beamsteering positions. The beam peaks at all measured locations are shown in Fig. 6.2.2 (left and middle panels). Further, by extracting the copolar beam peaks along the horizontal cardinal plane, the copolar biases for Z, Z_{DR} and ϕ_{DP} are computed and shown in Fig. 6.2.2. (right panels). Note that the biases are scaled to broadside. These measurements may not represent the current state of the array with utmost accuracy since they were obtained about a year prior to the collection of data analyzed here. Further, the ATD antenna was disassembled and reassembled for transportation and installation in Norman, OK. Nevertheless, comparing power outputs of each element during the near-field experiment (April 2018) to those with the ATD system fielded in Norman (May 2019) shows little to no increase in failed elements. Specifically, this comparison indicated 11 and 6 additional transmit elements failures on the horizontal and vertical polarizations, respectively. Thus, given the small change in the state of failed elements in the array, and assuming that the radar is sufficiently stable with time and temperature, the near-field measurements are used herein to correct for the copolar biases.

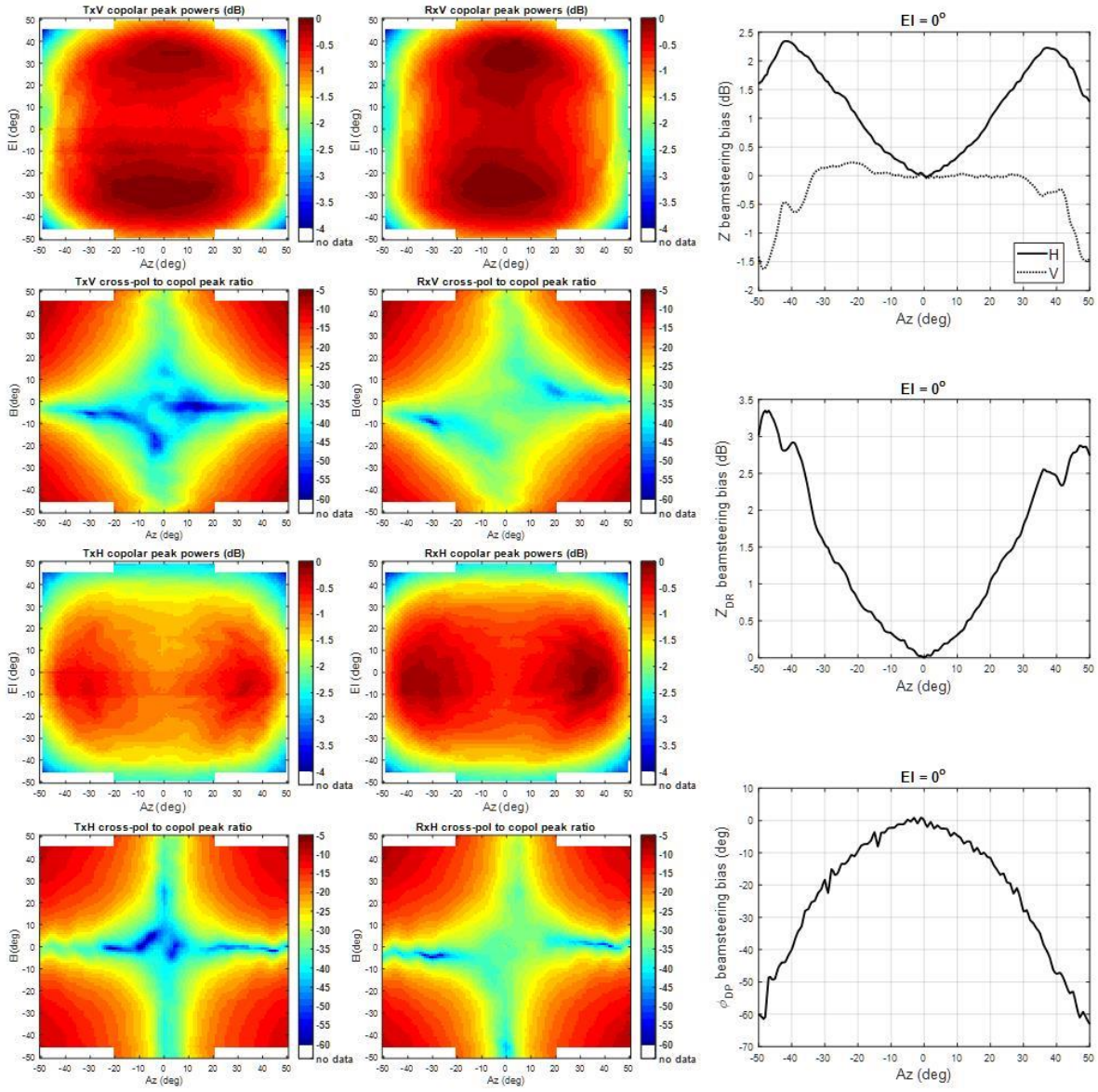

Fig. 6.2.2. Transmit (left panels) and receive (middle panels) beam peak powers of the ATD antenna measured in the near-field chamber. Near-field measured copolar beamsteering biases along horizontal principal plane (right panels).

Note that we used the NF based corrections to mitigate to the system induced biases relative to the broadside while the absolute calibration values were estimated via the comparison with the collocated NEXRAD radars (Ivić and Schvartzman, 2019). The corrections were tested on data sets collected consecutively on August 13, 2019 via three scans, which were shifted by 10° in azimuth at elevation of 0.5°. The overlapping parts of the scans are used to assess the difference in estimated polarimetric variables from collocated volumes illuminated using distinct electronic steering angles (herein referred to as self-consistency). The differences are analyzed when no corrections are applied for the effects of beamsteering and after applying the copolar polarimetric corrections derived from the near-field measurements. The results before and after corrections

are presented in Fig. 6.2.3 and Fig. 6.2.4. Visual comparison of overlapping areas reveals differences in Z_{DR} and ϕ_{DP} among estimates from different scans in Fig. 6.2.3. It is clear that these differences are induced by the system as indicated by the NF measurements (Fig. 6.2.2).

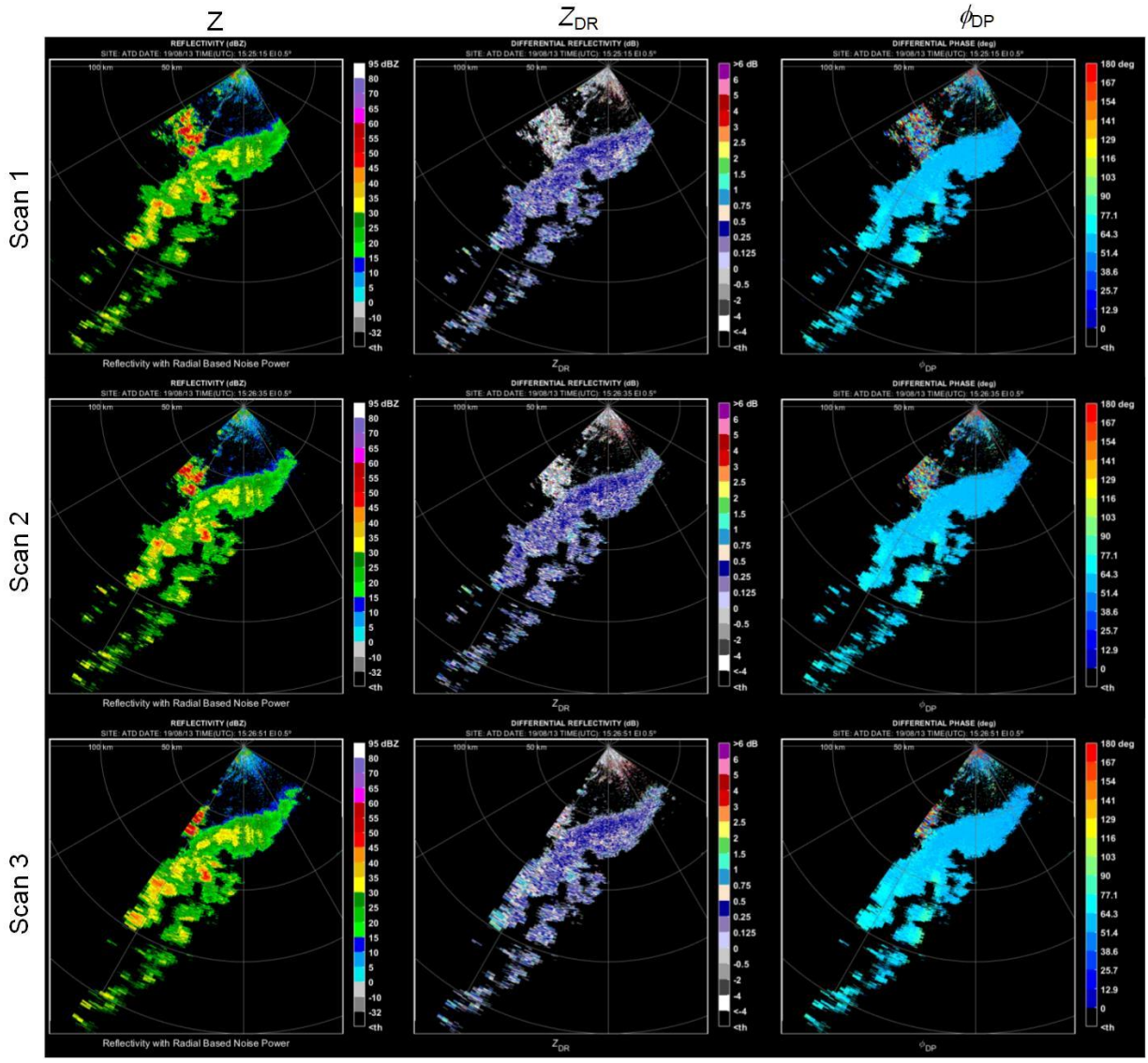

Fig. 6.2.3. Raw non-corrected estimates.

After applying corrections, the differences are visibly reduced as demonstrated in Fig. 6.2.4. The differences at each beamsteering position are averaged in range and shown in Fig. 6.2.5 along with differences computed from NF measurements. The weather obtained results for Z are rather noisy and indicate the span of system induced biases of ~±2 dB (dashed line in the upper left panel) while the NF measurements (grey line in the upper left panel) suggest the span of ~±1 dB. Because, the *Z* color scales in Fig. 6.2.3 and Fig. 6.2.4 are in steps of 5 dB, the system Z biases are not noticeable in the leftmost panels of Fig. 6.2.3. In case of Z_{DR} (upper right panel), the overlap between the NF and weather results is clearly visible for azimuths of about ±25° but

degrades outside this window. This is also corroborated by the weather derived results for the corrected Z_{DR} differences (solid line in the upper right panel) as the fluctuations around zero become larger outside the ±25° interval.

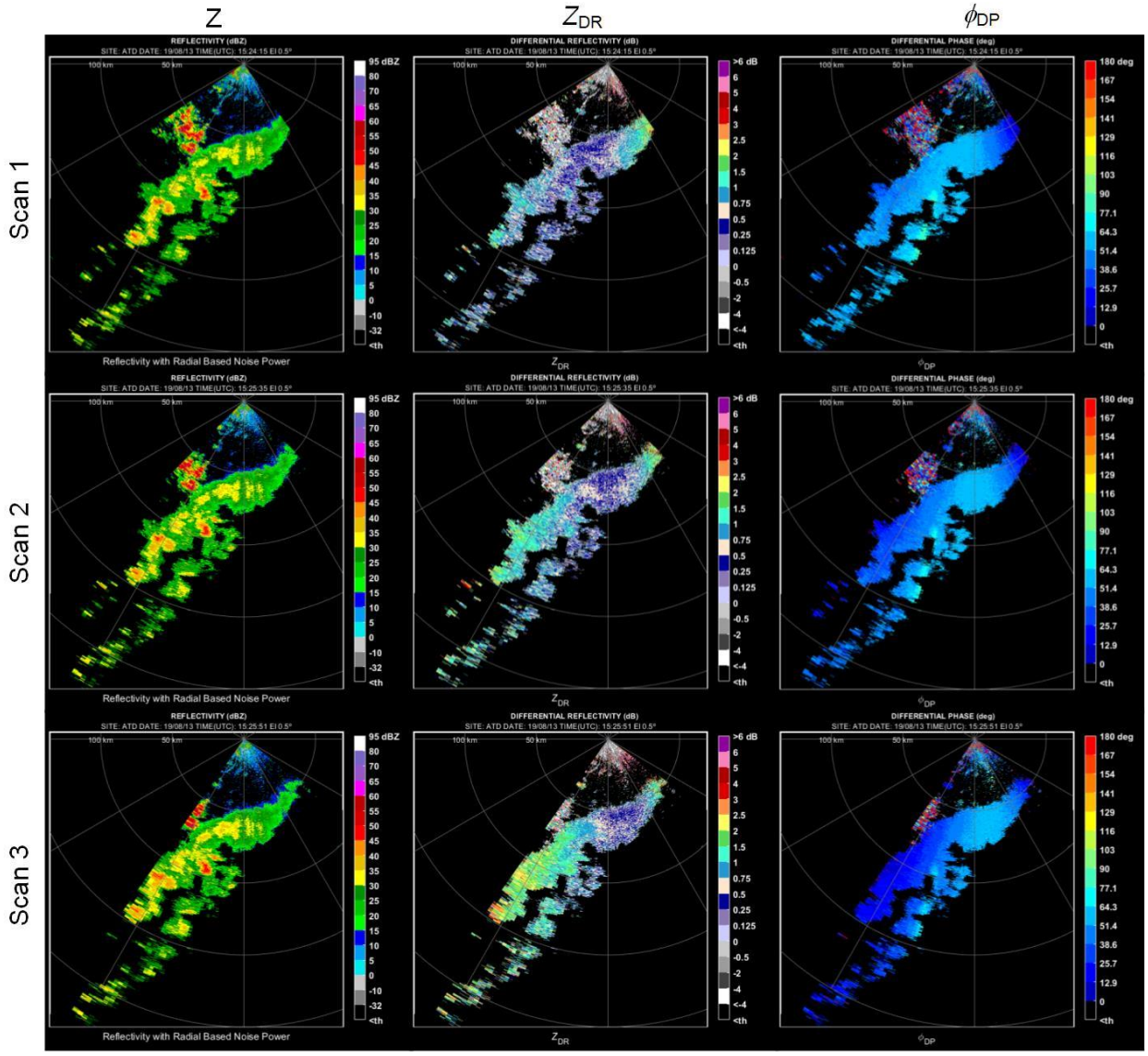

Fig. 6.2.4. Estimates after correction using NF measurements.

The results for ϕ_{DP} (lower left panel), exhibit the best matching between the weather and NF results. Accordingly, the weather derived differences after corrections exhibit relatively small fluctuations around zero over the entire measured interval. In a broader statistical sense, the benefits of Z_{DR} corrections are demonstrated by the histograms of Z_{DR} differences before and after corrections (the lower right panel in Fig. 6.2.5). These show that the histogram before corrections is asymmetric and centered off zero while the histogram after corrections becomes much more symmetric and is centered approximately at zero dB.

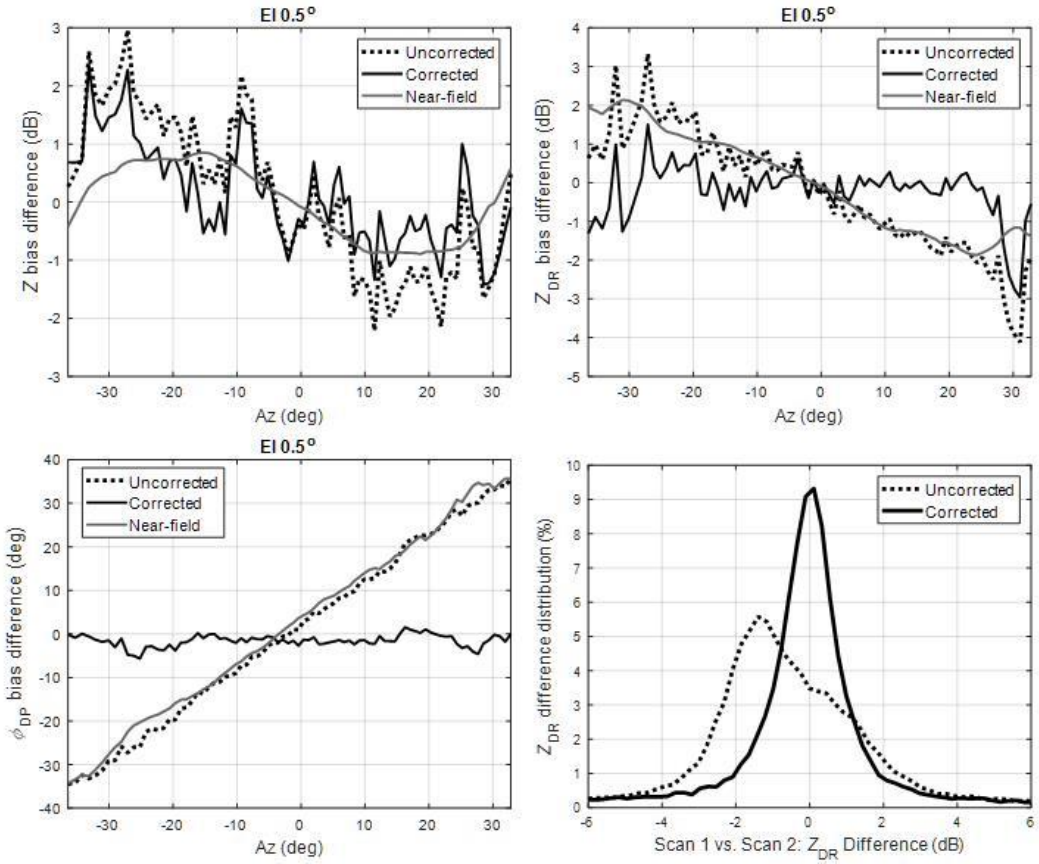

Fig. 6.2.5. Range averaged system induced differences among estimates from collocated volumes illuminated during scans 1 and 3 (upper and lower left panels) as well as histograms of Z_{DR} differences before and after corrections (lower right panel).

The improvement in the broader statistical sense is further illustrated in Fig. 6.2.6 using data that was collected on August 22, 2019. This figure presents two-dimensional histograms (normalized so that the maximum value is one) of Z_{DR} estimates, before and after corrections, for two scans that are separated by 5° in azimuth, where the time between scans is ~29 seconds. Notice that the histogram of uncorrected Z_{DR} estimates exhibits significant spread (from ~1 to 5 dB) while the histogram produced from corrected estimates indicates that the majority of Z_{DR} values in both scans are concentrated at and around 0 dB. This is a clear indication of bias reduction as a result of beamsteering bias corrections. Using ten consecutive weather collections (also collected on August 22, 2019), we further demonstrate the self-consistency improvements by summarizing several histograms of uncorrected and corrected Z_{DR} fields into the boxplot presented in Fig. 6.2.7. The mechanical rotation in azimuth and the average time between consecutive scans are 5°, and 28 seconds (exact time difference shown in the *x*-axis labels). With over 100,000 data points used for each box, this shows the robustness and consistency of the corrections from NF measurements. That is, there are significant differences between the 25^{th}, 50^{th} (median), and 75^{th} percentile values of the uncorrected set of box plots (left panel on Fig. 2.1.7) before and after the rotation.

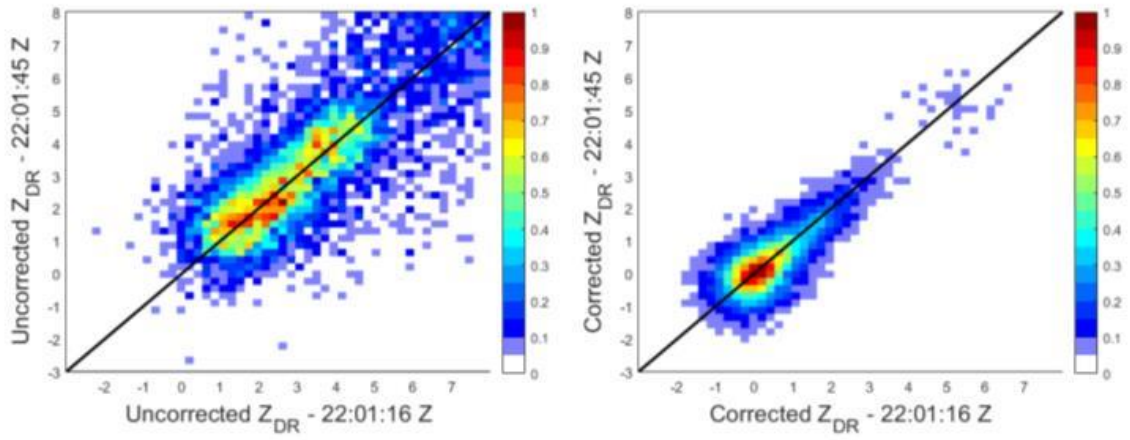

Fig. 6.2.6. Two-dimensional normalized histograms illustrate the dispersion of Z_{DR} estimates between two scans (separated 5º in azimuth and ~29 seconds apart) without corrections (left) and with corrections (right).

Additionally, the median Z_{DR} estimates transition from ~1.8 dB to 2.7 dB in a matter of about five minutes. In contrast, the corrected set of box plots (right panel on Fig. 6.2.7) shows nearly identical statistical properties for fields estimated before and after the rotation, and the median Z_{DR} estimates more reasonably transition from ~0.9 dB to 1.2 dB in about five minutes.

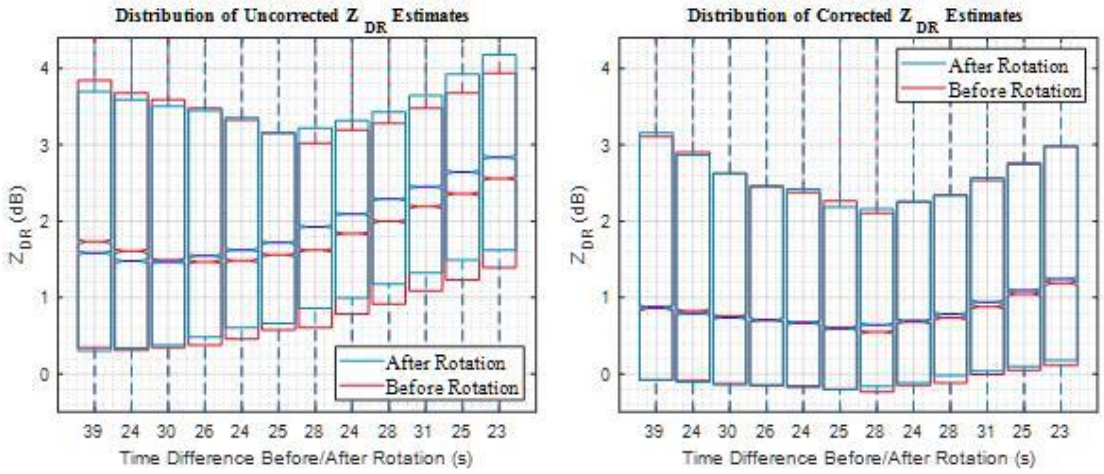

Fig. 6.2.7. Boxplots of uncorrected (left) and corrected (right) fields of Z_{DR} from consecutive weather collections. The mechanical rotation in azimuth between consecutive pairs of scans is of 5 °, and the average time between consecutive scans is 28 seconds (exact time difference shown in the x-axis labels).

Weather calibration using the Calibration Tower

The calibration infrastructure for the ATD includes a 45.7 m far-field calibration tower, located 428 m north of the ATD (Fig. 6.2.8). Atop the tower, an S-band standard gain horn is mounted at the height of ~45 m. It is attached to a motorized platform that allows it to rotate about its axis

and set the horn polarization in horizontal, vertical or any other desired position. This provides for measurements described in Ivić, 2018b. RF-over-fiber links connect the ATD and calibration tower, allowing coherent calibration measurements. A matrix of switches, attenuators, and amplifiers supports the following multiple modes of measurement: (1) remote horn connected to a continuous-wave source for non-coherent receive measurements of the ATD antenna, (2) remote horn connected to the ATD exciter for coherent receive measurements of the ATD antenna, (3) remote horn connected to the ATD receiver for coherent transmit measurements of the ATD antenna, and (4) remote horn connected to a delay line for two-way measurements. Mechanical positioning of the ATD antenna in azimuth and elevation allows measurements at any steering angle, enabling calibration data to be collected for all electronic scan positions of interest. Hence, the antenna can be mechanically placed in such elevation and azimuth position so that when the beam is electronically steered in the direction to be measured, it points towards the horn location. It is unlikely that the antenna positioning with respect to the horn will be perfect so a box scan will be conducted around the assumed horn location to precisely determine the boresight location which points towards the horn and for which the calibration data are to be collected. This will result in a grid of measurement points with non-uniform spacing. Consequently, an interpolation will be applied to produce correction factors where needed. Fig. 6.2.9 illustrates recently collected calibration data.

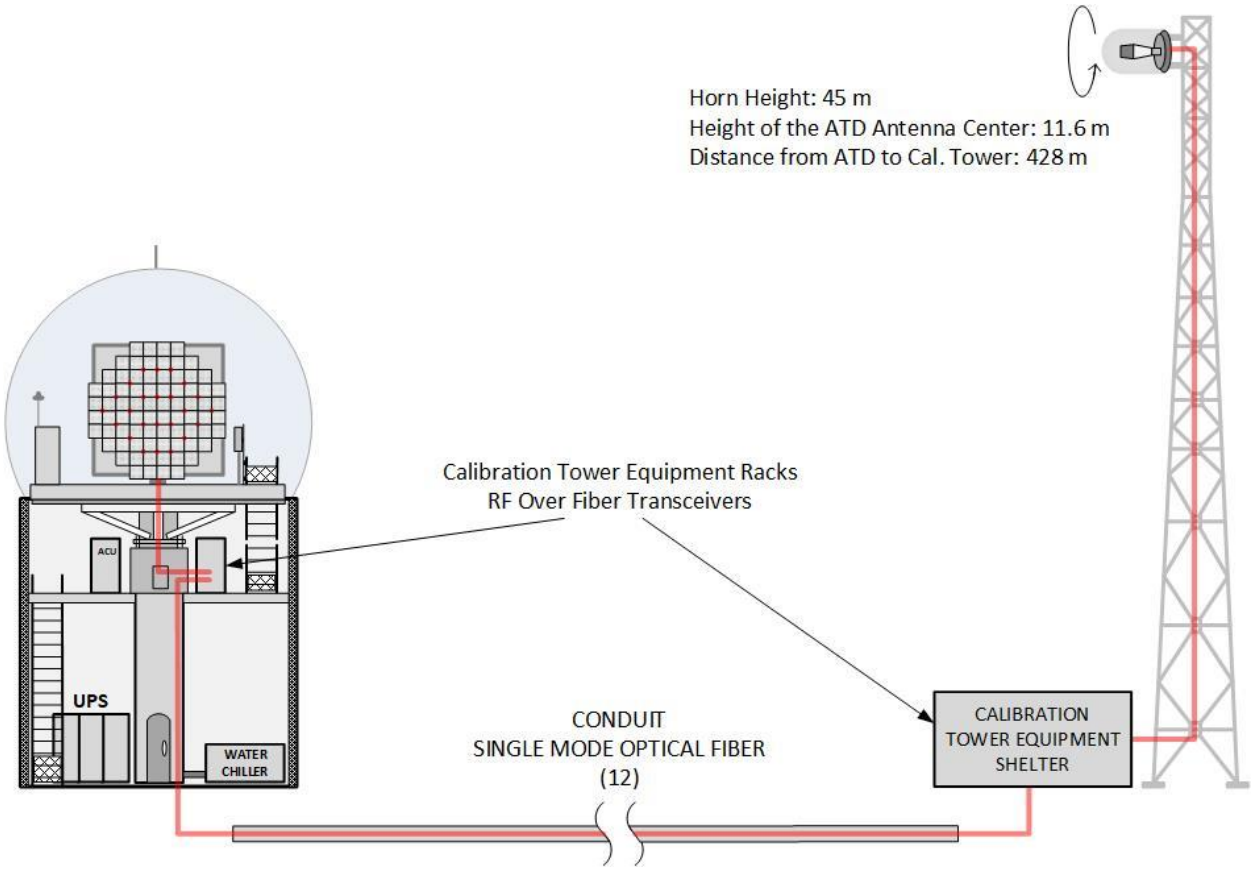

Fig. 6.2.8. ATD calibration infrastructure.

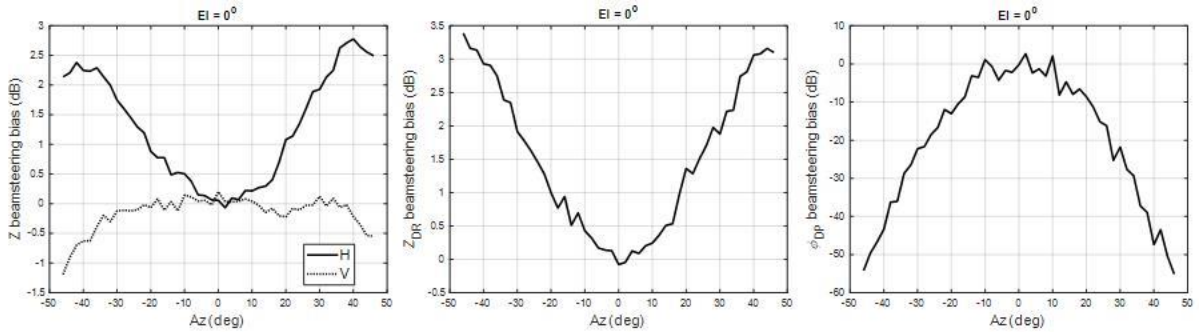

Fig. 6.2.9. An example of Calibration tower measurements. Reflectivity (left panel), differential reflectivity (middle panel), and differential phase (right panel) beamsteering biases.

This infrastructure is currently being developed and integrated into the ATD system and it will be used to obtain accurate far-field (FF) measurements of the fielded array. Accurate measurements of copolar patterns can be used to correct the antenna induced copolar biases in differential reflectivity (Z_{DR}) and phase (ϕ_{DP}) estimates as well as to correct reflectivity (Z) (Doviak and Zrnić, 1993) as the beam is steered away from broadside (assuming the known system calibration constant for Z at broadside). Further, the described infrastructure will be used to characterize the cross-polar ATD antenna patterns. In combination with copolar measurements, these may be used to create the full correction matrices that account for the copolar biases and mitigate the effects of cross coupling at the same time. These matrices may be used for correction at beamsteering locations where the cross-polar patterns are high and the cross coupling suppression via pulse-to-pulse phase coding is insufficient.

Using weather echoes to estimate the self-consistency correction curves

In addition to the efforts described so far, recent research also explored the possibility of using weather returns to estimate the relative self-consistency of correction curves. To produce such estimates, the radar must be able to illuminate collocated volumes using distinct electronic steering angles. This in turn, requires the antenna to be mounted on a pedestal as in ATD.

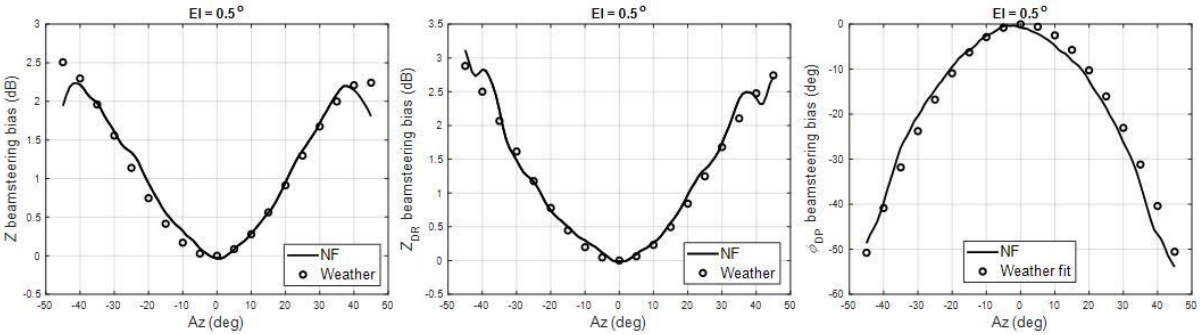

Fig. 6.2.10. Results of using weather echoes to estimate the relative system biases for Z (left panel), Z_{DR} (middle panel), and ϕ_{DP} (right panel).

Given that this is a possible operational architecture, this approach (if feasible) may have practical value. It may be used to validate the existing correction values as well as to aid in the calibration process. An example produced from 10 pairs of ATD scans, where the two scans in each pair are shifted 5° in azimuth with respect to each other, is shown in Fig. 6.2.10.

Conclusion

The weather data correction efforts described here are the first of a kind and have vital importance for the development of PAR technology for weather observations. In that regard, the results of data correction using NF measurements are encouraging because they demonstrate visible improvement in the self-consistency of Z_{DR} and ϕ_{DP} fields. This conclusion is substantiated with statistical results presented in Fig. 6.2.5 – 7. Presented results undeniably demonstrate the benefits of data corrections. This is quite remarkable since the NF measurements were conducted more than a year before data collections and the ATD antenna was disassembled for transportation and reassembled in Norman, OK. Nonetheless, while the NF based corrections exhibit improvements it is unlikely that the applied corrections achieve the beamsteering self-consistency accuracies within the desired limits (e.g., ±0.2 dB for Z_{DR}).

Originally, the intended approach to achieve ATD beamsteering self-consistency and calibration is via Calibration Tower. These efforts are ongoing and have encountered hardware/software issues, equipment instabilities and multipath effects. This is not surprising as Calibration Tower efforts are still in the beginning stage.

A third approach is to use weather echoes to estimate the correction data that achieve beamsteering self-consistency. This method can provide a valid correction data estimates only at beam locations where the effects of cross coupling are small or can be sufficiently suppressed (e.g., using pulse-to-pulse phase coding). This method requires further research to establish its usefulness and accuracy.

In general, it is encouraging that the correction curves produced using the three methods are all comparable. However, it is yet to be established whether the corrections that achieve accuracies within desired limits are achievable.

References

Bhardwaj, S., and Y. Rahmat-Samii, 2014: Revisiting the generation of cross-polarization in rectangular patch antennas: A near-field approach. *IEEE Antennas Propag. Mag.*, **56**, 14–38, doi:https://doi.org/10.1109/MAP.2014.6821758.

Conway, D., J. Herd, M. Fosberry, M. Harger, C. Weigand, M. Yeary, and K. Hondl, 2013: On the development of a tileable LRU for the nextgen surveillance and weather radar capability program. *2013 IEEE International Symposium on Phased Array Systems and Technology*, IEEE, 490–493, doi:https://doi.org/10.1109/ARRAY.2013.6731877.

Conway, M. D., D. Du Russel, A. Morris, and C. Parry, 2018: Multifunction phased array radar advanced technology demonstrator nearfield test results. *Proc. of the IEEE,* doi: https://doi.org/10.1109/RADAR.2018.8378771

Doviak, R. J., and D. S. Zrnić, 1993: *Doppler Radar and Weather Observations*. Academic Press, 562 pp.

Fulton, C., J. Salazar, D. Zrnić, D. Mirković, I. Ivić, and D. Doviak, 2018: Polarimetric Phased Array Calibration for Large-Scale Multi-Mission Radar Applications, *IEEE Radar Conference (RadarConf18)* doi: https://doi.org/10.1109/RADAR.2018.8378746

Herd, J. S., S. M. Duffy, and H. Steyskal, 2005: Design considerations and results for an overlapped subarray radar antenna. Preprints, *IEEE Aerospace Conf.*, Big Sky, MT, doi: http://dx.doi.org/10.1109/AERO.2005.1559399

Ivić, I. R., and R. J. Doviak, 2016: Evaluation of phase coding to mitigate differential reflectivity bias in polarimetric PAR. *IEEE Trans. Geosci. Remote Sens.*, **54**, 431–451, doi:https://doi.org/10.1109/TGRS.2015.2459047

Ivić, I. R., 2017a: Phase Code to Mitigate the Copolar Correlation Coefficient Bias in PPAR Weather Radar. *IEEE Trans. Geosci. Remote Sensing*, *GE-55(**4**)*, 2144-2166, doi: https://doi.org/10.1109/TGRS.2016.2637720

Ivić, I. R., 2017b: An experimental evaluation of phase coding to mitigate the cross-coupling biases in PPAR. *Preprints 38th International Conference on Radar Meteorology,* Chicago, IL.

Ivić, I. R., 2018: Options for Polarimetric Variable Measurements on the MPAR Advanced Technology Demonstrator, *IEEE Radar Conference (RadarConf18)*, doi: https://doi.org/10.1109/RADAR.2018.8378544

Ivić, I. R., 2018a: Effects of Phase Coding on Doppler Spectra in PPAR Weather Radar. *IEEE Trans. Geosci. Remote Sensing*, *GE-56(**4**)*, 2043 – 2065, doi: https://doi.org/10.1109/TGRS.2017.2772962

Ivić, I.R., 2018b: On the Use of Horn Antenna to Calibrate the MPAR Advanced Technology Demonstrator. *10th European Conference on Radar in Meteorology and Hydrology*, Wageningen, Netherlands.

Ivić, I. R., 2019: Facets of Planar Polarimetric Phased Array Radar Use for Weather Observations. *AMS 99th Annual Meeting,* Phoenix, AZ.

Ivić, I. R., and D. Schvartzman 2019: A first look at the ATD data corrections. Preprints, *39th International Conference on Radar Meteorology*, Nara, Japan. Amer. Meteor. Soc., Paper 2-06.

Stailey, J. E., and K. D. Hondl, 2016: Multifunction phased array radar for aircraft and weather surveillance. *Proc. IEEE*, **104**, 649–659, doi: https://doi.org/10.1109/JPROC.2015.2491179.

Zrnić, D. S., and Coauthors, 2007: Agile-beam phased array radar for weather observations. *Bull. Amer. Meteor. Soc.*, **88**, 1753–1766, https://doi.org/10.1175/BAMS-88-11-1753.

Zrnić, D. S., V. M. Melnikov, and R. J. Doviak, 2012: Issues and challenges for polarimetric measurement of weather with an agile beam phased array radar. NOAA/NSSL Rep., 119 pp. [Available online:http://www.nssl.noaa.gov/publications/mpar_reports/]

Zrnić, D.S., R.J. Doviak, V.M. Melnikov, and I.R. Ivić, 2014: Signal Design to Suppress Coupling in the Polarimetric Phased Array Radar. *J. Atmos. Oceanic Technol.*, **31**, 1063–1077, https://doi.org/10.1175/JTECH-D-13-00037.1.

6.3 Mutual Coupling and UAV Far-Field Probe[10]

SENSR phased array polarimetric calibration research has focused on advancing the state-of-the-art for calibrating large scale phased array radar: this includes corrections as a function of scan angle, temperature and other environmental variables. This work built on algorithms and concepts that were developed in the past, but still have not been demonstrated on large-scale systems. In order to calibrate a dual-pol phased array for the weather mission, the polarization characteristics of the main beam peak (at a minimum) must be known precisely, for both transmission and reception, at every scan angle of interest. Various algorithms (matrix inversion, product correction, etc.) have been previously described that make use of this information to correct for inevitable geometrically- and electromagnetically-induced biases dual polarization variable estimates.

This section briefly introduces SENSR calibration research conducted by OU's Advanced Radar Research Center (ARRC). Details are provided in the accompanying full report. Our work has focused on implementation and performance evaluation of different algorithms based on mutual coupling calibration process. Since the all-digital Horus demonstrator is still in development, a conventional 8x8 active array antenna has been used as a test bed platform. Results and error analysis indicate the mutual coupling calibration process is a robust in-situ method to calibrate a phased array system. Details of this proposed technique and results are discusses in the full report.

To validate the calibration procedures in a real environment, a UAV platform that carries an active RF dual-polarized RF probe was proposed and is almost ready for final validation. This novel UAV-RF platform was designed and fully characterized to guarantee that aerodynamic behavior during fly mode does not affect dual-polarization measurements. Extensive electromagnetic scattering/interference analysis between the UAV platform and probe, in addition to precise position control of the UAV, were required to guarantee accurate dual-pol calibration procedure.

During the first year of SENSR funded research our team developed the UAV platform hardware and necessary CEM numerical simulations. These enabled us to evaluate the electromagnetic field interaction of the UAV platform and the RF antenna probe, guaranteeing high cross-polarization isolation. This past year our team focused on experimental characterization in the near- and far-field of the UAV platform with RF probe for different scenarios. Two outdoor field antenna patterns measurements completed recently shows the UAV based method is an excellent candidate for in-situ radar pattern test. Details and recent results are provided in our full report.

[10] Principal Investigators: Caleb Fulton and Jorge Salazar (OU ARRC)

7. Cylindrical Polarimetric Phased Array (CPPAR) [11]

Introduction

After a decade of study, it has been realized that it is challenging to develop a high-performance polarimetric phased array radar (PPAR) to make accurate weather measurements (Zhang et al. 2008&2009; Zrnic et al. 2011; Lei et al. 2013& 2015; Stailey and Handl 2016). The challenges particularly apply to a 2D electronic scan planar PPAR, because of the change in beam characteristics and cross-pol coupling when the beam steers off the broadside. To avoid the beam-dependent calibration needed for a planar array, a cylindrical polarimetric phased array radar (CPPAR) was proposed for future weather measurements (Zhang et al. 2011). With support from NOAA/NSSL and OU/ARRC, the CPPAR demonstrator was designed and developed (Zhang et al. 2013, Karimkashi et al. 2013, Kelly et al. 2013, Karimkashi and Zhang 2015). Preliminary test results revealed issues of the CPPAR demonstrator in beam mismatch and electronics instability (Fulton et al. 2017, Byrd et al. 2017). In collaboration with NSSL, we have rebuilt the CPPAR demonstrator to provide a more stable system. Major accomplishments include: i) CPPAR rebuild, ii) system characterization and calibration, iii) initial weather measurements, and iv) the design and development of the 12x12 reconfigurable array antennas.

CPPAR system rebuild

As shown in Fig. 7.1, CPPAR rebuild includes the following:

- Electronics Design/Fabrication/Test
- Antenna Production/Testing/Installation
- Mechanical design and construction
- Software development and test
- Test Plan/Far-Field Transceiver mounted at NWC

[11] Principal Investigator: Guifu Zhang (OU ARRC)

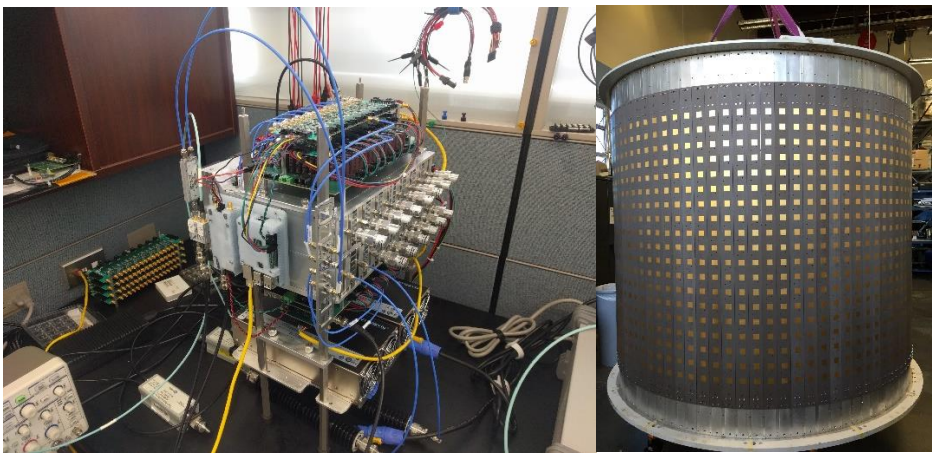

Figure 7.1: (a) 16-channel electronics and (b) A picture of CPPAR with antenna installed

After initial testing on the ground, CPPAR was moved to the rooftop of the Radar Innovations Laboratory (RIL) building on March 6th 2019. The following picture was taken during the operation.

Figure 7.2: A picture of CPPAR being installed on the top of RIL

System characterization and calibration

After CPPAR was deployed at the rooftop of RIL, the embedded element patterns of the CPPAR columns were re-measured, as shown in Fig.7.3. The calibration horn height was adjusted based on the CPPAR beam pointing angle at 2.76 GHz. Using the modified particle swarm optimization (Golbon et al 2018), a set of beamforming weights are found according to the measured active element patterns and then applied to the CPPAR to achieve more accurate active and beam radiation patterns.

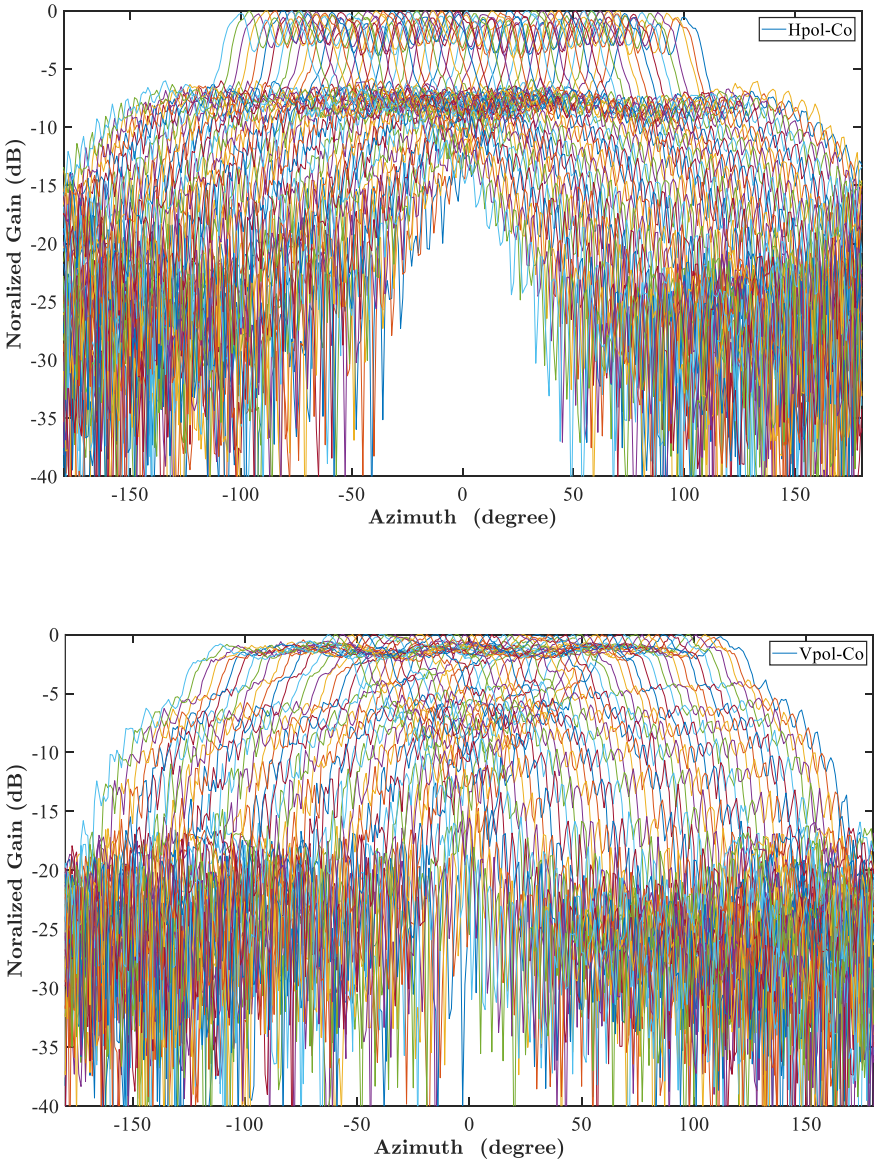

Figure 7.3: CPPAR active element patterns for horizontal polarization (top) and vertical polarization (bottom).

Figure 7.4 shows the optimized CPPAR beam pattern measured in the transmitting mode.

As shown in the figure, the sidelobe level for both polarizations is better than -28 dB, and the horizontal and vertical polarizations cross-polarization level is less than -37 dB. Also noted is that the polarization patterns are matched, especially in the main beam areas.

Similarly, all 25 commutating CPPAR beam patterns are formed from the 180° sector and measured. It was shown that a similar radiating pattern can be obtained while commutating scanning in the azimuth.

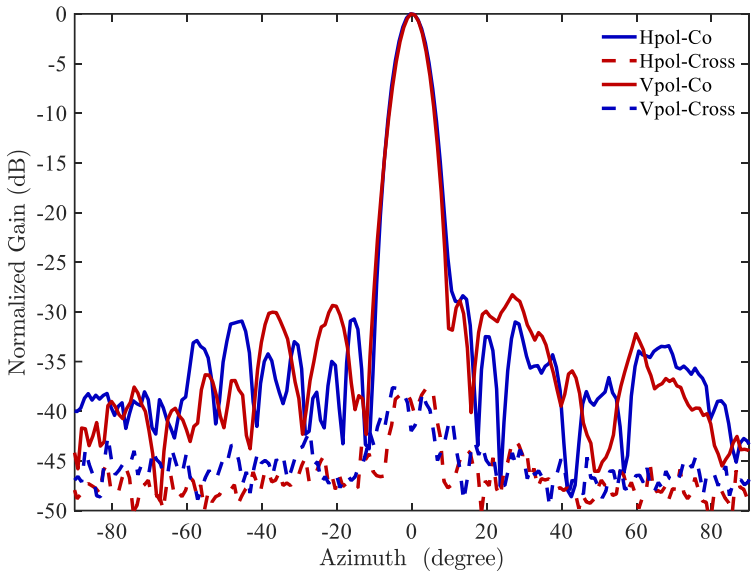

Figure. 7.4 CPPAR horizontal and vertical polarization beam pattern comparison in the transmit mode.

To further characterize CPPAR performance, the 2-D radiation pattern was measured with the CPPAR operating in the receiving mode due to the limited frequency band. Assuming that the horn antenna radiation pattern will not significantly change within ±12 degrees along the elevation direction, by changing the CPPAR operating frequency, the radiation pattern of CPPAR at different elevation angles can be approximately measured. The pseudo 2-D (3-D) radiation pattern of CPPAR is presented in Fig. 7.5. As shown in the figure, the cross polarization level in the entire measured volume is below -40 dB for both polarizations.

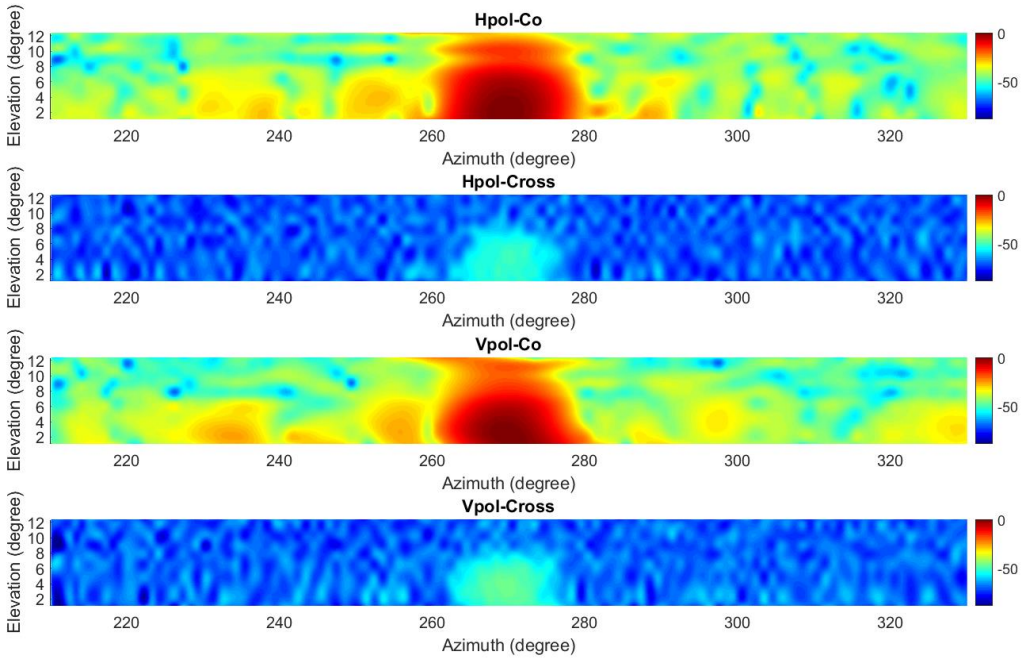

Figure 7.5: CPPAR pseudo 2-D radiation pattern.

Initial weather measurements were made during the summer of 2019 (Li et al. 2019). Polarimetric radar data of reflectivity (Z_H), radial velocity (v_r), spectrum width (σ_v), differential reflectivity(Z_{DR}), copolar correlation coefficient (ρ_{hv}), and differential phase (ϕ_{DP}) in a convective precipitation case are presented in Fig. 7.6. For qualitative comparison, observations from the nearby KTLX are also shown in Fig. 7.6 as reference. As can be seen, the CPPAR electronic scan produces visually almost the same measurements as its mechanical scan. Moreover, CPPAR measurements are generally consistent with KTLX observations except for the difference in resolution. It should be noted that the difference in v_r and ϕ_{DP} measurements is because the resolution volumes in precipitation are seen by CPPAR and KTLX from different radial directions. Furthermore, CPPAR produces higher estimates of σ_v due to its wider beam which illuminates more weather scatterers in motion. Please see more detailed analysis of errors/differences in Li et al. (2019).

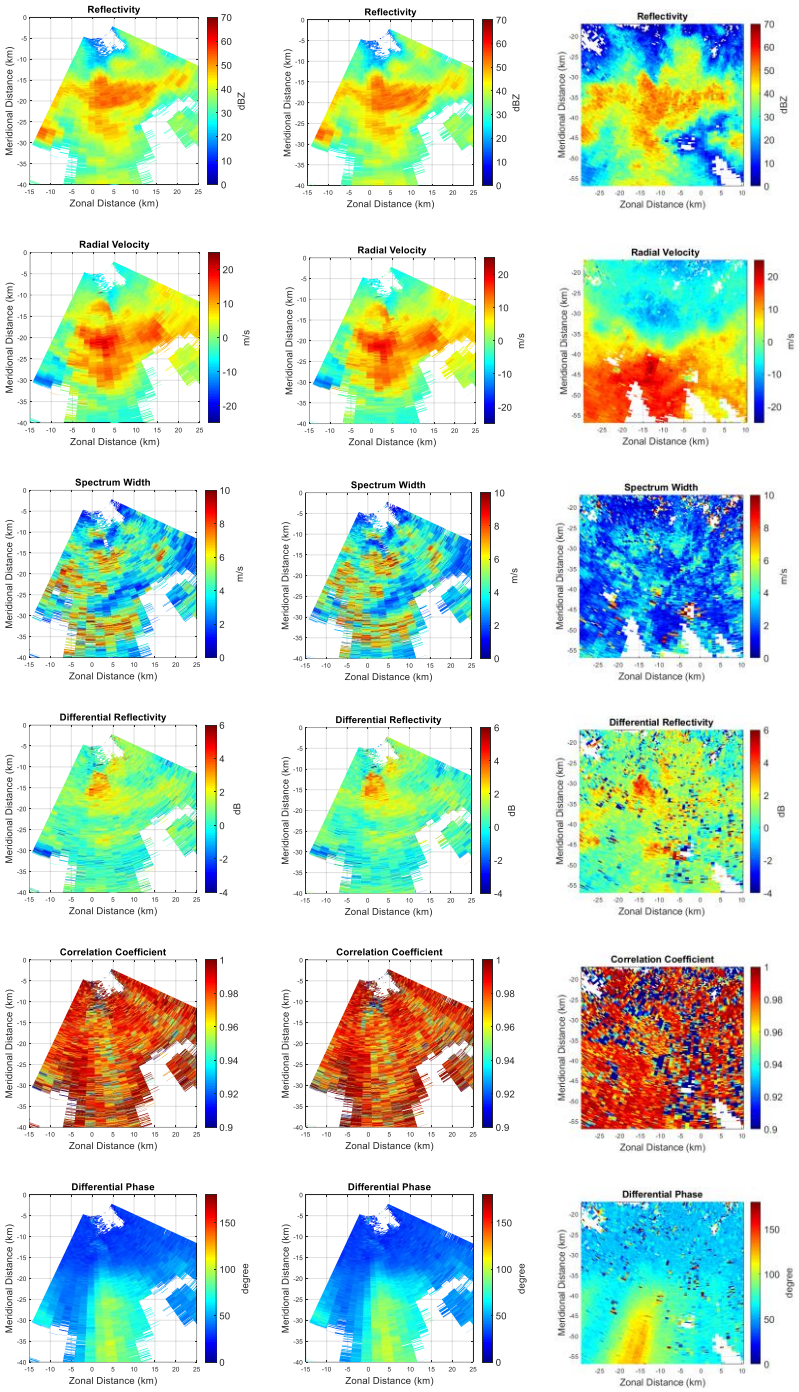

Figure 7.6. Weather measurements collected with CPPAR (SNR≥5dB) and KTLX on 27 August 2019. Left column: CPPAR mechanical scan at 05:03:40 UTC; middle column: CPPAR electronic scan at 05:04:04 UTC; right column: KTLX mechanical scan at 05:06:10 UTC.

From the CPPAR initial experiments and data, we learned that

i) High accuracy of polarimetric weather measurements is feasible with the CPPAR without complicated calibration;

ii) Creeping wave is not a big issue for a large scale CPPAR to make accurate weather measurements (Golbon et al. 2019), and

iii) Polarization purity and azimuthally scan-invariant beams can be achieved, along with accurate polarimetric measurements of weather (Li et al. 2019).

Design and development of the 12x12 reconfigurable arrays

For future research and development of PPAR for weather measurements, high-performance radiating elements and array configurations are needed. The high-perfroamce crossed dipole antenna had been designed and manufactured (Mirmozafari et al. 2018&2019). Three different array antenna configurations as shown in Fig. 7.7 have been designed, developed, and set up in RIL anechoic chamber and their radiation patterns are being measured using the Unit Excitation Active Element Pattern (UEAEP) method. In this method, the radiation pattern of each element is measured while all other elements were terminated. All mutual coupling effects are completely accounted for, including the possibility of scan blindnesses. The amplitude and phase of all measured active element patterns are imported into Matlab and the required phase shift between elements is applied to steer the array radiation pattern.

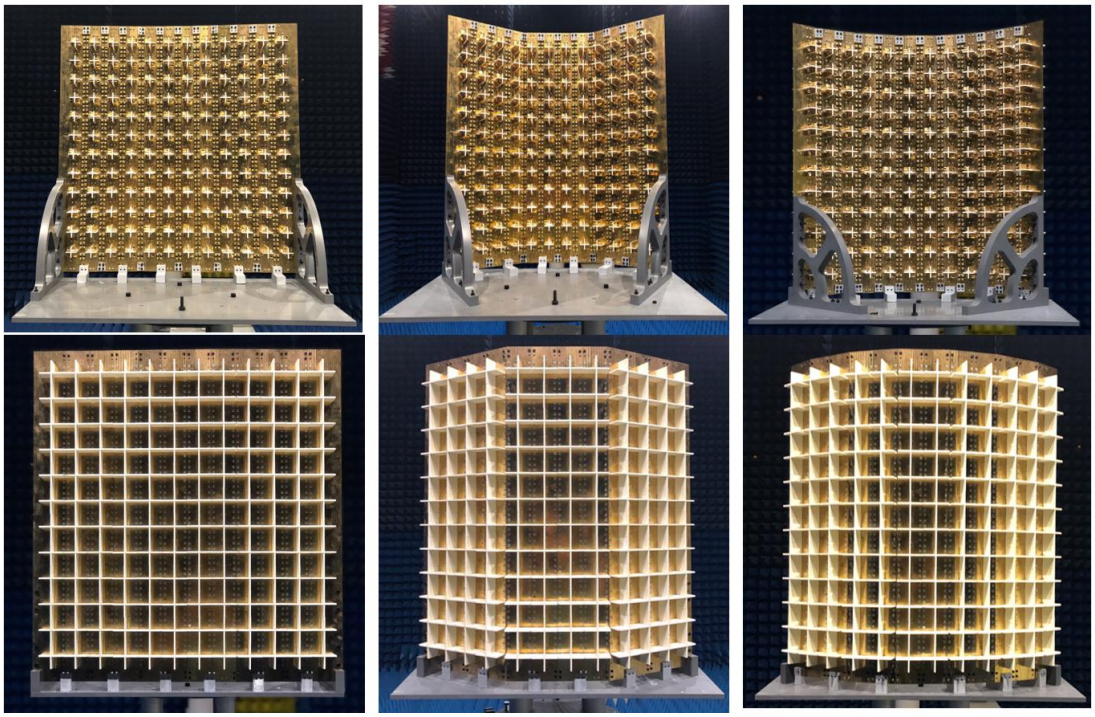

Planar configuration **Multifaceted configuration** **Cylindrical configuration**

Figure 7.7. Fabricated 12x12-element array antenna different configurations being set up in RIL anechoic chamber .

The active element radiation patterns of the center 8 elements of the multifaceted configuration are shown in Fig. 7.8. These radiation patterns belong to the two middle rows of the center facet. The next step is combining the active element patterns and applying the required phase shift between elements to calculate the measured antenna radiation pattern at different steering angles. Continuous testing is to be conducted. As shown in Golbon et al. (2019), the dipole antenna has advantages in developing PPAR with high purity of polarization over patch radiating elements.

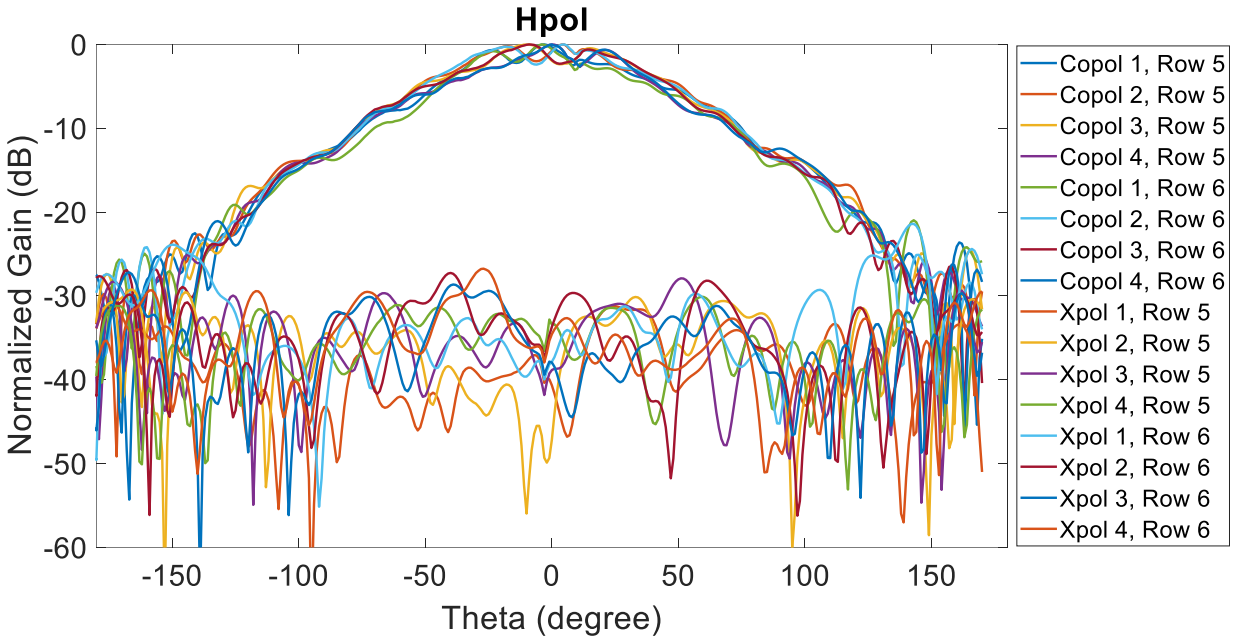

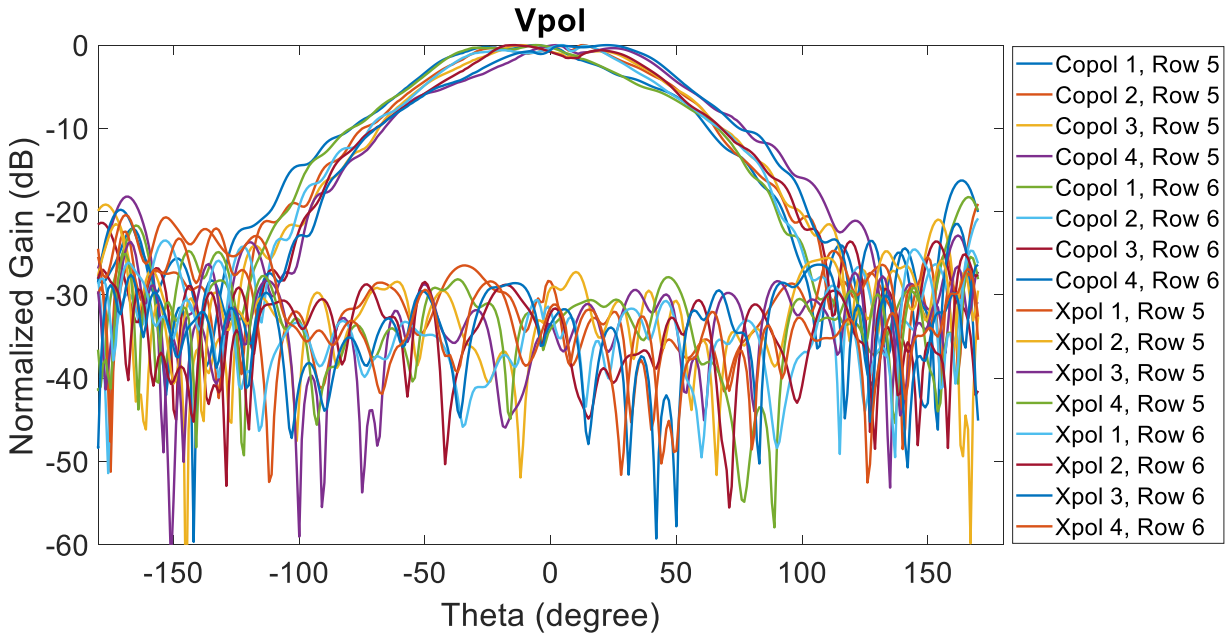

Figure 7.8. Measured horizontal (top) and vertical (bottom) polarization active element radiation patterns of the 8 central elements of the fabricated 12x12-element array antenna in the multifaceted configuration.

References:

Byrd, A., C. Fulton, R. Palmer, S. Islam, D. Zrnic, R. Doviak, R. Zhang and G. Zhang, 2017: First weather observations with a cylindrical polarimetric phased array radar, Internal report.

Fulton, C., Salazar, J. L., Zhang, Y., Zhang, G., Kelly, R., Meier, J., McCord, M., Schmidt, D., Byrd, A. D., Bhowmik, L. M., Karimkashi, S., Zrnic, D. S., Doviak, R. J., Zahrai, A., Yeary, M., Palmer, R. D. (2017). Cylindrical Polarimetric Phased Array Radar: Beamforming and Calibration for Weather Applications. *IEEE Transactions On Geoscience And Remote Sensing*, **55**(5), 2827-2841.

Golbon-Haghighi, M.-H., Saeidi-Manesh, H., Zhang, G., Zhang, Y., 2018: Pattern Synthesis for the Cylindrical Polarimetric Phased Array Radar (CPPAR).*Progress In Electromagnetics Research M, 66*, 87-98.

Golbon-Haghighi, M.-H., M. Mirmozafari, H. Saeidi-Manesh, G. Zhang, 2019: Pattern Synthesis for Cylindrical Phased Array Antennas with Dual-polarized Patch and Dipole Elements, *IEEE Transactions On Antennas And Propagation, submitted*.

Karimkashi, S., G. Zhang, R. Kelley, J. Meier, R. Palmer, A. Zahrai, R. J. Doviak, and D. S. Zrnic, Cylindrical Polarimetric Phased Array Radar: Design and Analysis of a Frequency Scanning Antenna Array 2013 IEEE International Symposium on Phased Array Systems & Technology, Boston, 2013.

Karimkashi, S., and G. Zhang, 2015: Optimizing radiation patterns of a cylindrical polarimetric phased-array radar for multi-missions, *IEEE Trans. On Geoscience and Remote Sensing* **53**(5), 2810-2818

Kelly, R., J. Meier, S. Karimkashi, M. McCord, G. Zhang, R. Palmer, A. Zahrai, R. J. Doviak, D. S. Zrnic, Cylindrical Polarimetric Phased Array Radar: Hardware Design and Mobile Demonstrator, IEEE International Symposium on Phased Array Systems & Technology, Boston, 2013

Lei, L., G. Zhang, R. Doviak, and S. Karimkashi, 2015: Comparision of theoretical biases in estimating polarimetric properties of precipitation with weather radar using parabolic reflector, or planar and cylindrical arrays, *IEEE Trans. On Geosci*. Remote Sensing, **53**(8), 4313-4327.

Li, Z., G. Zhang, G., M.-H. Golbon-Haghighi, H. Saeidi-Manesh, Matthew Herndon, and Hong Pan , 2019: Initial Observations with Electronic and Mechanical Scans Using a Cylindrical Polarimetric Phased Array Radar. *IEEE Transactions On Geoscience And Remote Sensing*, conditionally accepted.

Mirmozafari, M., Zhang, G., Fulton, C., Doviak, R. J. (2019). Dual-Polarization Antennas With High Isolation and Polarization Purity A review and comparison of cross-coupling mechanisms. *IEEE Antennas and Propagation Magazine, 61*(1), 50-63. 10.1109/MAP.2018.2883032.

Mirmozafari, M., H. Saeidi-Manesh, G. Zhang (2018). Highly isolated crossed dipole antenna with matched copolar beams, *Electronics Letters* **54** (8), 470-472

Saeidi-Manesh, H., G. Zhang, 2017: Cross-polarisation suppression in cylindrical array antenna, *Electronics Letters* 53 (9), 577-578

Saeidi-Manesh, H., G. Zhang, 2017: Characterization and Optimization of Cylindrical Polarimetric Array Antenna, *Progress In Electromagnetics Research* 158, 49-61

Saeidi-Manesh, H., G. Zhang, 2019: Challenges and Limitations of the Cross-Polarization Suppression in Dual-Polarization Antenna Arrays using Identical Subarrays, *IEEE Trans. On Antenna and Propagation,* Accepted

Stailey, J.E., and Hondl, K.D. 2016: Multifunction phased array radar for aircraft and weather surveillance, *Proc. IEEE*, **104**(3), 649–659.

Zhang, G., R. J. Doviak, D.S. Zrnic, and J. E. Crain, "A calibration algorithm for phased array radar polarimetry" OU Intellectual Property Disclosure (#09NOR005), 28 July 2008.

Zhang, G., R. J. Doviak, D. S. Zrnic, J. E. Crain, D. Staiman, and Y. Al-Rashid, 2009: Phased array radar polarimetry for weather sensing: A theoretical formulation for polarization calibration. *IEEE Trans. on Geoscience and Remote Sensing*, **47**(11), 3679-3689

Zhang, G., R. J. Doviak, D. S. Zrnic, R. D. Palmer, L. Lei, Y. Al-Rashid, 2011: Polarimetric Phased Array Radar for Weather Measurement: A Planar or Cylindrical Configuration? *J. Atmos. Ocean. Tech.*, **28**(1), 63-73,

Zhang, G., S. Karimkashi, L. Lei, R. Kelley, J. Meier, R. Palmer, C. Futon, R. Doviak, A. Zahrai, and D. Zrnic, Cylindrical Polarimetric Phased Array Radar Concept: A Path to Multi-mission Capability, IEEE International Symposium on Phased Array Systems & Technology, Boston, 2013

Zrnic, D.S., G. Zhang, and R. J. Doviak, 2011: Bias Correction and Doppler Measurement for Polarimetric Phased Array Radar, *IEEE Trans. on Geoscience and Remote Sensing*, **40**(2), 843-853,

8. All Digital Phased Array Demonstration[12]

Introduction & Motivation

Sampling of existing mechanically scanning weather radars is insufficient to capture the four-dimensional evolution of atmospheric dynamics and microphysics, especially in severe weather scenarios. The scientific community and the federal government have shown intense interest in the development of rapid-scanning polarimetric radars, which is possible with phased array radar technology. In order to meet the desired update rates and polarimetric quality, however, it is expected that a fully digital phased array architecture will be necessary. In fact, it may be the best way to effectively (and continuously) calibrate dual polarization on a phased array radar via mutual coupling. In addition, all-digital arrays inherently have high dynamic range since noise from separate elements is uncorrelated, allowing simultaneous observations of low-reflectivity clear-air echoes and high-reflectivity/clutter regions, for example. The flexibility of an all-digital phased array radar would also allow a variety of beam-scanning strategies, some of which are shown in the figure below, and may be necessary to achieve the desired temporal resolution.

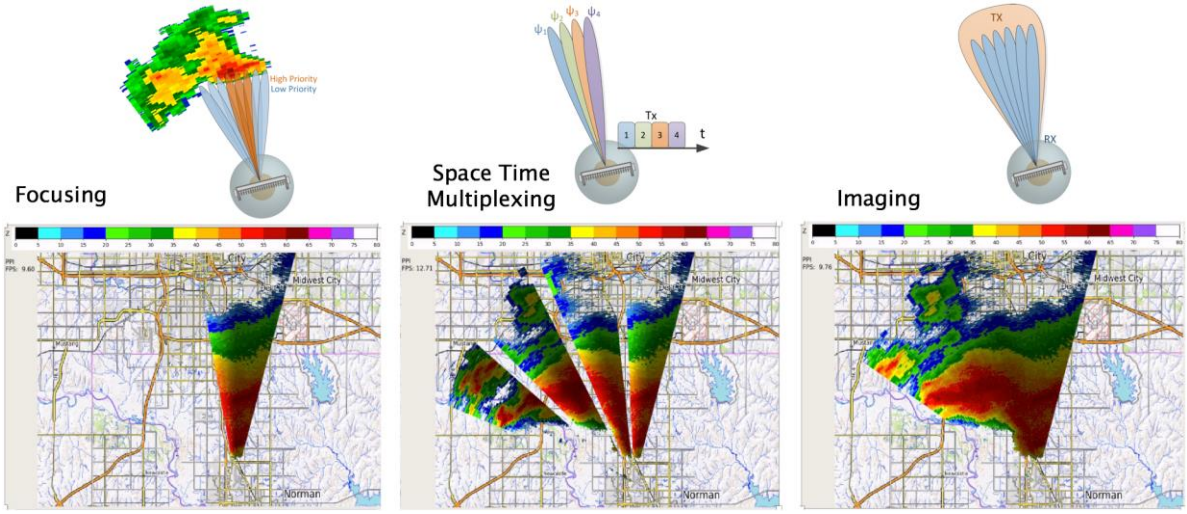

Just as important, an all-digital radar architecture would potentially save millions in O&M lifecycle costs. Over the expected 30-year lifespan of such a system, new missions and capabilities would be possible via software upgrades rather than costly hardware redesigns (e.g., analog subarray beamforming network) and deployment across the entire network. Finally, digital phased array radars would leverage decades of telecom industry investment in digital technology further driving down system costs.

For these reasons, and based largely on NOAA SENSR funding, the Advanced Radar Research Center (ARRC) at the University of Oklahoma (OU) is working with NOAA's National Severe Storms Laboratory (NSSL) on the development of a digital-at-every-element, S-band, dual-pol phased array radar. The mobile demonstrator is called "Horus" after the Egyptian god of war

[12] Principal Investigators: Robert Palmer, Caleb Fulton, Jorge, Salazar, Hjalti Sigmarsson and Mark Yeary (OU ARRC)

and sky. With an aperture of approximately 1.63 m, the Horus radar will have 1024 (32x32) dual-pol channels and will be capable of extreme flexibility in terms of array segmentation, channel-independent waveforms, adaptive beamforming, etc.

Horus Overview

The initial conceptual design of the Horus demonstrator is shown in the figure below. Each of the 2x1024 channels will produce more than 10 W of peak power on transmit and will support a duty cycle of 10%, thus providing a sensitivity of approximately 12.5 dBZ at 50 km. Though its limited size means that the S-band Horus radar does not provide the angular resolution typically expected from a forecast-quality weather radar, it is extremely scalable and will serve as an engineering testbed for next-generation weather radars. Given the importance of radar polarimetry to the weather community, its most-important feature will be the capability of performing real-time, frequent array and polarimetric adaptive calibration as a routine part of the Horus scanning strategy. By exploiting mutual coupling between individual radiating elements that make up the array and the waveform independence of an all-digital array, the ARRC is currently developing automatic algorithms for array/polarimetric calibration. The system will be based on a slat/brick design for the majority of the electronics; hence, the electronic modules will be line replaceable for simplification of routine maintenance. These electronics include the RF front-ends, commercial-off-the-shelf (COTS) transceivers, and on-board FPGA processing. This functionality will be combined into a single so-called "OctoBlade" composed of 16 highly compact and functional channels. Each OctoBlade will include liquid cooling that is facilitated via a cold plate, also known as a heat transport duct (as briefly discussed in the next section). The dual-polarization patch antenna that has been specifically designed for Horus has extremely high polarimetric isolation (better than -40 dB), which is enhanced further by the design of the isolated RF channels that are connected to each element of the antenna. Although the system is extremely flexible, if desired to reduce data size, partial systolic beamforming will be possible with the on-board FPGAs. Data transfer will be handled with a high-speed RapidIO network, since the team has vast experience with this mature technology. Below is the current

timeline for the completion of the system, which should be available for the 2021 spring storm season.

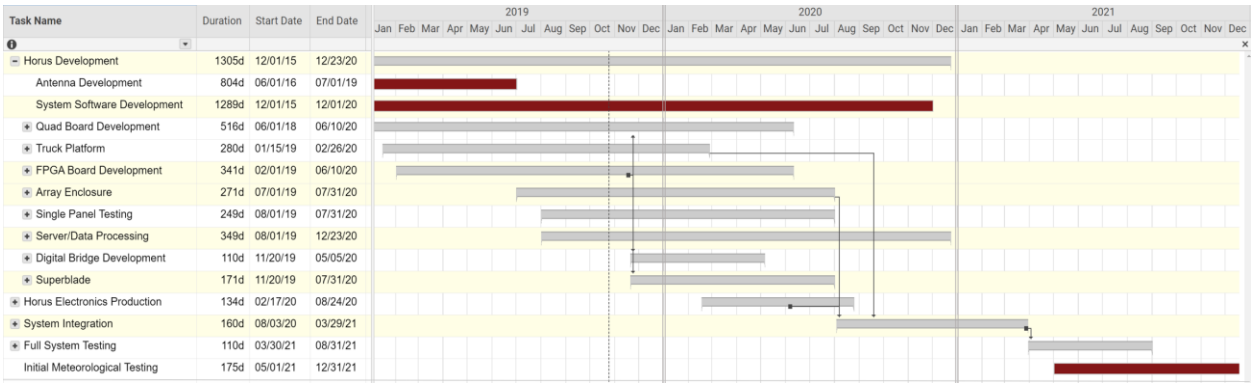

Task Name	Duration	Start Date	End Date
Horus Development	1305d	12/01/15	12/23/20
Antenna Development	804d	06/01/16	07/01/19
System Software Development	1289d	12/01/15	12/01/20
Quad Board Development	516d	06/01/18	06/10/20
Truck Platform	280d	01/15/19	02/26/20
FPGA Board Development	341d	02/01/19	06/10/20
Array Enclosure	271d	07/01/19	07/31/20
Single Panel Testing	249d	08/01/19	07/31/20
Server/Data Processing	349d	08/01/19	12/23/20
Digital Bridge Development	110d	11/20/19	05/05/20
Superblade	171d	11/20/19	07/31/20
Horus Electronics Production	134d	02/17/20	08/24/20
System Integration	160d	08/03/20	03/29/21
Full System Testing	110d	03/30/21	08/31/21
Initial Meteorological Testing	175d	05/01/21	12/31/21

Status of Horus Development

The all-digital Horus demonstrator can be broken into several major subsystems, which are shown in the figure below. The OctoBlade with its heat-transport duct is shown in the left panel, with the 8x8 panel shown in the center panel. The completed truck and positioner are shown in the right panel, along with a rendering of the full antenna array. A summary of the progress over the course of the SENSR funding is given below for each of these subsystems.

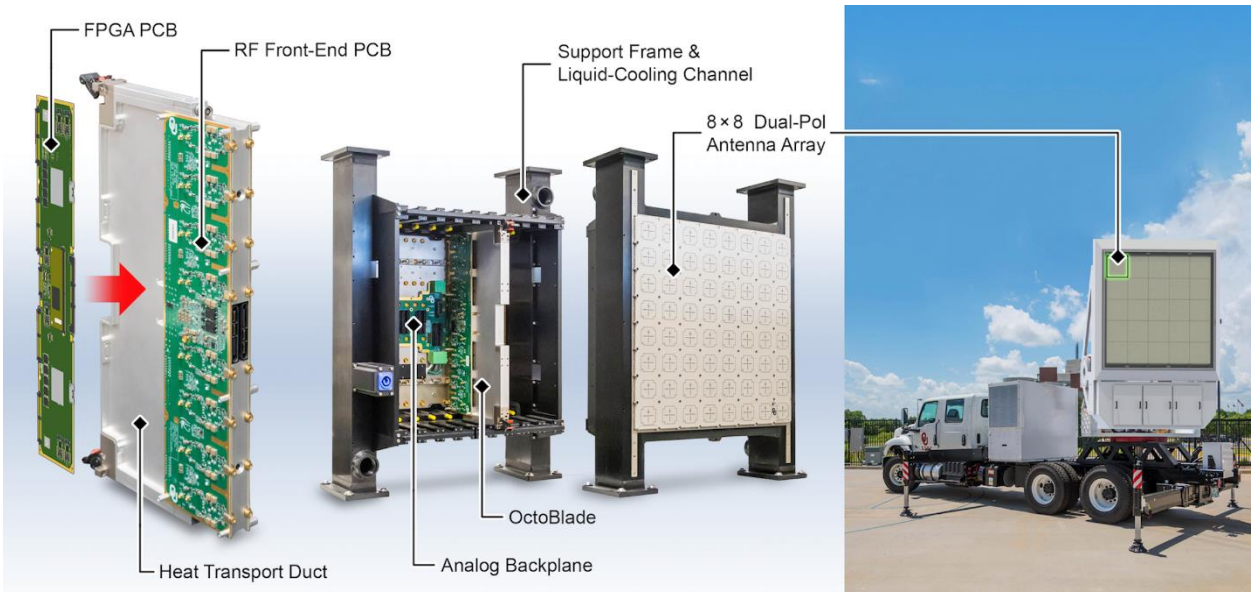

Electronics (OctoBlade, SuperBlade, Digital Bridge)

The OctoBlade is a 16-channel, RF-to-digital transceiver, and makes up the heart of the Horus radar. The other major electronics components are the SuperBlade (power, control) and the Digital Bridge (RapidIO). The major electronics of the OctoBlade are contained within the team's Quad board and FPGA board. The Quad board design is essentially complete now, reaching a mature testing phase. Several loop-back tests have confirmed this board's efficacy. However, some minor design changes may be needed to ensure compatibility with the FPGA board, which should be completed by early 2020. With this interoperability constraint, it is expected to complete the Quad/FPGA board combination by mid-2020 with immediate production runs at that time. The current state of the layout of the PCBs is provided below. The Quad board and FPGA board are on the top and bottom, respectively. From these renderings, it is easy to see how the two boards will mate. Note that an OctoBlade has two Quad boards and two FPGA boards on each side of the heat-transport duct.

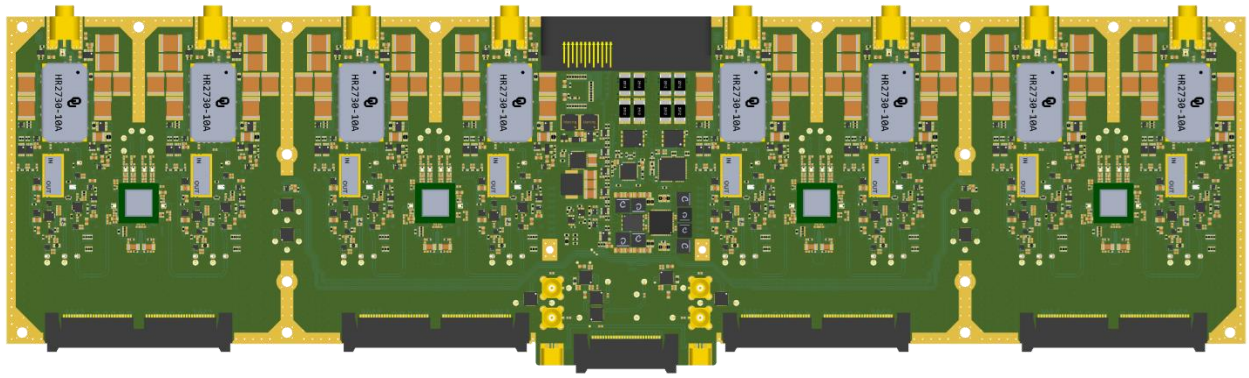

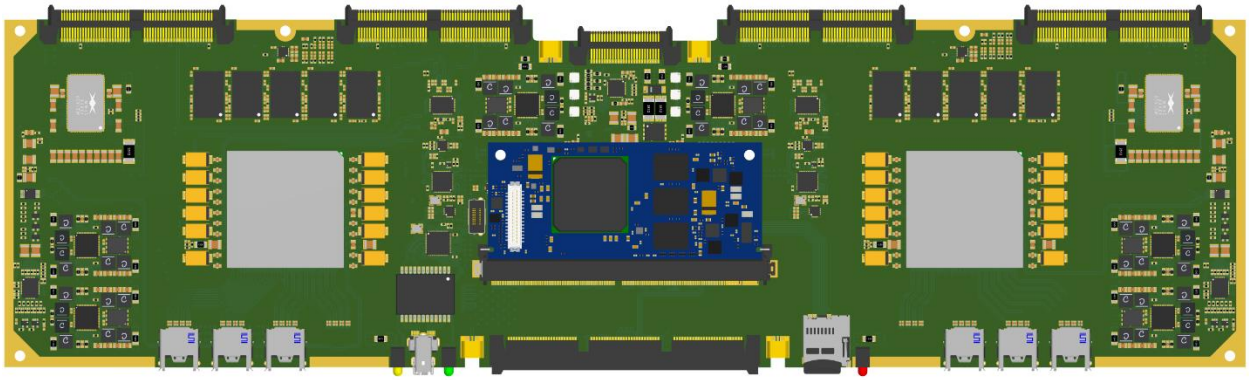

In terms of loopback testing: Digital control at the subarray and element levels allows the quality of data received by radars to be enhanced using methods like adaptive digital beamforming (ADBF), which mitigates interference and clutter for the cost of a little computation. To achieve maximum performance, ADBF algorithms require precise steering,

meaning that the channels must be well matched; this may require use of an equalizer on the IQ data. Consequently, this was confirmed via a digital loopback experiment. In brief, a 500-microsecond chirp spanning 124 MHz was passed through a prototype Horus receiver and the signals at the outputs of the four channels were collected, after being mixed down to baseband, at a sampling frequency of 125 MHz. There was noticeable channel mismatch throughout the bandwidth; the Fourier transforms of the signals at the receiver input and at each receiver channel's output are shown in the figure below. Digital equalization was performed using a least mean squares method. Because the input signal to the receiver was available and had good behavior across the spectrum, it was used as the reference signal for the equalization calculation. The Fourier transforms of the signals before and after equalization using a 128-tap equalization filter can be seen in the figure. With equalization using 128 filter coefficients, the signals matched the reference signal very well. The channel pair cancellation ratio (CPCR) was the metric that was used here to assess the quality of the channel matching. Note that under this definition, a higher CPCR means that better cancellation has been achieved.

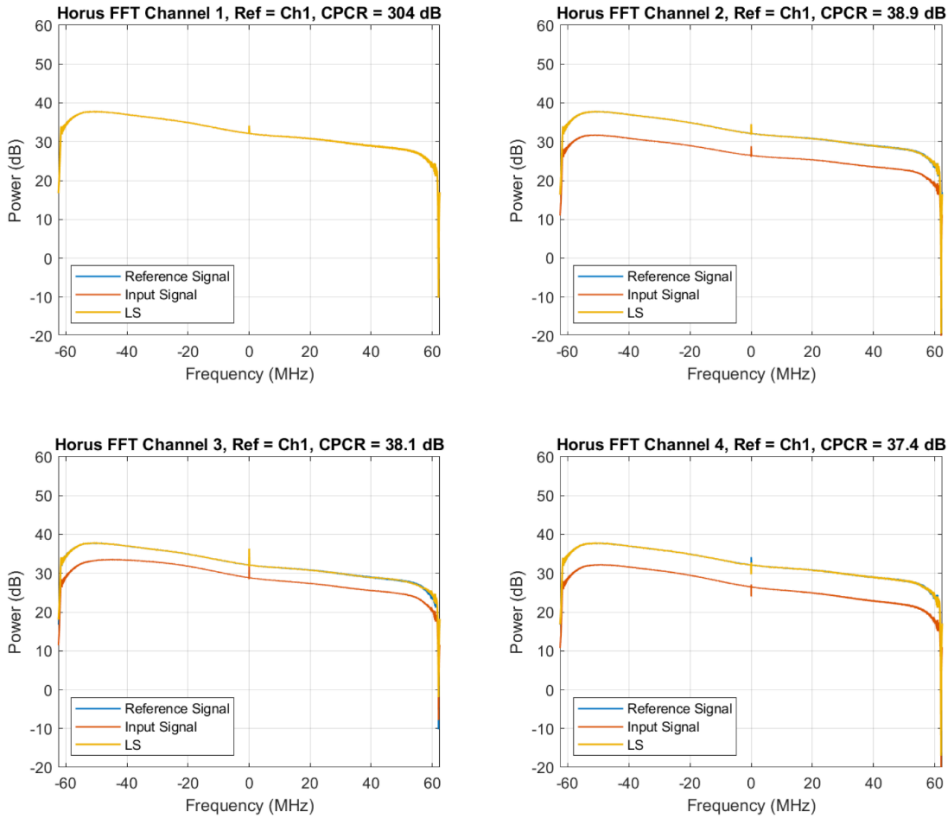

The next figure illustrates the benefit of a well calibrated array.

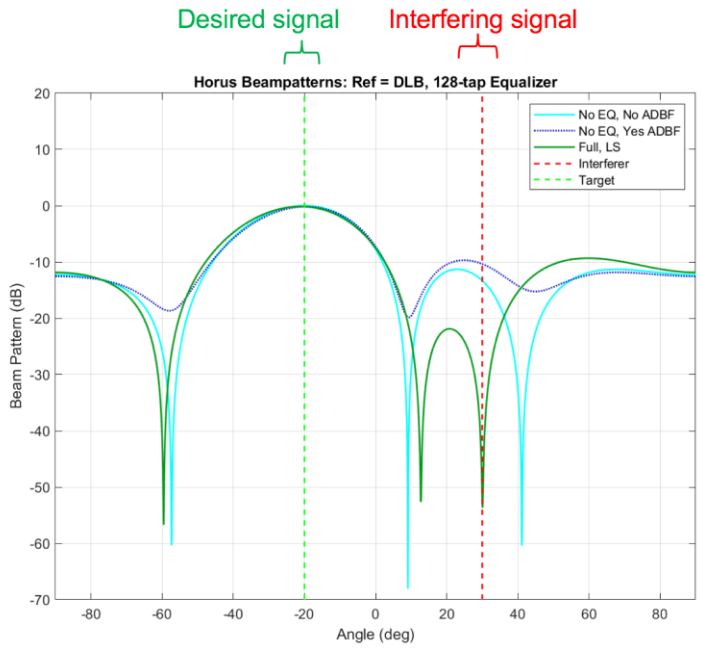

Planning for the digital bridge architecture has also commenced with the design to be completed by May 2020. The general functionality of the digital bridge includes:

- Reference clock distribution to 2 OctoBlades
- Trigger distribution to 2 OctoBlades
- Debug interface via JTAG (single chain across 2 OctoBlades)
- SMBus interface for access to onboard peripherals and power management
- Access to hardwire control signals (power enable, power good, write protect, reset)
- Derives power from 4 FPGA boards (load shared)
- TX/RX RF local oscillator distribution to 2 OctoBlades

The SuperBlade is currently under design, and will include the following features:

- Reference clock distribution to 4 digital bridges
- Trigger distribution to 4 digital bridges
- Panel-level controller based on MitySOM with ethernet communication interface.
- TX/RX RF local oscillator distribution to 4 digital bridges
- Standalone copper-to-fiber launch points for long inter-panel SRIO links

- Panel-level conversion of high voltage DC (400V) from Analog Bridge down to +50V and +12V and back into Analog Bridge.
- Communication with panel-level power system via SuperBlade control/data board

Mechanical (Truck, Positioner, Chiller, PTO, etc.)

The Horus truck not only provides transport for the radar, but also (1) provides prime power through the power take-off (PTO) unit, (2) supports the chiller unit for the liquid cooling of the array electronics, (3) supports the positioner, and (4) houses the rotary joint and various computing facilities. In total, the mechanical systems of the Horus radar represent a fully contained mobile radar system, which will facilitate field demonstrations, comparative observations with other systems, and will generally be convenient for transport of the system.

As shown to the right, the truck w/levelers, chiller, PTO, positioner, and rotary joint are complete. The array frame, which supports the OctoBlades and liquid cooling manifolds, will be integrated with the truck by March 2020. A photograph of the current state of the transport system is provided below, along with a mechanically accurate rendering of the array support structure.

Antenna/Filter Design & Fabrication

The fully digital active and dual-pol phased array antenna was designed for full control of transmitted and returned signals of each antenna element. The antenna design was focused on achieving the same or improved performance compared to WSR-88D parabolic antennas. Dual-polarized radars require both low cross-polarization levels (better than -40 dB) and well-matched patterns (lower than 0.1 dB) to successfully determine the polarimetric variables of the scanned atmosphere sector.

In general, when the cross-polarization levels of the antenna increase, all the biases in the polarimetric variables are increased. Multiple factors in the antenna element were investigated during the design process of the 8x8 array, and these factors included: edge diffraction suppression; bandwidth in excess of 10% with a central frequency of 2.8 GHz; port-to-port isolation in the element on the order of -50 dB; cross polarization levels below -40 dB and co-polar mismatch below 0.1 dB at ± 60^o and ± 10^o for scanning range at the azimuth and elevation planes, respectively, after careful calibration; and active reflection coefficient of at least -10 dB at ± 60^o and ± 10^o for scanning range at the azimuth and elevation planes, respectively. Consequently, a new stacked cross microstrip patch radiator with electromagnetic coupling was developed for Horus. An 8x8 antenna panel, along with extensive measurements taken in OU's anechoic chambers, are shown in the figure below. The radiators and the feeding network were separated into two different assemblies to prevent them from bending after fabrication. The radiator assembly consists of two conducting layers and a radome of RT/Duroid 5880LZ bonded with RO4450F.

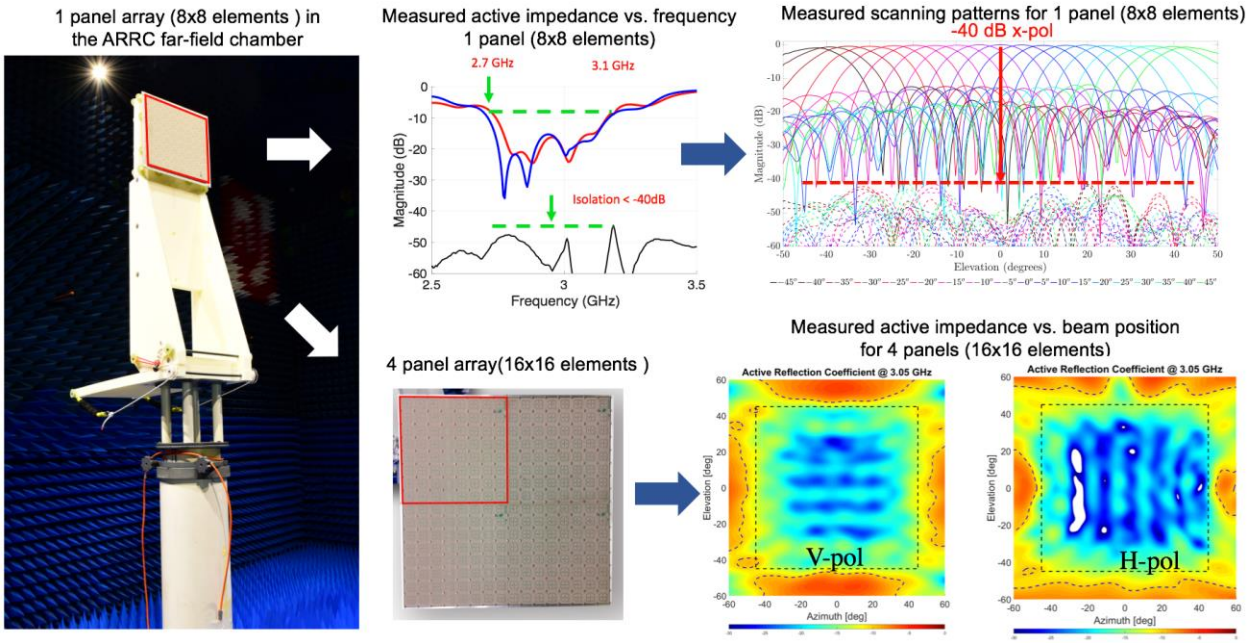

Modern day and next-generation radars, such as the Horus demonstrator, are challenged to operate in complex, dynamic environments as demand for precious spectrum continues to grow. For instance, the desire for resilient systems that can adapt to and counter new sources of interference across the spectrum is a common theme in any radar modernization strategy. Consequently, in order to mitigate interference, the integration of miniaturized filters, both static

and frequency reconfigurable, into the antenna panels has been investigated in parallel with the antenna development. These filters are based on capacitively-loaded, substrate-integrated waveguide (SIW) resonators that are completely integrated into the feeding network assembly. The static filters provide added out-of-band rejection, and the reconfigurable filters can be used to achieve in-band interference rejection, both of which may prove important for all-digital radars.

Software

The Horus demonstrator is an all-digital polarimetric radar exploiting the latest in COTS digital transceiver technology. As such, software is an integral and extremely important "subsystem" of the radar. During the SENSR project, software for the Horus radar has been a concentration area while waiting for the final design of the OctoBlade and supporting hardware subsystems. The figure below shows a general overview of the various levels of software development needed for the system. The lowest level of software exists on the OctoBlades themselves and controls the basic functionality of the radar, including up/down conversion, transmit/receive waveforms and data transport using the RapidIO protocol. The next level of code exists on the control/data servers, which interfaces the network connection with the OctoBlades and has the important role of data/command routing and ethernet communication. The highest level of code will be implemented on standard computers and will allow command execution, data display, etc. At this point, the basic functionality of a rudimentary digital radar is operational on our benchtop evaluation OctoBlade. By the end of 2020, this code will be fully ported to the final OctoBlade design and further features will continue to be developed for field operations.

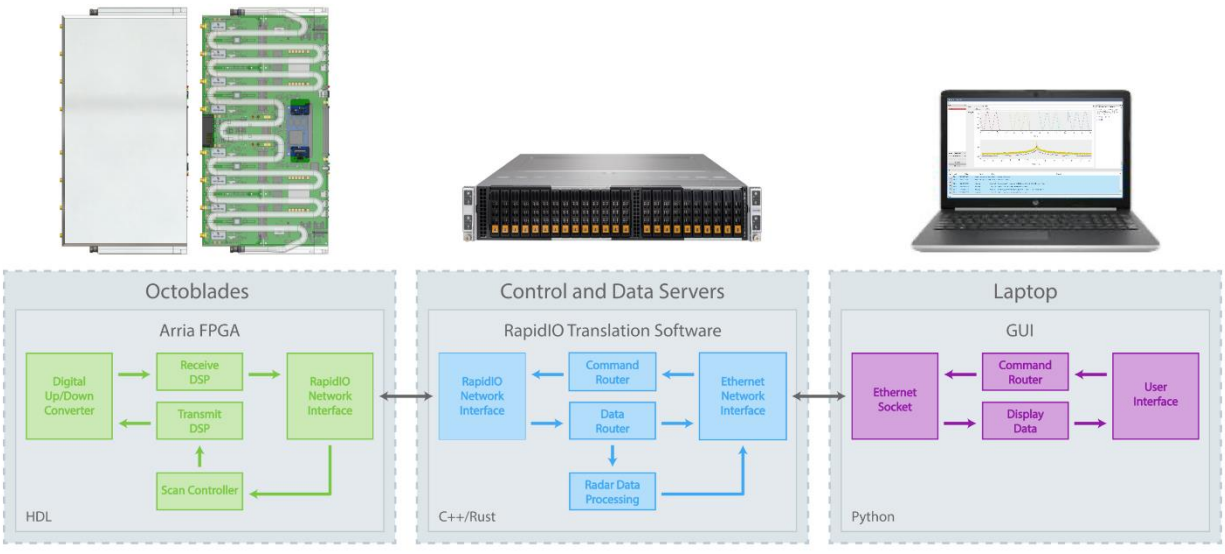

Plans for the Horus Demonstrator

The calendar year of 2020 will be an important year for the development of the Horus demonstrator. Previous funding is sufficient for the hardware and development costs for completion of the radar to a basic operational level. The system should be nearing completion by the end of 2020 with final integration and testing occurring in early 2021. In consultation with our NSSL colleagues, we plan to expand the fundamental research efforts with a concentration on topics directly related to the Horus all-digital demonstrator. Likely topics of interest will be the demonstration of mutual-coupling base calibration, implementation of various beam-scanning strategies and waveform designs. Working closely with the ARRC engineering team, these development topics will be led by students who will be co-advised by ARRC and NSSL/CIMMS researchers, thereby deepening the OU-NOAA collaboration while providing a mechanism for all to become more familiar with the all-digital Horus demonstrator. As a longer-term plan, OU leadership would like to discuss the desire for an ATD-scale Horus demonstrator, which could be constructed as a separate facility or as a replacement of the current subarray-based ATD.

Resulting Publications

1. C. Fulton, M. Yeary, D. Thompson, J. Lake, and A. Mitchell. "Digital phased arrays: Challenges and opportunities." Proceedings of the IEEE 104, no. 3, 487-503, 2016.
2. C. Fulton, R. Palmer, J. Salazar, H. Sigmarsson, “Updates on the All-Digital Dual-Polarization Phased Array Radar (Horus),” AMS Radar Conference, Chicago, IL, 2017.
3. M. Yeary, C. Fulton, R. Palmer, J. Salazar, H. Sigmarsson, “Update on the All-Digital Phased Array Radar Horus Program at the Advanced Radar Research Center at OU,” Government Microcircuit Applications & Critical Technology Conference (GOMAC), pp. 1-4, March 2018.
4. J. Diaz, J. Salazar-Cerreno, J. Ortiz, N. Aboserwal, R. Lebron, C. Fulton, and R. Palmer, “A cross-stacked radiating antenna with enhanced scanning performance for digital beamforming multifunction phased-array radars,” IEEE Trans. on Antennas and Propagation, vol. 66, no. 10, pp. 5258–5267, 2018.
5. S. Saeedi and H. Sigmarsson, “Miniaturized evanescent-mode cavity SIW bandpass filter with spurious suppression,” 2018 IEEE Radio and Wireless Symposium (RWS), Anaheim, CA, 2018, pp. 234-236, 2018.

6. R. Palmer, C. Fulton, J. Salazar, H. Sigmarsson, and M. Yeary, “The Horus Radar – An All-Digital Polarimetric Phased Array Radar for Multi-Mission Surveillance”, American Meteorological Society Annual Meeting, Phoenix, AZ, 2019.

7. R. Palmer, C. Fulton, J. Salazar, H. Sigmarsson, and M. Yeary, “An Update on the “Horus” All-Digital Polarimetric Phased Array Weather Radar”, AMS Radar Conference, Nara, Japan, 2019.

8. J. Lake, M. Yeary, and R. Palmer, “Real-time digital equalization to enhance element-level digital beamforming,” 2019 IEEE Radar Conference, 2019.

9. M. Yeary, R. Palmer, C. Fulton, J. Salazar, and H. Sigmarsson, “Recent Advances on an S-band All-Digital Mobile Phased Array Radar,” IEEE International Symposium on Phased Array Systems & Technology, 2019.

10. C. Fulton, R. Palmer, M. Yeary, J. Salazar, H. Sigmarsson, M. Weber, A. Hedden, “Horus: A Testbed for Fully Digital Phased Array Radars”, Microwave Journal, January 2020.

11. S. Saeedi, G. Ariturk, and H. H. Sigmarsson, “Compact Wide-Stopband Bandpass Filter Based on Highly-Loaded Substrate Integrated Cavity Resonators,” in 2020 IEEE Radio and Wireless Symposium (RWS), San Antonio, TX, 2020.

9. Summary and NexPAR Risk Reduction Recommendations

As described in this report, significant progress in addressing the NexPAR technical challenges summarized in Fig. 9.1 has been accomplished with support from the SENSR feasibility study and OAR/NSSL's ongoing "Tornado Severe Storm Research/Phased Array Radar" Program.

Figure 9.1: Key meteorological PAR research areas

Section 2 discussed data- and model-driven analyses of the operational benefits realizable using PAR. Data assimilation techniques development for WoFS – including determination of optimal observation/assimilation cycle times and refinement of dual-polarization assimilation methods – has progressed significantly, leading towards more realistic assessment of the benefits PAR can bring to this future warning paradigm. OSSE's have indicated that adaptive radar interrogations of the severe storm environment, for example by observing clear-air winds in the inflow region of severe storms might have warning and forecast benefits. Observational studies using NSSL's experimental WSR-88D operating in a rapid-sector scan mode have documented the value of monitoring polarimetric signatures (e.g. ZDR columns) with fast temporal update. Sections 3 and 4 described analysis of PAR data quality characteristics and rapid scanning concepts using a high fidelity Signal Processing and Radar Characteristics (SPARC) simulator. SPARC is being used to assess a variety of candidate PAR architectures - for example a rotating planar array, alternative spatial and temporal sampling techniques, and advanced signal processing techniques not readily emulated with NSSL's current PAR testbeds.

In Section 5, we discussed econometric studies of operational impacts of enhanced low altitude coverage for tornado warning and flash flood warnings. The assumptions and methods of analysis indicate that deployment of gap-filling radars, or a more dense overall radar network

might improve warning performance, with an associated reduction in casualties. This information will be useful in the cost benefit analysis of future radar systems.

Section 6 summarized research addressing the NexPAR calibration and bias compensation methods essential for providing dual polarization variable estimates meeting NWS requirements. Computational electrodynamic modeling, near- and far-field array probe calibrations and mutual coupling based techniques show considerable promise. A large, dual-polarization phased array radar – the Advanced Technology Demonstrator or ATD – has been deployed at NSSL and initial data analysis provides encouraging evidence that these methods will be effective.

The engineering issues that will inform the choice of array architecture are being addressed using both ATD and smaller PAR prototypes - a cylindrical polarimetric PAR (CPPAR) described in Section 7 and an all-digital planar PAR (Section 8). Experiments using near- and far-field calibration sources and storm target-of-opportunity measurements are exposing the strengths and limitations of these various architectures in realizing NWS observational requirements.

This significant progress towards resolving key questions for meteorological PAR, and the simplification of requirements resulting from the single-mission NexPAR CONOPs make it appropriate to focus the OAR research effort to support an acquisition Analysis of Alternatives decision for the WSR-88D replacement network in the coming decade.

Research to Operations Framework: Figure 9.2 is a timeline depicting the recommended R2O program. Four interdependent research thrusts will resolve outstanding meteorological PAR engineering issues, adapt WoFS assimilation and modeling techniques for PAR and validate benefits, optimize forecaster HMI and work flows for PAR, and continue evaluation of alternative radar network topologies.

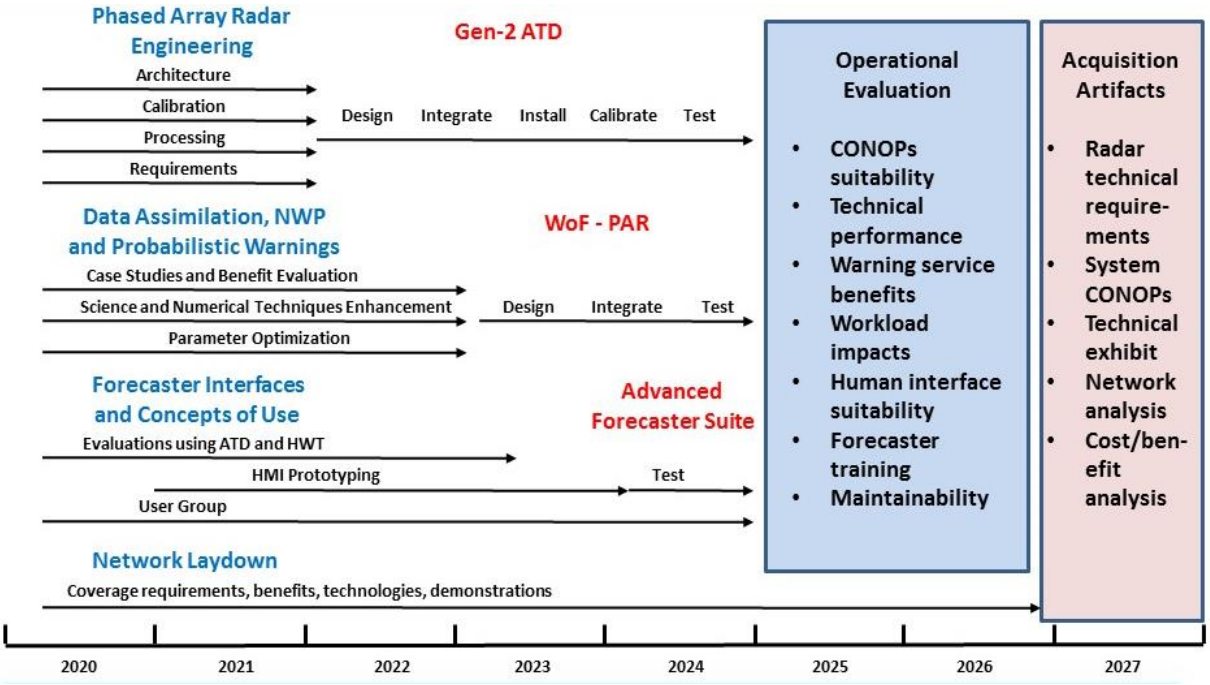

Figure 9.2: NexPAR Research to Operations Framework

We expect that the outcome of the first phase of the program will be, by the end of 2022 a determination that - with reasonable expectations for ongoing technology maturation -- PAR can provide a robust operational and technical solution for the WSR-88D replacement network.

Follow-on effort in 2023-2024 will develop high-fidelity prototypes of the required technologies:

i. a "Gen 2 ATD" providing observational capabilities largely consistent with NWS objective requirements for quality of observations and volume scan update rate;

ii. a real-time "Warn on Forecast - PAR" probabilistic warning system analogous to the NSSL Experimental Warn-on-Forecast System for ensembles (NEWS-e) but adapted to and benefiting from the higher update observations provided by PAR;

iii. appropriate forecaster decision support tools and HMI to view, manipulate and integrate information provided by the radar processing systems.

Operational evaluations in 2025-2026 will assess the technical performance of the prototype systems, their benefits for warning and forecast services, workload impacts and the suitability of the overall CONOPS. These evaluations may also provide insight into appropriate forecaster training processes for the new technology, and system maintainability in a quasi-operational configuration.

Data obtained through these operational evaluations and supporting analysis will result in critical artifacts to support a WSR-88D replacement key decision point (KDP) in 2028. KDP artifacts will include:

i. mature radar technical requirements;

ii. a validated system-level CONOPS;

iii. "technical exhibits" serving as Government Furnished Information (GFI) for industry, specifically the prototype radar, processing and HMI systems and associated design and performance data;

iv. cost/benefit analysis (CBA);

v. an evaluation of radar network modifications relative to today's laydown (e.g. deployment of gap-fillers where CBA justifies this).

Establishing effective technical leadership and interaction amongst stakeholders is critical for this complex R2O project. Radar engineers and meteorologists will engage with NWS requirements-setting organizations (e.g. the "Office of Observations" and the "Analyze, Forecast and Support Office") to converge on requirements and technical solutions. NWS operational forecasters will participate throughout the development, test and evaluation of the prototype system and will be integral in developing the overall concept of operation.

Ongoing coupling to the SENSR acquisition program will provide valuable insight into the maturity, manufacturability, maintainability and cost of PAR technology and will allow NOAA to influence requirements for SENSR's "ATC weather" products so that these can be usefully integrated as supplementary data.